ARL6IP1 in Endoplasmic Reticulum Homeostasis and Axonal Maintenance

Dissertation

zur Erlangung des akademischen Grades

doctor rerum naturalium (Dr. rer. nat.)

vorgelegt dem Rat der Medizinischen Fakultät

der Friedrich-Schiller-Universität Jena

von M. Sc. Hartmut Bocker

geboren am 19.08.1989 in Jena

Gutachter:

1. Prof. Dr. Christian A. Hübner (Jena)
2. Prof. Dr. Helen Morrison (Jena)
3. Prof. Dr. Ingo Kurth (Aachen)

Tag der öffentlichen Verteidigung: 07.09.2021

Meinen Eltern und Großeltern gewidmet, die die Neugier in mir weckten.

„Dass ich erkenne, was die Welt

im Innersten zusammenhält.“

— Faust I, Johann Wolfgang von Goethe

Table of Contents

Abbreviations

(d)dH_2O (double) distilled water

aa	Amino acid
APH	Amphipathic helix
ATG	Autophagy-related
AU	Arbitrary units
AUC	Area under curve ≙ integral
BCA	Bicinchoninic acid assay
bp	Base pairs
CMAP	Compound muscle action potential
CoIP	Co-immunoprecipitation
DMEM	Dulbecco's Modified Eagle Medium
DRG	Dorsal root ganglion
EM	Electron microscopy
ER	Endoplasmic reticulum
ERAD	ER-associated protein degradation
ERES	ER exit sites
ERLAD	ER-to-lysosome-associated degradation
FBA	Foot-base angle
FBS	Fetal bovine serum
HRP	Horse radish peroxidase
HSAN	Hereditary sensory autonomic neuropathy
HSP	Hereditary spastic paraplegia
IB	Immunoblotting
ICC	Immunocytochemistry
IF	Immunofluorescence
IHC	Immmunohistochemistry
LIR	LC3-interacting region
m	months old
MEFs	Mouse embryonic fibroblasts
MIP	Maximum intensity projection
MRI	Magnetic resonance imaging
NCV	Nerve conduction velocity
NMJ	Neuromuscular junction
P/S	Penicillin/Streptomycin
PCR	Polymerase chain reaction
PFA	Paraformaldehyde
RHD	Reticulon homology domain
RT	Room temperature
SEM	Standard error of the mean
SPG61	Spastic Paraplegia 61
SV40	Simian virus 40, used for cell immortalisation
TBS-T	Tris-buffered saline with Tween20
UPR	Unfolded protein response

The human genes and proteins are capitalised whereas proteins and genes of murine or other offspring are written with only an initial capital. Genes and coding RNAs are italicised.

The digital copy of this thesis is an interactive document. For convenience, the table of contents and cross references to figures, tables or chapters are clickable links. Hyperlinks to the www are underlined.

1 Abstract

ADP-ribosylation factor-like protein 6-interacting protein 1 (ARL6IP1) is an endoplasmic reticulum (ER) membrane protein which contains reticulon-homology domains (RHDs) that mediate the ability of the protein to bend membranes. Mutations in *ARL6IP1* are reported to cause severe neurological disorders including hereditary spastic paraplegia (HSP) and insensitivity to pain. Although ubiquitously expressed, the protein appears to play a specific role in the survival of long-projecting neurons as described in the clinical picture termed SPG61.

Within the scope of this study, a colocalisation between ARL6IP1 and the ER-phagy receptor FAM134B within the ER was shown and the protein-protein interaction verified by co-immunoprecipitation. While a direct role in ER-phagy by LC3-binding was previously described for FAM134B, identified putative LC3-interacting regions (LIRs) in ARL6IP1 were shown to be non-functional. Further *in vitro* experiments could verify an oligomerisation of ARL6IP1 and pinpoint it to its N-terminal half. In contrast to previous reports, a Fluorescence Protease Protection (FPP) assay points to a cytosolic C-terminus of ARL6IP1. Together these findings suggest that ARL6IP1 plays a role in ER morphology and compartment regulation through oligomerisation and activity in membrane fragmentation.

A knock-out (KO) mouse model for *Arl6ip1*-deficiency was developed and analysed in this work. The most striking phenotype found in *Arl6ip1*-KO mice was infantile onset of several characteristic features of the SPG61 disease phenotype. This includes a progressive loss of motor functions as shown by gait analysis and grip strength measurements. Nerve conduction velocity studies further revealed a progressive decrease in sensory function. A loss of cerebellar Purkinje neurons and spinal motor neurons was observed in animals deficient of *Arl6ip1*, verifying neuronal degeneration. A newly generated reporter mouse line expressing a fluorescent protein within the ER of *Emx1*-positive neurons was used to identify further morphologic changes in *Arl6ip1*-KO mice (*Arl6ip1-ER-Tomato-Emx1*). While Tomato-positive punctae, likely depicting debris or fragmented ER within neurons, were found in cortex and hippocampal Schaffer collaterals, axon swelling was specifically observed in fibre tracts of the spinal cord. The latter was verified by electron microscopy which additionally uncovered ER and mitochondria alterations in cultured dorsal root ganglia (DRG) neurons.

Remarkably, the loss of *Arl6ip1* in mice results in both motor deficits and sensoneuropathy, but *Fam134B*-deficiency only in the latter. This suggests that Arl6ip1 is either upstream of a Fam134B regulation or has in contrast to Fam134B far-reaching functions in motor neurons.

Taken together, this study enables the profound characterisation of an animal model mimicking the human neurodegenerative disease phenotype caused by Arl6ip1 loss. Furthermore, it underlines the protein's role in ER morphology and possibly autophagic processes, highlighting the crucial role of this gene product for neuron homeostasis and cellular survival.

2 Zusammenfassung

ARL6IP1 ist ein Protein in der Membran des Endoplasmatischen Retikulums (ER), welches über Retikulon-Homologie Domänen (RHD) verfügt, die dem Protein die Eigenschaft verleihen Membranen zu formen. Mutationen im Gen *ARL6IP1* führen im Menschen zu schwerwiegenden neurologischen Erkrankungen wie der Hereditären Spastischen Paraplegie (HSP) und einer Form der Schmerzunempfindlichkeit. Trotz der ubiquitären Expression in verschiedenen Gewebetypen, scheint das Protein eine besondere Rolle für das Fortbestehen von Neuronen mit langem Axon zu haben. Die Ergebnisse dieser Arbeit erweitern das Wissen zum pathogenetischen Mechanismus der durch Mutationen in *ARL6IP1* verursachten Neuropathien (SPG61 und sensorische Neuropathie).

Eine Kolokalisation von ARL6IP1 und dem ER-spezifischen Autophagierezeptor FAM134B konnte beobachtet und eine Interaktion beider Proteine mittels Koimmunpräzipitation im Rahmen dieser Arbeit nachgewiesen werden. Während für FAM134B der Wirkmechanismus über eine direkte Bindung an das in autophagosomalen Membranen vorliegende LC3-II bekannt ist, konnten Untersuchungen von ARL6IP1 zwar putative LC3-interagierende Regionen (LIR) in ARL6IP1 identifizieren, eine Bindung von LC3-II jedoch nicht bestätigen. Weitere Experimente konnten die bereits publizierte Oligomerisierung von ARL6IP1 belegen und die N-terminale Proteinhälfte als dafür essenziell ermitteln. Im Gegensatz zu früheren Publikationen konnten detaillierte Topologiestudien zeigen, dass der C-Terminus von ARL6IP1 cytosolisch lokalisiert ist.

Neben den proteinbiochemischen und zellbiologischen Untersuchungen wurde ein *Arl6ip1*-Knock-Out (KO) Mausmodell generiert, in welchem das Auftreten deutlicher Symptome des SPG61-Phänotyps schon im jungen Alter besonders auffällig war. Diese beinhalteten progressive Defekte von motorischen Nervenfunktionen, wie die Analysen des Fußbasiswinkels und der Griffstärke zeigten. Messungen der Nervenleitgeschwindigkeiten wiesen zudem auf einen Verlust der sensorischen Funktionen hin. In histologischen Untersuchungen stellten sich in *Arl6ip1*-KO eine Reduktion an Purkinjezellen und spinalen Motorneuronen heraus, was eine Neurodegeneration bestätigt. Erste Tiere einer zusätzlich generierten Mauslinie (*Arl6ip1-ER-Tomato-Emx1*), welche das fluoreszierende Reporterprotein *Tomato* im ER von *Emx1*-positiven Zellen exprimiert, zeigten Tomato-positive punktartige Strukturen im Cortex und in den Schaffer-Kollateralen des Hippocampus. Die beobachten Strukturen stellen höchstwahrscheinlich Debris oder fragmentiertes ER dar. Des Weiteren wiesen die leitenden Bahnen des Rückenmarks teils starke Akkumulationen des Tomato-Signals auf. Elektronenmikroskopische Untersuchungen in *Arl6ip1*-KO-Mäusen konnten dies als axonale Schwellungen im Rückenmark auflösen und zusätzlich in kultivierten Spinalganglianeuronen Veränderungen in der Morphologie des perinukleären ERs sowie der Mitochondrien aufzeigen. Die dabei beobachtete Axonopathie erklärt die beschriebenen Symptome.

Da die Abwesenheit von Arl6ip1 in Mäusen zu sowohl motorischen Defiziten als auch einem sensorischen Phänotyp führt, in *Fam134b*-KO-Mäusen jedoch lediglich eine sensorische Neuropathie beobachtet wurde, liegt es nahe, dass Arl6ip1 entweder einer Fam134b-Regulation vorgeschaltet ist oder das Protein eine weitreichende Rolle zusätzlich in Motoneuronen erfüllt.

Zusammengenommen stellt diese Arbeit eine eingehende Analyse des Tiermodels dar, welches die humanen neurodegenerativen Symptome als Folge von Mutationen in *ARL6IP1* nachbilden. Weiterhin unterstreicht diese Arbeit die Rolle des Proteins in der ER-Morphologie und legt einen Bezug zu Autophagieprozessen nahe, was die Wichtigkeit von ARL6IP1 für Neuronenhomöostase und -überleben betont.

3 Introduction

3.1 Neurons

Neurons are highly specialised cells and are needed for quick and targeted transmission of information. On one hand they differentiate early to a postmitotic state and cannot be replaced by new cells, on the other hand they have a characteristic structure with an axon which often bridges far distances. Neurons can be classified by several characteristics including location (central nervous system, CNS vs peripheral nervous system, PNS), their function (motor, sensory or autonomous neuron) presence of myelination, the direction they transmit signals (afferent: to the CNS, efferent: from the CNS), their released neurotransmitter and further (Kandel *et al.* 2000).

3.1.1 Central and peripheral nervous system

The CNS consists of the brain and spinal cord which are both surrounded by bone structures. The PNS comprises all nervous tissue outside of brain and spinal cord. The PNS consists of the somatic or voluntary nervous system which mediates muscle contraction (motor neuron) or sensation transmission (sensory neuron), and the autonomous or involuntary nervous system which controls and monitors organ functions such as the digestive system, blood pressure, heartbeat etc. (Figure 1). Whereas neurons within the CNS can range from few millimetres to

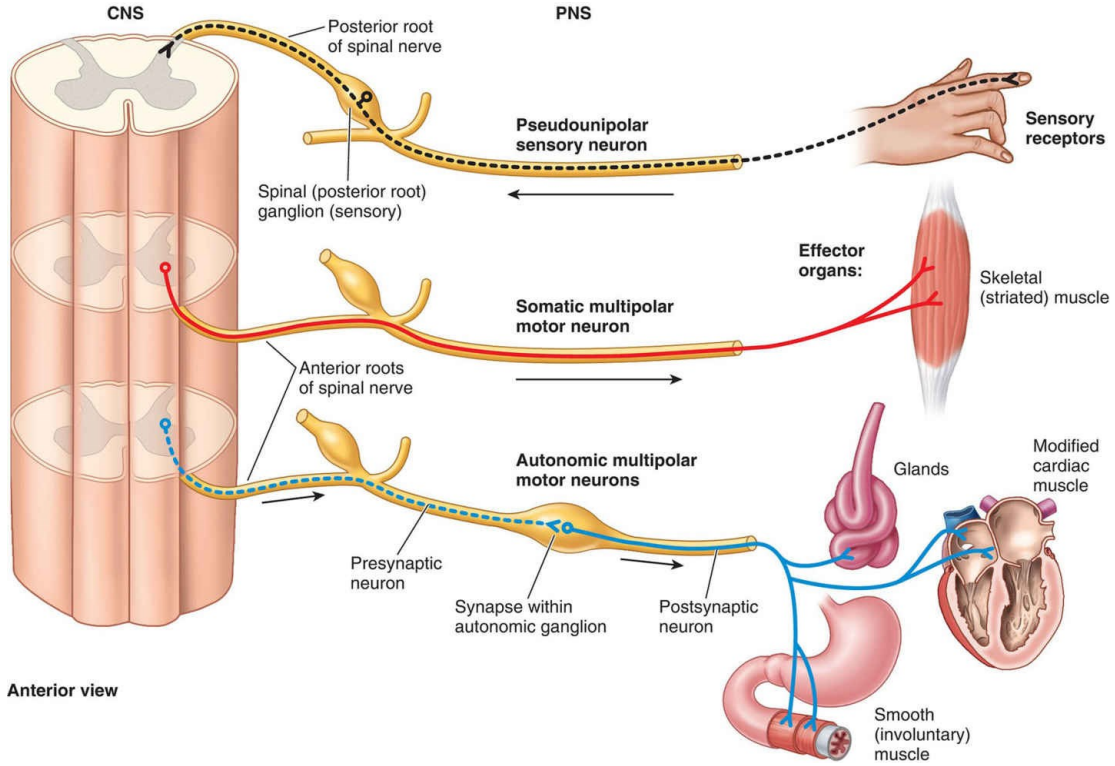

Figure 1: Peripheral nervous system. *Neurons of the peripheral nervous system (PNS), their soma location and projections. From Moore and Dalley (2018).*

~1 meter in length in humans, neurons or axons within the PNS are generally long-projecting. Neurons like lower motor neurons have their soma located in the CNS but the axon in the PNS (Bear *et al.* 2020).

3.1.2 Sensory neurons

Sensory neurons are transmitting information like pain, touch, proprioception and temperature from the periphery in afferent fibres via the spinal cord to the brain (Figure 2A). First-order sensory neurons are pseudounipolar which means they do not possess dendrites as the divided axon is replacing their function. They have their cell bodies located in dorsal root ganglia (DRG) right next to the spinal cord on the level they innervate it (Kandel *et al.* 2000).

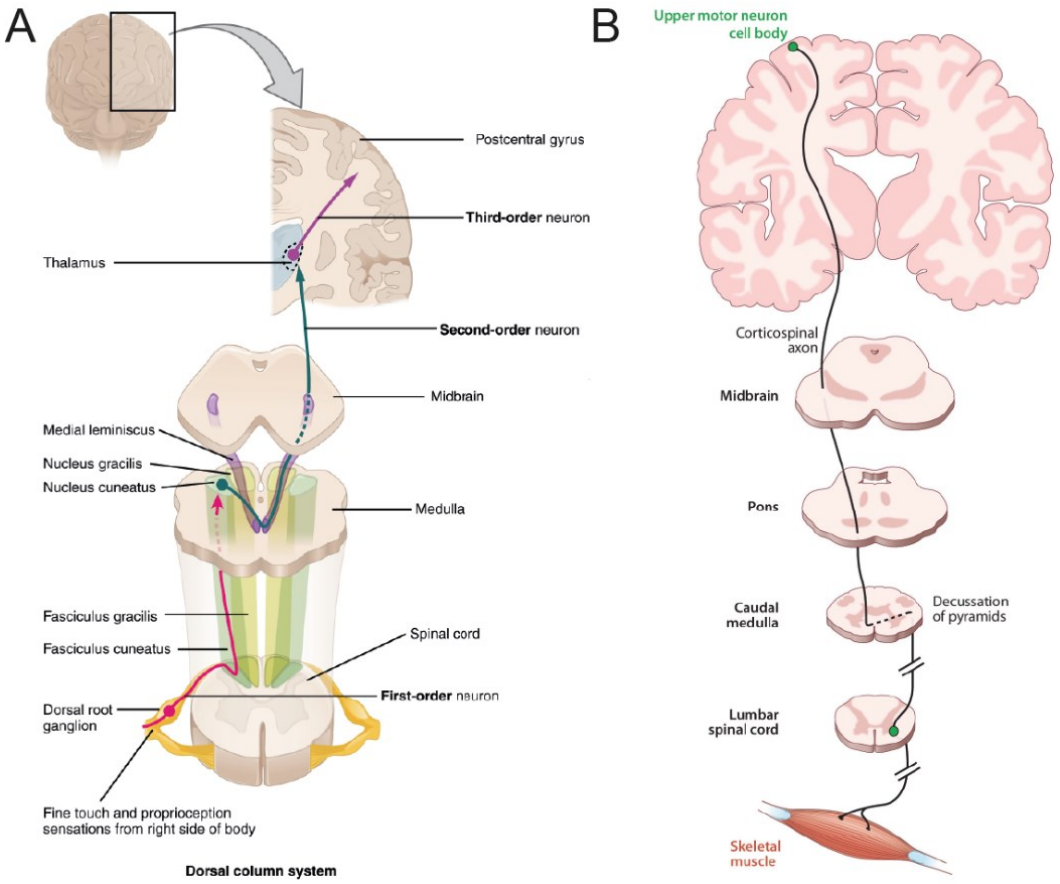

Figure 2: Neuron pathways and projections. *(A) Sensory neurons are afferent cells and transmit signals like pain, touch, proprioception and temperature via the spinal cord, medulla and midbrain to the cerebral cortex. First order neurons have their soma in the dorsal root ganglia. The sensation is projected via several neurons into the somatosensory cortex. (B) Motor signals derive from the somatomotor cortex, where the multipolar motor neurons have their soma. By travelling through the hindbrain and spinal cord, these efferent, upper motor neurons innervate lower motor neurons which further project to skeletal muscles. Modified from Biga et al. (2019), Blackstone (2012).*

3.1.3 Motor neurons

These specialised cells transmit impulses of the somatomotor cortex to effector muscles. For this, the upper motor neuron innervates a lower motor neuron in the spinal cord (Figure 2B). At the horizontal level of the lower neuron, its axon is leaving the spinal cord to innervate a set of muscles fibres via neuromuscular junctions (NMJs, Blackstone 2012, Kandel *et al.* 2000).

3.1.4 Neurons in disease

The large distance within a cell requires a complex cellular machinery for sorting, packaging and distributing proteins, cytoskeletal elements, lipids, organelles and other molecules resulting in vulnerabilities due to the number of involved proteins (Blackstone 2018). Hence, neurons not only are extremely susceptible to various kinds of stresses such as traumatic injury, environmental toxins, heavy metals, cardiovascular disorders or infectious agents but also genetic impairments resulting of mutations in diverse, crucial genes (Hutchins and Barger 1998).

3.2 Polyneuropathies

These are diseases affecting multiple neurons and are often associated with symmetrically occurring symptoms such as drop foot on both sides or spasticity of the upper limbs. A main mechanism of disease is axonopathy, were axons or myelination are the site of disorders resulting in a length-dependent dieback of neurons with subsequent early symptoms in distal innervated parts such as the feet (Burgess and Crish 2018). Hereinafter, two major inherited polyneuropathies relevant for this study are described.

3.2.1 Hereditary Spastic Paraplegia

Progressive motor neuron loss is a typical feature of Hereditary Spastic Paraplegia (HSP), also named after the early describers Strümpell-Lorrain disease (Lorrain 1898, Strümpell 1883), that is first recognisable in the lower limbs due to its neuron-length dependency. Because of defective innervation, muscle fibres are denervated resulting in muscle atrophy and weakness of lower limbs. As this disease is progressive, the symptoms appear to climb up body regions over the course of months or years. There are two causative variants: Degeneration of either upper motor neurons or both upper and lower motor neurons (Parodi *et al.* 2017).

3.2.2 Hereditary Sensory and Autonomic Neuropathy (HSAN)

In this group of clinical heterogeneous neuropathies axons of sensory and autonomic neurons are primarily affected. For both myelinated and unmyelinated fibres an axonal loss can be observed in this genetically driven but rare disorder (Katona and Weis 2017). Clinical signs are loss-of-sensation, including nociception, temperature and touch, starting on distal digits often leading to secondary symptoms such as ulceration, acromutilation and chronic osteomyelitis (Kurth 2010). Molecular pathways of these symptoms are goal of current research with putting cellular processes such as impaired autophagy into the focus (Khaminets *et al.* 2015).

3.3 Autophagy

Autophagy ("self-eating") describes a cellular process at which intracellular molecules or parts of cellular organelles are degraded and broken down to molecular building blocks which can be reused for biosynthetic processes or energy release. Macro-autophagy or often synonymously termed autophagy is triggered for example by starvation, which leads to a general, untargeted recycling of cellular material. Specific autophagy targets can be different organelles such as e.g., defective mitochondria or ER fragments. The generation of the phagophore and its maturation to autophagosome and finally autolysosome is a complex and tightly regulated process, which involves the concerted action of approximal 30 highly conserved autophagy-related (ATG) proteins, numbered in order of their action within autophagy (Klionsky 2012, Klionsky *et al.* 2003, Lopez *et al.* 2018).

3.3.1 Autophagy initiation by generation of phagophores

The phagophore initiation takes places in the cytosol by nucleation of three protein complexes: the ULK1 initiation complex (containing ATG1/ULK1, ATG13, ATG101), the PI3K III nucleation complex (ATG14, Beclin, VPS15, VPS34) and the PI3P-binding complex (WIPI, DFCP1, ATG16L1, ATG5, ATG12 activated by ATG7 and ATG10, Figure 3A, Hansen *et al.* 2018). ATG9-containing vesicles are recruited to these complexes and thereby deliver lipids to build up a double-layered lipid bilayer (Rao *et al.* 2016). Meanwhile, the cytosolic LC3 (belonging to the ATG8 protein family) is cleaved by ATG4 to LC3-I, the activated form (Figure 3B). This can be linked to a phospoethanolamine (PE) by ATG7 and ATG3 resulting in lipidated LC3-II (Birgisdottir *et al.* 2013). This process takes place next to the PI3P-binding complex, resulting in integration of

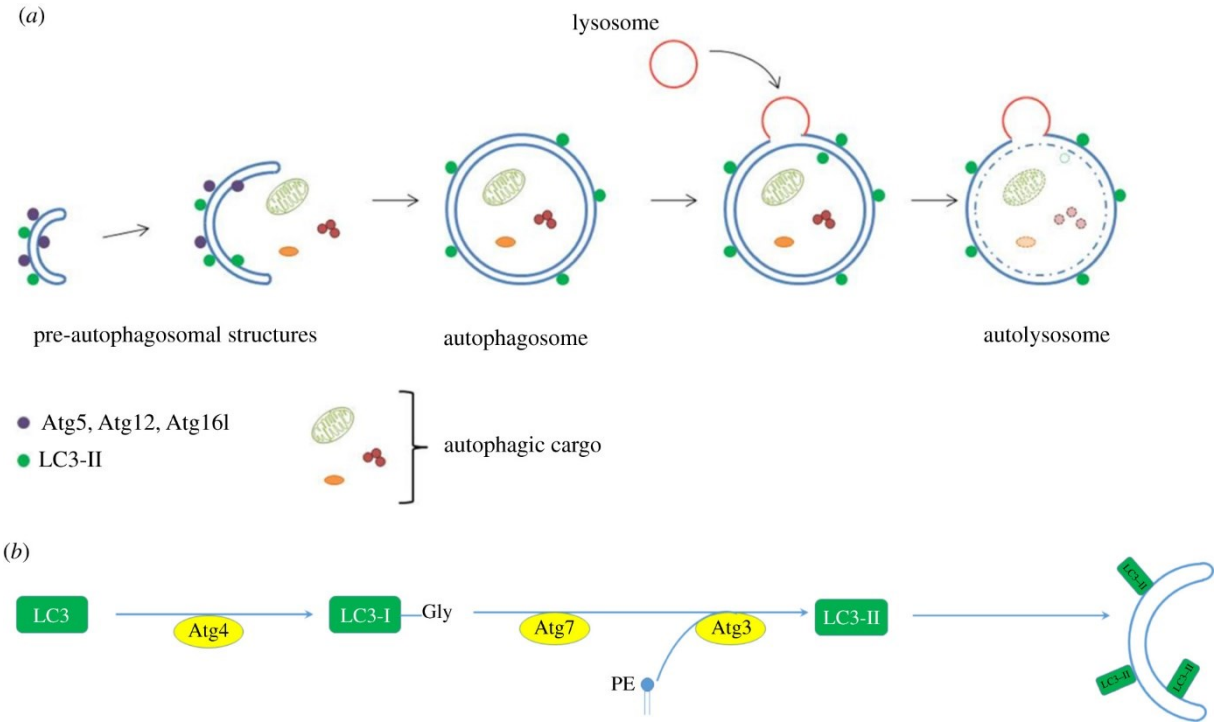

Figure 3: Autophagosome generation and cargo degradation via autolysosome. (A) Upon initiation by the ULK1 complex, pre-autophagosomal structures (also called phagophores) are created while LC3-II is recruited to the pre-autophagic membrane by a ATG5, 12 and 16L1 complex. Specific or unspecific cargo is recruited to the invaginated membrane followed by membrane closure – the autophagosome formation. Note the double lipid bilayer boundary. Subsequently, a lysosome fuses with the outer membrane while the inner membrane is dissolved. The autolysosome is generated allowing the cargo degradation by hydrolases. (B) LC3-II maturation and membrane linking. Cytosolic LC3 is partly cleaved by the protease Atg4, resulting in LC3-I with a C-terminal Glycine. This truncated LC3 is lipidated by the help of ATG7 and ATG3 to a phospoethanolamine (PE) in close neighbourhood of the ATG5/12/16l1 complex leading to insertion in phagophore membranes. The PE-bound LC3-I is termed LC3-II, which is assumed to take part in growth and closure of autophagosomal membranes, in lysosome fusion and degradation of the inner autophagosomal membrane. Modified from Lopez et al. (2018).

LC3-II into the growing phagophore. LC3-II recruitment is thought to be crucial for autophagosomal maturation as it supports the expansion of the phagophore and mediates the recruitment of cargo via LIR-carrying proteins (Birgisdottir *et al.* 2013, Schaaf *et al.* 2016).

3.3.2 Autophagosomes and autolysosomes

The phagophore engulfs its cargo, expands and eventually LC3-II mediates the closure of the phagophore double membranes (**Figure 3**A) resulting in the formation of an autophagosome (Lopez *et al.* 2018, Schaaf *et al.* 2016). Membrane bound LC3-II at cytosolic site is delipidated by ATG4 enabling the recycling of resulting solvent LC3-I (Reggiori and Ungermann 2017). Autophagosomes subsequently fuse in an LC3-II-facilitated process with lysosomes containing hydrolases (proteases and lipases) in its lumen with a strongly acidic milieu (Schaaf *et al.* 2016). This step leads to the resolution of the inner lipid bilayer in an LC3-II-dependent manner (Yu *et al.* 2018), making its previous content accessible for the hydrolases allowing break-up of the

cargo. Biological building blocks such as amino acids, fatty acids, nucleotides and sugars are actively exported into the cytosol to be available for anabolic processes or energy production (Al-Bari 2020, Parzych and Klionsky 2014). The autolysosome eventually undergoes a process termed autolysosomal reformation (ALR) giving rise to early (proto-)lysosomes and is finally disintegrated (Chen and Yu 2017).

3.4 Membrane shaping by proteins

For many cellular processes such as ER-Golgi transport, endolysosomal degradation, vesicle formation, organelle kinetics etc. certain structures of compartments and therefore curvature of their membranes are physiologically required (Zimmerberg and Kozlov 2006). As stated previously, the ER network is a highly evolved and dynamic structure which consists of tubules and sheets, explaining the necessity of structurally shaped membranes.

Phospholipids tend to form planar bilayers or micelles. Hence, mechanisms are required to bring membranes into shape. This is possible by introducing a lipid asymmetry between both layers by having lipids with a more spacious head on the outside of the curvature. Alternatively, membranes can be bent by proteins. Active membrane shaping needs motor proteins (Atlastins, Dynamins etc.) which consume energy by hydrolysis of GTP (Hu *et al.* 2009). Passive membrane shaping (**Figure 4**) is possible by rigid scaffolding proteins that shape membranes by

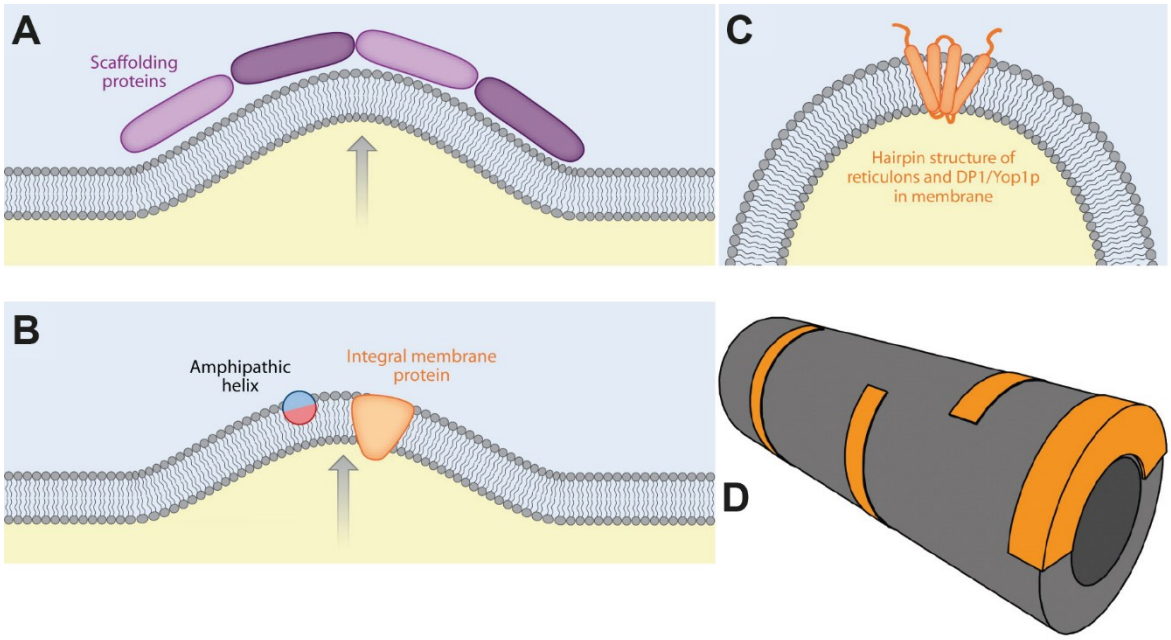

Figure 4: Membrane-shaping by proteins. *(A) Proteins can build a scaffold by interacting with the membrane surface. (B) Partly integrating proteins can also lead to membrane curvature. (C) Proteins carrying a reticulon homology domain (RHD) are able to bend the membrane by asymmetric integration. (D) Resulting tubule-like structure of membranes equipped with reticulons or similar proteins. Modified from (Shibata et al. 2009).*

their concave, membrane-interacting surface (like BAR proteins and COPI or II) or (partly) membrane-integrating proteins that take up more space on the outer compared to the inner membrane side (Shibata *et al.* 2009).

Reticulons and reticulon-like proteins (carrying a reticulon homology domain, RHD), to which also FAM134B and ARL6IP1 belong, are part of the latter, membrane-integrating group.

The RHD is known to integrate in a wedge-like manner into the membrane and thereby induces positive membrane curvature (Hübner and Kurth 2014). Recent findings suggest that a proximal amphipathic helix (Figure 5) is needed for the actual shaping ability of reticulon proteins (Brady

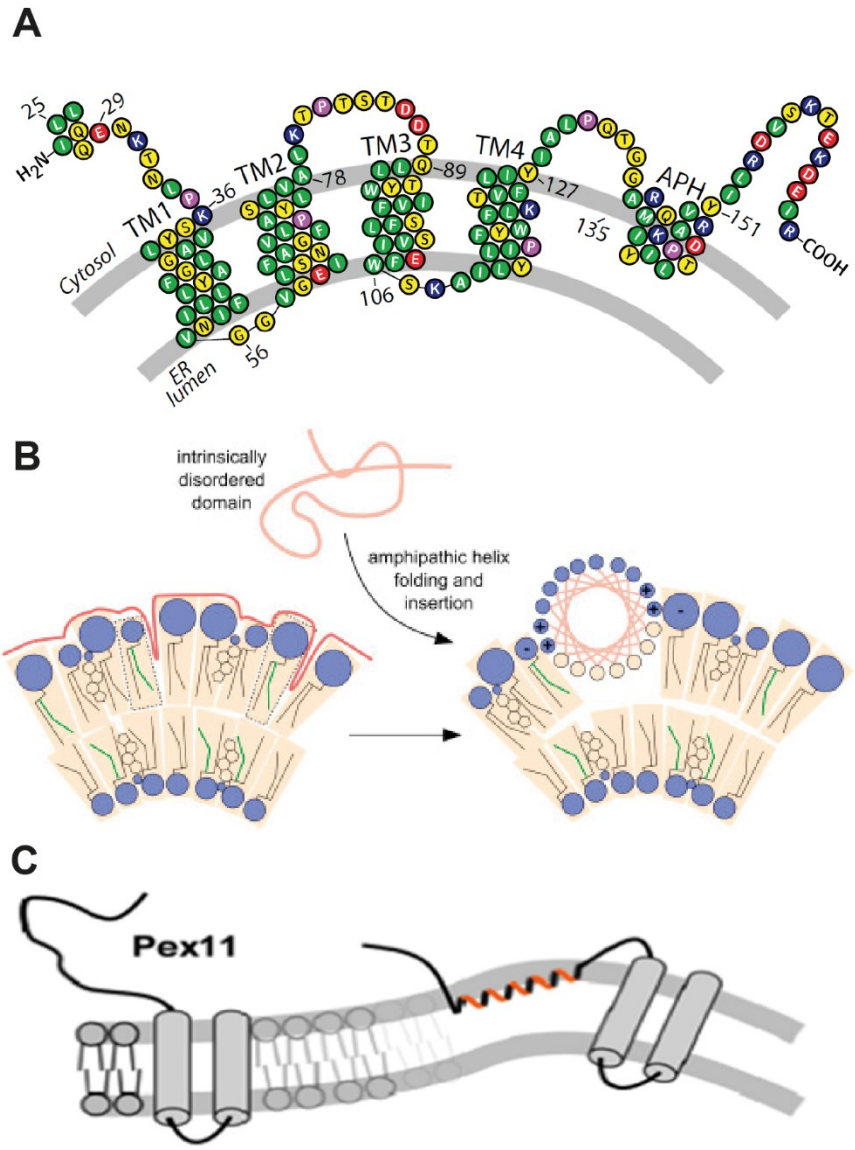

Figure 5: Amphipathic helix (APH) as semi-integrating domain causative for membrane remodelling. *(A) Topology of Yop1p, the yeast homologue of REEP proteins with an APH C-terminal to the second Reticulon homology domain (RHD, Brady et al. 2015). (B) Illustration of the integration process of an APH with axial view (Lauwers et al. 2016). (C) The peroxisomal yeast protein Pex11 with a hydrophobic hairpin next to an APH with outside view (Gimenez-Andres et al. 2018).*

et al. 2015, Breeze *et al.* 2016). Indeed, APHs have been identified in most reticulons or related proteins like FAM134B and ARL6IP1 (Bhaskara *et al.* 2019, Brady *et al.* 2015). The APH consists of an α-helix, which is on one side (parallel to its axis) hydrophilic and on the opposite site hydrophobic. Thereby, the helix is semi-integrating at the membrane surface. In connection with the hydrophobic hairpin of the RHD, this structure may act as lever with a fixed inner angle and thus curves the membrane (Gimenez-Andres *et al.* 2018).

3.5 Endoplasmic Reticulum

3.5.1 Function of the Endoplasmic Reticulum

The Endoplasmic reticulum (ER) is a membrane-enclosed sub-compartment in eukaryotic cells allowing special reaction conditions. It plays an essential role in protein translation, folding, posttranslational modifications, protein quality control, trafficking and potential degradation. These functions are also referred as protein homeostasis, or short proteostasis (Wang and Kaufman 2016). Besides being the largest endomembrane storage, the ER also plays a major role for lipid synthesis (Fagone and Jackowski 2009). The organelle allows the sorting and transfer of proteins and lipids to their specific destination by vesicle budding. As the transfer is not unidirectional, the ER is in lively exchange with other organelles and the plasma membrane (Baumann and Walz 2001).

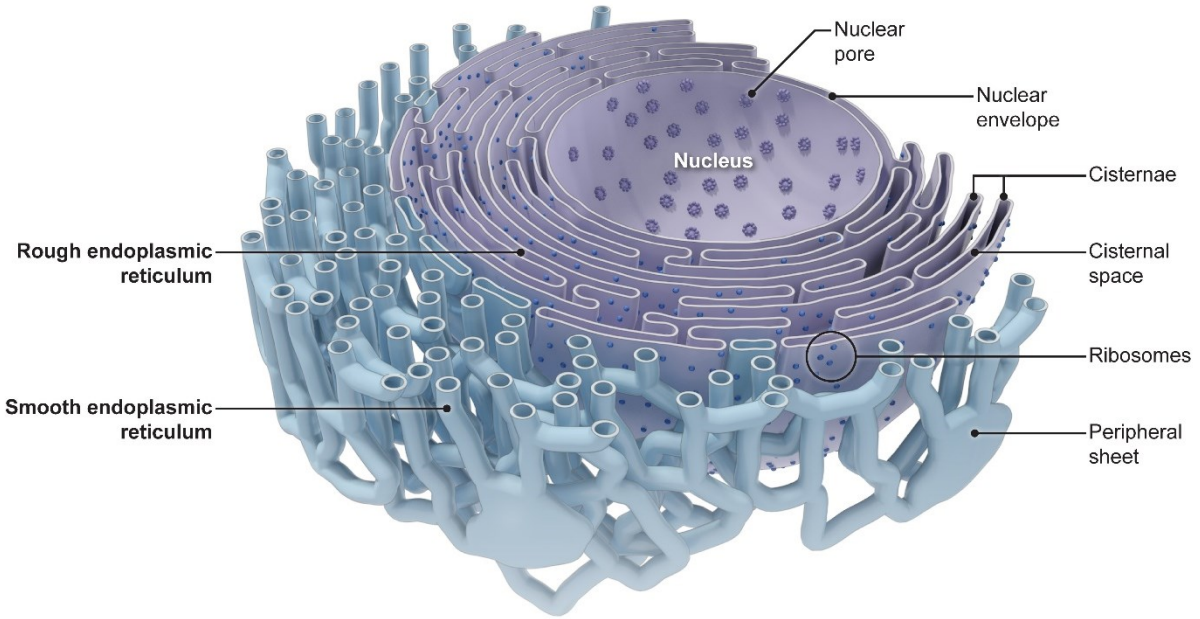

Figure 6: Spatial model of ER. *Note the blueish peripheral tubules and sheets in comparison of the ribosome-decorated juxtanuclear ER (purple) and nuclear envelope. Modified from (Blackstone and Prinz 2016).*

3.5.2 *Morphology of the ER*

The ER consist of a highly dynamic network of tubules, sheets and cisternae (**Figure 6**). From nuclear envelope to cell periphery, the ER consists of ribosome-associated cisternae, the sites of co-translational membrane insertion of proteins, and gradually changes into the smooth tubular ER network with occasional sheets. The latter parts play a role for lipid synthesis and ion homeostasis including Ca^{2+} (Lippincott-Schwartz *et al.* 2000).

It is assumed that also for ER, form follows function (Blackstone and Prinz 2016). The key features (**Figure 7**) of this architecture are supported by several membrane-integrating shaping proteins (chapter 3.4) such as reticulons that stabilise tubules, atlastins that promote tubular three-way junctions und Climp63 that maintain ER sheets (Goyal and Blackstone 2013).

Because of their shape ER tubule tips are predestined to allow budding of vesicles either for transport to the Golgi complex or other destinations (Kurokawa and Nakano 2019). The tubules are also described to mediate physical contact to other organelles such as mitochondria on the mitochondria-associated membranes (MAMs) to promote mitochondrial fission (Friedman *et al.* 2011, Moltedo *et al.* 2019).

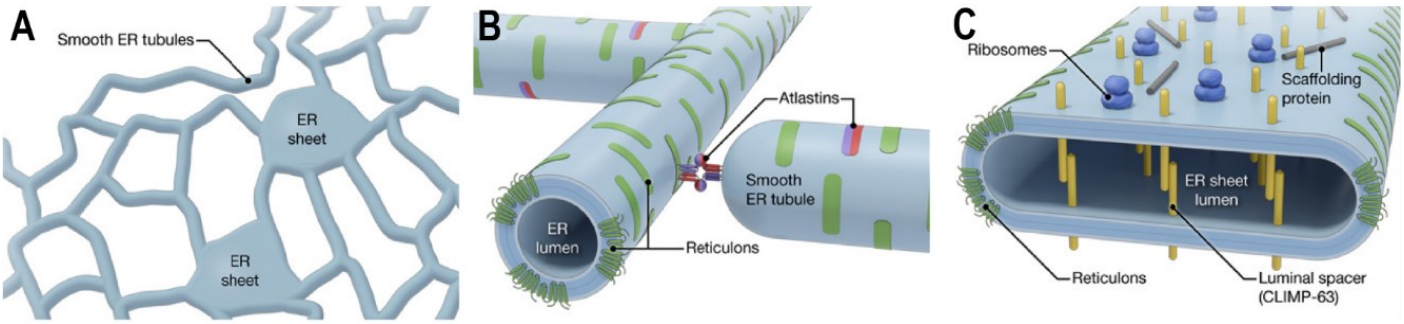

***Figure 7: ER key structures**. (A) ER tubule network with peripheral ER sheets. (B) Three-way junctions of tubular ER. (C) Section of an ER sheet. Modified from Goyal and Blackstone (2013).*

3.5.3 *ER stress*

As mentioned previously, the ER is an essential site for the synthesis and maturation of membrane bound, luminal and secreted proteins. During translation, the nascent protein is folded and, depending on the protein, optional disulphide bounds are formed. The latter two processes are the most error-prone during protein production, demanding for a process of quality control and release or degradation. If not folded correctly, proteins can accumulate and impair proper function of the organelle – ER stress is occurring. This happens on a stochastic basis but can be induced by extrinsic or genetic factors. Molecular sensors like Grp78 can detected en-

hanced levels of unfolded or misfolded proteins and trigger a pathway called the unfolded protein response (UPR). This includes the upregulation of chaperones, attenuation of further protein translation, upregulation of protein degradation processes and eventually, if the stress cannot be resolved after a certain period, apoptosis.

3.5.4 ER-phagy – selective autophagy of the ER

As stated earlier, autophagy can be unspecific (chapter 3.3) or selective. The latter is induced by its cargo which could be cytosolic protein aggregates or damaged or superfluous organelles such as mitochondria, nucleus or ER (Gatica *et al.* 2018, Zaffagnini and Martens 2016). In the case of the selective autophagy of the ER, a process termed ER-phagy or reticulophagy, parts of the ER membrane including its luminal cargo like misfolded proteins bud from the organelle

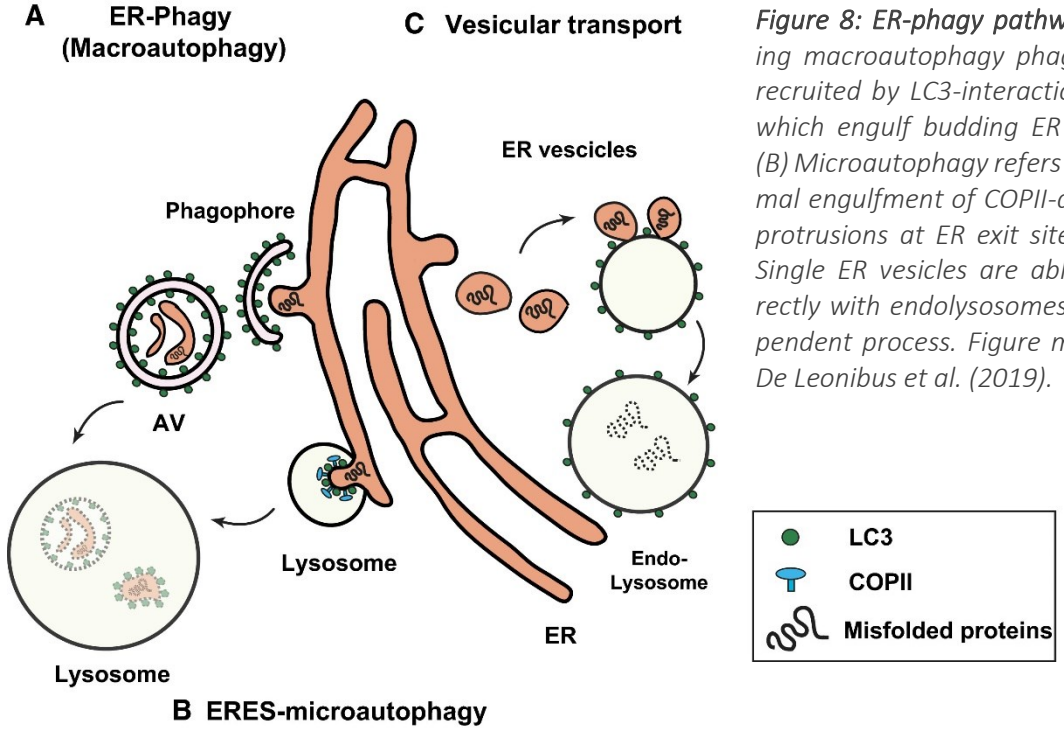

Figure 8: ER-phagy pathways. (A) During macroautophagy phagophores are recruited by LC3-interaction to the ER, which engulf budding ER membranes. (B) Microautophagy refers to the lysosomal engulfment of COPII-dependent ER protrusions at ER exit sites (ERES). (C) Single ER vesicles are able to fuse directly with endolysosomes in a LC3-dependent process. Figure modified from De Leonibus et al. (2019).

to eventually fuse with a lysosome to allow degradation. Recently, different ways of ER-phagy have been described (Figure 8). First, the macro-ER-phagy process is similar to the previously explained macro-autophagy with the only difference of a targeted phagophore recruitment to the ER membrane. The resulting autophagosome fuses with a lysosome to an autolysosome allowing degradation of its cargo (Khaminets *et al.* 2015, Stolz *et al.* 2014). Secondly, a process termed Micro-ER-phagy or ERES microautophagy was reported recently (Schuck *et al.* 2014, Omari *et al.* 2018). In this, the budding ER exit sites (ERES), hubs for the secretory pathway, are

engulfed by lysosomes in a COPII-dependent manner and finally taken up by them for degradation. Thirdly, ER-deriving vesicles can fuse directly with LC3-decorated endolysosomes. This process is called vesicular delivery (Fregno and Molinari 2019, Fregno *et al.* 2018). All three variants have in common that cargo like improperly folded proteins and ER membranes are removed thus diminishing ER stress and regulating ER turnover. These pathways are referred to as ER-to-lysosome-associated degradation (ERLAD) in contrast to a lysosome-independent, proteasome-dependent mechanism called ER-associated protein degradation (ERAD).

3.5.5 ER-phagy receptors

ER-phagy receptors mediate the recruitment of/to membranes of the lysosomal pathway by recognizing and binding specific marker proteins. In the past years more and more ER-phagy receptors have been identified (Figure 9). They range from ER tubule-enriched proteins (RTN3) over rather ER sheet edge-enriched proteins (FAM134B) to cargo sensing proteins (CCPG1, Grumati *et al.* 2018). These ER-phagy receptors have in common that they are ER-resident membrane proteins harbouring LIR or FIR (FIP200-interacting region) motifs (Stolz and Grumati

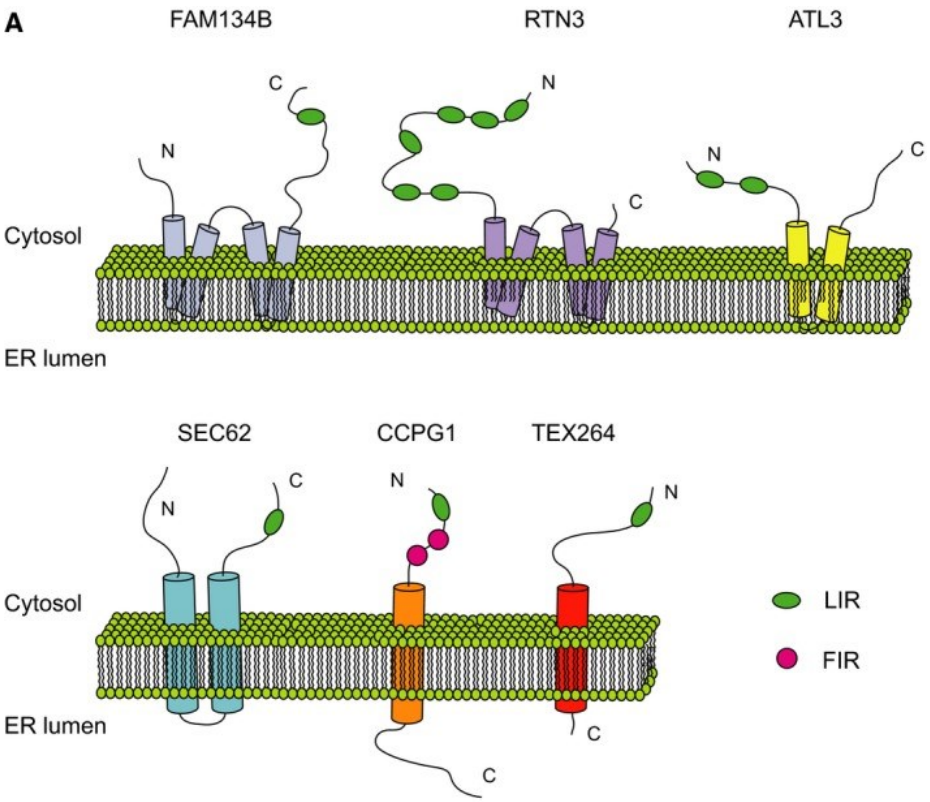

Figure 9: Known ER-phagy receptors. The ER-membrane proteins harbour either LC3-interacting regions (LIR) or FIP200-interacting regions (FIR) at which they can bind to their counterpart residing in or at the phagophore and later autophagosomal membrane. Modified from Stolz and Grumati (2019).

2019). With those they can bind to LC3-II, which resides in the phagophore and autophagosome. FIP200 builds a membrane-attached complex during the autophagosome initiation and fulfils a similar task like LC3-II for membrane recruitment (Kirkin and Rogov 2019).

Fam134B was identified as ER-phagy receptor in previous work of the laboratory of the author.

3.6 FAM134B

3.6.1 General

This protein is the second member (hence B) of the family with sequence homology 134. Loss-of-function by homozygous premature stop codons (Q145X, S309X, P7GfsX133) or splice mutations (c.873+2T>C) were associated with early onset HSAN 2B and acro-osteolysis in patients (Kurth *et al.* 2009). FAM134B contains two RHD domains while it was recently reported that it also carries two APHs C-terminal of each RHD (Bhaskara *et al.* 2019). With these features, it partly integrates (**Figure 10**) into the membranes of the ER, the ER-Golgi intermediate compartment (ERGIC) and the cis-Golgi, while having a cytosolic N- and C-terminus (Hübner and Kurth 2014). The membrane shaping ability was verified by incubation with liposomes resulting in a prevalence of lower diameter liposomes compared to control (Khaminets *et al.* 2015).

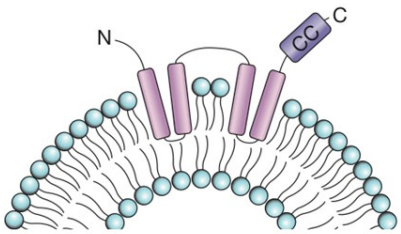

Figure 10: Assumed topology of FAM134B. *The two reticulon-homology domains (RHD, pink) are integrating into the membrane. A predicted amphipathic helix C-terminal of the second RHD is not shown. A coiled-coil (CC) domain containing the LC3-interacting region (LIR) motif is located at the C-terminus of the protein. Modified from Hübner and Kurth (2014).*

3.6.2 LC3-interacting region

FAM134B resides in ER membranes and is able to recruit LC3 by its LIR domain to promote selective ER-phagy. Thereby, FAM134B recruits autophagosomal membranes (phagophores) to the ER, which is budding partly due to the shaping properties of the protein and partly as a result of yet to be determined mechanisms. When the budded ER is engulfed by autophagosomal membranes, the autophagosome fuses with lysosomes (Carlsson and Simonsen 2015). Because of its LC3-interaction, FAM134B serves as an ER-phagy receptor and was lately also dubbed Reticulophagy Regulator 1, or short RETREG1 (Kurth (2010), updated 2015).

3.7 ARL6IP1

3.7.1 General

In a yeast two-hybrid screen ARL6IP1 was identified as a potential interaction partner of FAM134B (unpublished results). The protein's importance for the neuronal system was soon verified by the first description of an HSP phenotype in patients caused by the frameshift mutation K193F*fs (Novarino *et al.* 2014).

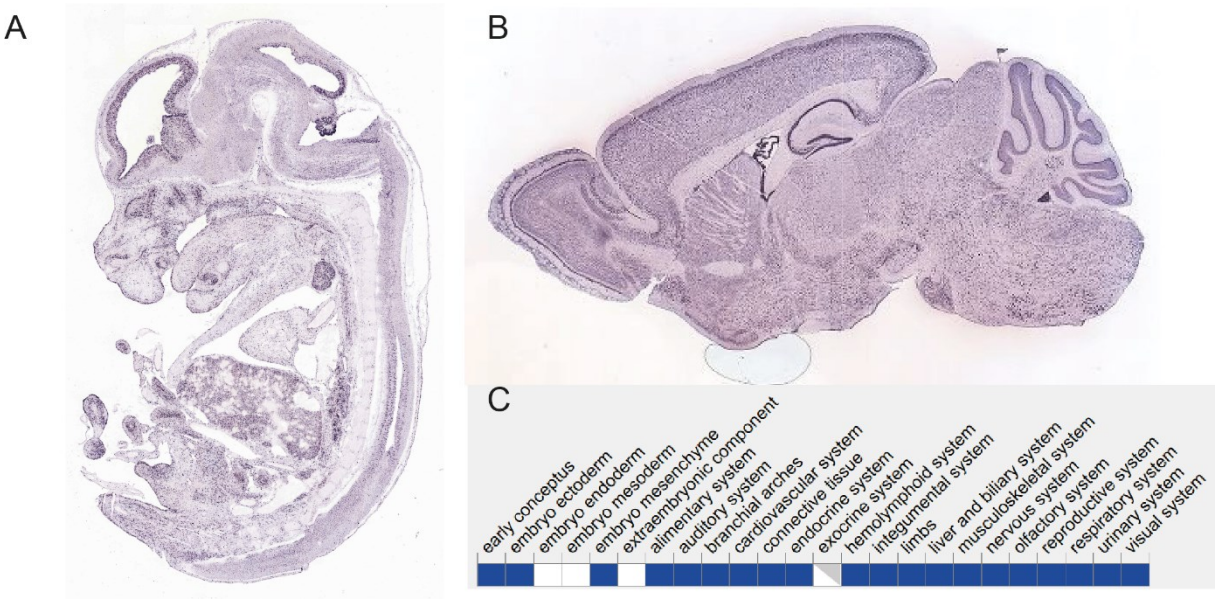

Figure 11: Expression of Arl6ip1. *(A)* In situ *hybridisation with an anti-*Arl6ip1 *probe on sagittal section of a mouse embryo shows ubiquitous expression. From* eurexpress.org*, Assay ID:euxassay_017744, age unknown. (B) Sagittal* section of the *brain* of *a 56-week-old male mouse hybridized with an anti-*Arl6ip1 *probe (Marques et al. 2011). From* Allan Brain Atlas*, experiment ID: 69526874. (C) Arl6p1 is expressed in various tissues (as marked in blue). From* Gene Expression Database *(GXD), accession number: 1858943.*

ARL6IP1 is the acronym for *ADP-ribosylation factor-like protein 6-interacting protein 1* and was previously referred to as ARMER, the *apoptotic regulator in the membrane of the endoplasmic reticulum* (Lui *et al.* 2003). The latter name already gives insights into its subcellular localisation in the ER membrane and its function of negatively regulating apoptosis via inhibiting caspase-9 function. This protects cells from various exogenous stressors like ER stress causing brefeldin A, tunicamycin and thapsigargin as well as apoptotic inducers such as serum starvation, doxorubicin or UV irradiation (Lui *et al.* 2003). *Arl6ip1* is ubiquitously expressed, but particularly enriched in neuronal tissue (see **Figure 11**, Magdaleno *et al.* 2006, Lein *et al.* 2007).

3.7.2 Previous Studies on ARL6IP1

ARL6IP1 was originally found to be expressed during mammal haematopoiesis (Pettersson *et al.* 2000). Its neuronal importance was shown by its involvement in retinogenesis in zebra fish and mice (Blackshaw *et al.* 2004, Huang *et al.* 2012). It is also expressed in the human retina (Strunnikova *et al.* 2010). In zebra fish it may play a role neural crest development (Huang *et al.* 2009).

ARL6IP1 was also reported as an interaction partner of Addicsin (also termed ARL6IP5), a protein that is able to modulate neuron excitability by attenuating the function of the glutamate transporter SLC1A1 (also called EAAC1 or EAAT3, Akiduki and Ikemoto 2008, Ikemoto *et al.* 2017).

Besides clinical reports (which are subject of the next chapter 3.7.4), knockdown of *Arl6ip1* was recently found to cause significant progressive locomotor deficits in drosophila (Fowler and O'Sullivan 2016). While two independent knockdown strains did not show decreased lifespan, alterations of neuromuscular junctions (NMJs) were observed for both long- and short-projecting neurons (posterior and anterior axons, respectively). In *Arl6ip1*-knockdown flies, the NMJs were more likely to be disrupted. Interestingly, the axonal mitochondria network was disrupted in long-projecting neurons resulting in elongated and less mitochondria whereas short-projecting neurons appeared normal. Fowler and O'Sullivan suggested a model in which the distal ER in axons of *Arl6ip1*-attenuated flies is decreased and less complex, resulting in a reduction of ER-mitochondria contact sites. These sites are important for mitochondria fission which is hence diminished. In fact, experimental overexpression of the GTPase DRP1, which mediates mitochondrial fission, rescues the mitochondria morphology and described general phenotype of *Arl6ip1*-deprieved drosophila while the ER stays disrupted.

Dong *et al.* (2018) recently reported in their cellular overexpression studies a new interaction partner: Inositol polyphosphate 5-phosphatase K (INPP5K or SKIP). It appears that ARL6IP1 is able to recruit INPP5K to the ER membrane as suggested by colocalisation and CoIP experiments. Furthermore, both proteins preferentially localise to the tips of ER tubules compared to luminal or tubular ER markers. The authors also noted an increased abundance of ER sheets upon siRNA-mediated depletion of *ARL6IP1* or *INPP5K* in HeLa cells.

3.7.3 The topology of ARL6IP1 is controversial

The localisation of the C-terminus of ARL6IP1 is controversially discussed within literature. Due to similarity of other membrane-shaping proteins, it was proposed to have two hydrophobic hairpin domains integrating into the ER membrane (Hübner and Kurth 2014, Yamamoto *et al.* 2014). In contrast, Kuroda *et al.* (2013) proposed an ER-luminal C-terminus of ARL6IP1 (see Figure 12).

The latter group cloned variants of ARL6IP1 that had insertions of the redox-sensitive *Gaussia* luciferase (Gluc) on various positions. They stated that if the relative luminescence (normalised to the transfection control with β-galactosidase) was increased, this may indicate an ER localisation at the point of insertion. This is explained by the activity of the Gluc reporter enzyme, and its resulting luminescence, which is roughly 10-fold higher, if Gluc is located within the oxidative environment of the ER compared to cytosolic orientation (Li et al. 2012). They concluded from their studies that ARL6IP1 has a luminal C-terminus.

Nevertheless, several facts point to a cytosolic C-terminus. For example, the C-terminal KKXX motif needs to be cytosolic for proper function (Vincent et al. 1998). Additionally, topology forecast tools like Protter and 11 other topology tools independently resulted in a structure with two hydrophobic hairpin domains. The UniProt database suggests a luminal C-terminus with reference to Kuroda *et al*. Aligning the ARL6IP1 protein sequence against the Protein Families (Pfam) database led to the detection of a reticulum homology domain (RHD) with two lipid bilayer hairpins with high statistical significance. Yamamoto et al. (2014) also identified the RHD.

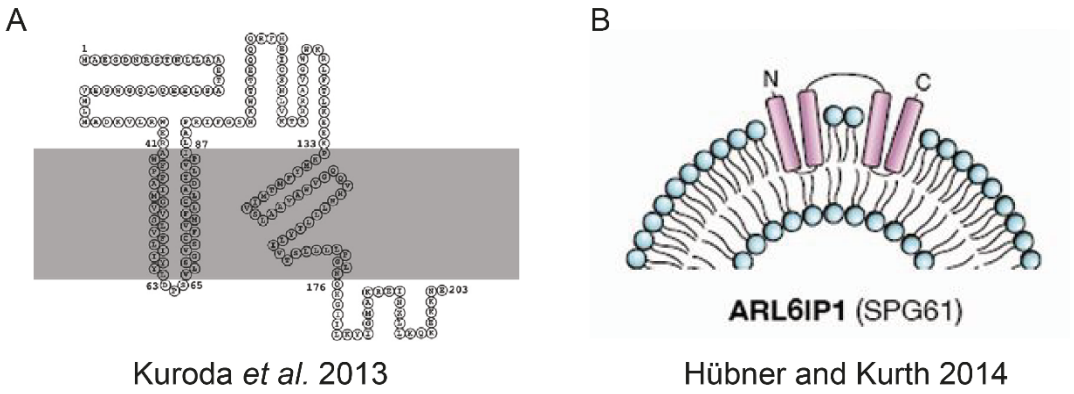

Figure 12: The topology of ARL6IP1 is controversially reported. *While Kuroda et al. (2013) proposed a C-terminus luminal of the ER (A), further literature suggested a topology with two wedge-like reticulon-homology domains resulting in a cytosolic C-terminus (B, Dong et al. 2018, Hübner and Kurth 2014, Yamamoto et al. 2014).*

3.7.4 Clinical relevance and known mutations

To date, there are only a few families with confirmed mutations in *ARL6IP1* (**Figure 13**) with autosomal recessive inheritance, clinically referred as spastic paraplegia 61 (SPG61). So far, only 6 families were reported world-wide. The first published mutation is a deletion of 4 bases at the C-terminus (last 10% of coding sequence), resulting in a frameshift of the triplet code: p.K193F*fs (Novarino *et al.* 2014). This likely results in an altered C-terminus with a later stop codon and subsequent longer protein (228 amino acids) creating another hydrophobic helix. The same mutation was reported later in an independent family (Nizon *et al.* 2018). Recently, a missense mutation was identified at c.92T>C leading to p.L31P, meaning replacing the leucine 31 by proline (Chukhrova *et al.* 2019). There are three mutations known resulting in premature stop codons (c.112 C>T, p.R38*; c.169delC, p.L57*; c.346C>T, p.R116*). As none of these premature stop codons is located within the last exon nor in the last 50 coding base pairs, nonsense-mediated mRNA decay seems very likely (Schweingruber *et al.* 2013) thus leading to a complete loss of the protein. The family with the p38R* variant was reported twice (Maddirevula *et al.* 2019, Wakil *et al.* 2019), whereas p116R* was only found heterozygous but nevertheless classified as pathogenic (Lek *et al.* 2016). p57L* is an entry in the database ClinVar without being formally published.

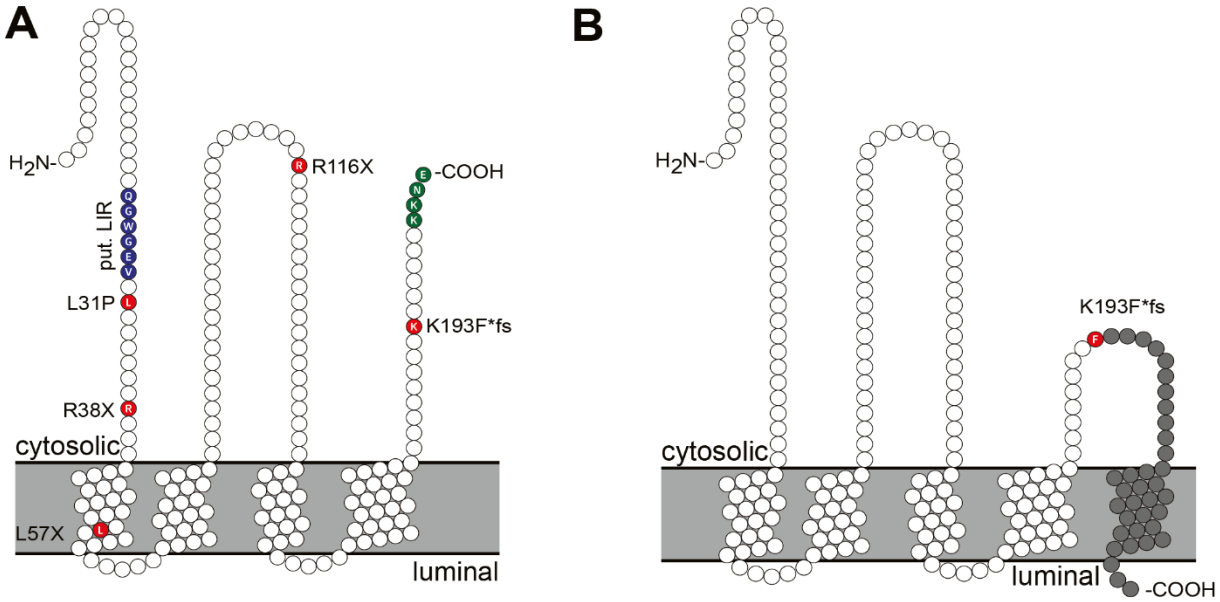

Figure 13: Wild-type and mutated* ARL6IP1 *with its potential topology and integration into the ER membrane. *(A) ARL6IP1 topology model with putative LC3-interacting region motif (blue), sites of clinical mutations (red) and ER retention signal KKXX (green). (B) Potential topology of the frameshift variant ARL6IP1-K193F*fs resulting in a delayed stop codon and an elongated protein. The site of mutation is marked (red) and the frameshift amino acids leading to another hydrophobic helix are pictured in grey. Online tool Protter used for topology and illustration (Omasits et al. 2014).*

All publications describe severe neurological phenotypes. For the p.R38* variant, two homozygous patients with reduced birth weight, microcephaly and dysmorphic features have been reported. Dilated ventricles, enlarged subarachnoid space and partial agenesis of the corpus callosum were seen in Magnetic Resonance Imaging (MRI) for the first, female patient. Furthermore, overriding sutures, small fontanels, prominent nasal bridge, thin lips, microcephaly plagiocephaly, retrognathia, high arched palate, long hands, long fingers, hyper-extendable joints, redundant skin, large feet, severe head lag, absent deep tendon reflexes, and generalized hypotonia were described for the second, male patient. Both died early at 28 or 37 months (Wakil *et al.* 2019).

The frameshift (K193F*fs) and point (L31P) mutations also lead to strong neurological phenotypes such as motor deficits, increased patellar reflexes and spasticity. Patients carrying the L31P mutation exhibit mental retardation, dysarthria, dysmorphic facial features and neurogenic bladder (Figure 14A).

Figure 14: Clinical symptoms of patients. *(A) 6-year-old boy, carrying the L31P mutation, with dysmorphic face (large low-set of ears, macrodontia, microgenia), diffuse muscular hypotrophy and upper limb muscle hypertonia. Cerebral MRI suggests atrophic ventriculomegaly. Modified from Chukhrova et al. (2019). (B) 11-year-old patient with K193F*fs frameshift mutation showing progressive ulcerations, distal finger amputations and osteomyelitis. Modified from Nizon et al. (2018).*

The MRI reveals diffuse cortical and subcortical abnormalities, parietal white matter reduction, secondary atrophic ventriculomegaly with compensated liquor dynamics, and agenesis of the corpus callosum. These patients cannot sit or walk, had an onset of disease at 3 months of age and showed signs of amyotrophy (Chukhrova *et al.* 2019). In contrast to L31P patients, the K193F*fs frameshift mutation did not affect cognition. For those, the disease onset was around 14 months involving a walking ability with support with difficulties, loss of terminal digits and acropathy and acromutilation (Figure 14B). The Achilles tendon reflex was absent.

In summary, mutations in *ARL6IP1* are causative for a severe neurological phenotype that seems to be diverse dependent on the specific mutation. Although the number of described patients is very low and the case studies were prepared by different teams of neurologists, it appears that truncation mutations are most severe with complex course leading to early lethality, while the point mutation L31P had strong locomotor difficulties and mental retardation whereas the K193F*Fs mutation results in acropathy and walking ability with support.

3.8 Aims

In the recent years, clinical findings of loss-of-function mutations of ARL6IP1 shed light on this protein. Studies in zebra fish and drosophila confirmed that Arl6ip1 is required for normal neuronal function. To date, little is known about an actual pathomechanism. For this reason, both *in vivo* studies using an Arl6ip1-KO mouse line and *in vitro* experiments on cellular and protein level were planned to elucidate the Arl6ip1 protein function. In particular, this thesis aimed to:

- Assess a potential protein-protein interaction of ARL6IP1 and FAM134B as suggested by a previous yeast two-hybrid screen.
- Investigate a potential interaction of ARL6IP1 with LC3, in order to evaluate a similar pathomechanism as observed in Fam134B-KO mice.
- Verify the reported self-oligomerisation of ARL6IP1 and possibly narrow down the interaction site.
- Generate and study the effects of disease-causing and truncated ARL6IP1 variants on interactions.
- Establish a suitable assay and evaluate the localisation of the C-terminus as its topology is controversially reported as cytosolic or ER-luminal.
- Characterise the consequences of the disruption of *Arl6ip1* in mice by using a toolbox containing behavioural studies, histology, ultrastructural analysis and *ex vivo* cell cultures.
- Assess the reporter mouse line *Arl6ip1-ER-Tomato-Emx1*.

4 Material & Methods

4.1 Material

4.1.1 Cell lines

Table 1: Cultured eukaryotic cells. *For cultivation details see 4.2.2.1.*

Cell line	Source	Description
COS-7	ATCC: CRL-1651	African green monkey kidney cells expressing SV40 T antigen
HEK293T	ATCC: CRL-1573	Human embryonic kidney cells expressing SV40 T antigen
CB cells	Thomas Braulke, Hamburg	Cerebral cells, fibroblast-like neuronal precursors immortalised with a temperature-sensitive construct
Arl6ip1 WT / KO MEFs	Own work	Mouse embryonic fibroblasts wild-type or deficient of *Arl6ip1*, either primary or immortalised by SV40

4.1.2 Bacteria

For cloning and amplification of DNA plasmids chemically competent cells of the bacterial strain *Escherichia coli* XL1-Blue (recA1 endA1 gyrA96 thi-1 hsdR17 supE44 relA1 lac [F proAB lacIqZΔM15 Tn10 (Tetr)]) were used.

4.1.3 Antibodies

Following primary antibodies were used for immunofluorescence (IF) and immunoblot (IB):

Table 2: List of primary antibodies used for immunofluorescence (IF) or immunoblot (IB). *All were IgG subtype. ms: mouse, rb: rabbit, pc: polyclonal, mc: monoclonal.*

Antigen	Company	Order Number	Application (Dilution)	Species & Clonality
ARL6IP1 (ARMER)	Sigma-Aldrich	PRS3305	IF (1:250), IB (1:500)	rb (pc)
ARL6IP1 (ARMER)	Atlas Antibodies	HPA045307	IF (1:250)	rb (pc)
β-Actin	Abcam	ab6276	IB (1:4000)	ms (mc)
FAM134B	self-made antibody	-	IF (1:250), IB (1:250)	rb (pc)
Gm130	BD Biosciences	610823	IF (1:250)	ms (mc)
LC3B	Cell Signaling	2775	IF (1:250), IB (1:1000)	rb (pc)
Laminin	Abcam	ab11575	IF (1:200)	rb (pc)
LAMP1	Abcam	ab24170	IF (1:1000), IB (1:1000)	rb (pc)
NF200	Sigma-Aldrich	MAB5266	IF (1:250)	ms (mc)
p62	Abcam	ab56416	IF (1:500), IB (1:500)	rat (mc)
PDI	Enzo Life Sciences	ADI-SPA-891	IF (1:250)	ms (mc)
CLIMP63 (CKAP4)	ProteinTech	16686-1-AP	IF (1:250), IB (1:1000)	rb (pc)
CLIMP63 (CKAP4)	R&D SYSTEMS	AF7355	IF (1:20)	sh (pc)
Reticulon 4 (Nogo A+B)	Abcam	ab47085	IF (1:250), IB (1:1000)	rb (pc)
HA-Tag	Roche	11867423001	IF (1:250), IB (1:1000)	rat (mc)
Myc-Tag	Sigma-Aldrich	M5546	IF (1:250), IB (1:1000)	ms (mc)

Antigen	Company	Order Number	Application (Dilution)	Species & Clonality
GFAP	Millipore	MAB360	IF (1:1000)	ms (mc)
NeuN	Millipore	MAB377	IF (1:500)	ms (mc)
Map2	Synaptic Systems	188004	IF (1:1000)	gp (pc)

The following secondary antibodies were used for immunostainings: anti-mouse Alexa 488 (Invitrogen, A11029), anti-rabbit Alexa 488 (Invitrogen, A11008), anti-mouse Alexa 546 (Invitrogen, A11030), anti-rabbit Alexa 546 (Invitrogen, A11010), anti-rat Cy5 (Invitrogen, A10525), anti-sheep Cy5 (Invitrogen, 81-8616). All secondary antibodies were diluted by 1:1000 in 5% NGS/0.25% Triton-X in PBS.

The following horse radish-conjugated secondary antibodies were used in immunoblotting: anti-rabbit (GE Healthcare, NA9340), anti-mouse (GE Healthcare, NA9310) and anti-rat (Abcam, ab97057) at dilutions of 1:4000 in 1% BSA in TBS-T.

4.1.4 Plasmids

Table 3: List of plasmids.

DNA construct	Vector backbone	Source
Empty expression vector	pCIneo	Promega
ARL6IP1-myc	pCIneo	Lab-intern
ARL6IP1-mutLIR-myc	pCIneo	Own work
ARL6IP1-GFP	pCIneo	Own work
ARL6IP1-GFP ΔKKXX	pCIneo	Own work
ARL6IP1-Ret1-GFP (Δ110-203aa)	pCIneo	Own work
ARL6IP1-Ret2-GFP (Δ1-109aa)	pCIneo	Own work
ARL6IP1-L31P-GFP	pCIneo	Own work
ARL6IP1-K193F*fs-GFP	pCIneo	Own work
ATL3-GFP	pCineo_CT_myc	Lab-intern
FAM134B-GFP	peGFP_N2	Lab-intern
FAM134B-GFP	peGFP_N2	Lab-intern
FAM134B-S309X-GFP	peGFP_N2	Lab-intern
FAM134B-GFP Δ C-term (162-497)	peGFP_N2	Lab-intern
GFP-FAM134B Δ N-Term (1-161)	peGFP_C2	Lab-intern
FAM134A-GFP	peGFP_N2	Lab-intern
FAM134C-GFP	peGFP_N1	Lab-intern
(pBSSVD2005) SV40 large-T antigen	Bluescribe (David Ron)	Addgene #21826

4.1.5 Primers

Table 4: List of genotyping primers. T_A: annealing temperature, KI: knock-in, DNA Ctrl: internal control on another genomic target.

Gene Target (T_A)	Primer Name	Primer Sequence	Bands size
Arl6ip1 (64°C)	Arl6ip1_for2	GTAATATTCTGAGCACTGCCT	537 bp = WT 736 bp = *Arl6ip1-flox* 350 bp = KO
	Arl6ip1_WTrev	CTAAGCACAGGCTATGAACC	
	Arl6ip1_rev	TGCCATAATGACCTAATACTGTTGTG	
Emx1-Cre (66°C)	oIMR1084	GCGGTCTGGCAGTAAAAACTATC	~100 bp = KI ~380 bp = WT
	oIMR1085	GTGAAACAGCATTGCTGTCACTT	
	oIMR4170	AAGGTGTGGTTCCAGAATGC	
	oIMR4171	CTCTCCACCAGAAGGCTGAG	
PVALB-Cre (55°C)	140 mKa1-Seq37s	AACAGCAGCGAGCCCGAGTAGTG	214 bp = KI 388 bp = DNA Ctrl
	141 mKa1-Seq37a	TAAGAACTAGACCCAGGGTACAATG	
	142 Cre-Seq7s	AAACGTTGATGCCGGTGAACGTGC	
	143 Cre-Seq8a	TAACATTCTCCCACCGTCAGTACG	
ER-Tomato (61°C)	oIMR9020	AAG GGA GCT GCA GTG GAG TA	196 bp = KI 297 bp = WT
	oIMR9021	CCG AAA ATC TGT GGG AAG TC	
	oIMR9103	GGC ATT AAA GCA GCG TAT CC	
	oIMR9105	CTG TTC CTG TAC GGC ATG G	

4.1.6 Kits

Clarity™ Western ECL Substrate (Bio-Rad; 170-5061)
MycoSpy® (Biontex; M030-050)
NucleoBond® Xtra Midi (Macherey-Nagel; 740410)
Peqlab Plasmid Mini-prep Kit I C line (VWR; 12-6942-02)
Phusion Site-Directed Mutagenesis Kit (Thermofisher Scientific; F530L)
Pierce™ BCA Protein Assay Kit (Thermo Scientific; 23228)
Snooplex® Fast Prep (GVG Genetic Monitoring; SFP-ABC-001)
Zymoclean Gel Recovery Kit (Zymo; D4002)

4.1.7 Enzymes

Alkaline phospatase (Roche; 1071302301)
Phusion High-Fidelity DNA Polymerase (Thermofisher Scientific; F541)
SsoFast EvaGreen (Bio-Rad; 172-5201)
SuperScript IV Reverse Transkriptase (Invitrogen; 18090050)
T4 DNA Ligase (Fermentas; EL0011)
Taq DNA Polymerase (Invitrogen; 10342-020)

Restriction endonucleases for cloning were acquired from Thermo Scientific. Restriction enzymes *Hin*dIII and *Bsp*HI were obtained from New England Biolabs.

4.1.8 Chemicals and Reagents

Acrylamide/bisacrylamide mixture, Rotiphorese® Gel 40 (Roth; A515.1)

Anti-c-Myc Agarose (Thermo Scientific; 20168)
Bromophenol blue (Applichem; A1120.0005)
Brij-35 (Roth; CN21.1)
Chloroquine (Sigma; C6628)
Cresyl violet (Sigma; 860980-5G)
Digitonin (Roth; 4946.1)
DPX Mountant (Sigma; 06522-100ML)
Eosin G Solution 0.5% in water (Roth; X883.2)
Fluoromount-G (Southern Biotech; 0100-01)
GFP-Trap®_A (Chromotek; gta-20)
Glutaraldehyde (GA) (25% solution in water; Serva; 23114.01)
Glyoxal (Roth; 128465-100G)
Hemalun stain according to Mayer (Roth; T865.2)
Hoechst 33258 (Invitrogen; H3569)
Ketamine solution (Inresa Arzneimittel GmbH, 100 mg/ml in 2 ml ampullae)
Normal goat serum (Vector Lab; S-1000)
Orange G (Aldrich; 0-1625)
PageRuler Plus Prestained Protein Ladder (Thermo Scientific; 26620)
Paraformaldehyde (Roth; 0335.3)
PCR-buffer (10x) (Invitrogen; Y02028)
Protease Inhibitor Cocktail Tablets, (Roche; 04693116001)
RNase away (Molecular Bioproducts; 7003)
RNaseOUT (Invitrogen; 10777-019)
S.O.C. Medium (Invitrogen; 15544-034)
TRIzol (ambion; 15596026)
Xylazine solution (Rompun, Bayer, 100 mg/ml)

Further essential chemicals & reagents such as acids, bases, solvents, salts etc. were obtained in life science grade from Roth, Sigma-Aldrich or Fluka.

4.1.9 Cell culture supplies

B-27® Supplement (50X) (Gibco; 17504-44)
β-nerve growth factor (β-NGF) (Preprotec; 450-01)
Bovine serum albumin (BSA), pH 7.0 (PAA; K41-001)
Collagenase II (Worthington; 4176)
Dimethyl sulfoxide (DMSO) (Sigma Aldrich; D2650)
Dulbecco's Modified Eagle Medium (DMEM) with GlutaMAX-I (Gibco; 31966-021)
DNase I (Applichem; A3778)
Earle's Balanced Salt Solution, EBSS (Gibco, 24010043)
Fetale bovine serum (FBS) (biowest; S1810-500)
Hank´s buffered salt solution (HBSS) (Gibco; 14175-053)

Horse serum (Sigma; H-0146)
L-Glutamine (Gibco; 25030)
Lipofectamine®2000 (Invitrogen; 11668- 019)
Minimum Essential Medium (MEM) (Gibco; 31095-029)
Neurobasal-A Medium (Gibco; 10888-022)
OptiMEM (Gibco; 51985-034)
Penicillin-Streptomycin (P/S), (5,000 U/mL; Gibco; 15070-063)
Poly-L-lysine hydrobromide (PLL), (Sigma; P2636)
Trypsin-EDTA (0.05%; Gibco; 25300-54)

4.2 Methods

4.2.1 Molecular Cloning

For this thesis, several constructs were generated via sticky end cloning on the basis of the construct ARL6IP1-myc in pCIneo backbone (see **Table 3**), which encodes human ARL6IP1. Depending on the desired variation, site-directed mutagenesis (ARL6IP1-L31P), truncation by PCR product annealing (ARL6IP1 ΔKKXX, Ret1 & Ret2) or insertion of oligos (Eurofins Genomics) or synthetic DNA fragments (ARL6IP1-K193F*fs) was conducted according to standard cloning procedures. For the ARL6IP1-K193F*fs variant, a fragment of 545 bp was synthesised at GeneCust (Luxembourg) due to lack of suitable restriction sites. Endonucleases (restriction enzymes) were used according to the manufacturer protocols. For ligation, T4 DNA Ligase was used. Clones were tested by slot lysis, test digests or by PCR and verified by Sanger sequencing (Microsynth Seqlab and Macrogen). Finally, modified ARL6IP1 constructs were reintroduced into the pCI-neo backbone to minimize backbone effects on expression levels. The software SnapGene was used for planning cloning steps as well as alignment of Sanger sequence traces.

4.2.2 Primary and immortalised cell culture techniques

4.2.2.1 General cell culture and handling

Used cell lines are listed in section 4.1.1. Human embryonic kidney 293T (HEK293T) cells, COS-7 cells as well as primary or immortalised WT and *Arl6ip1*-KO mouse embryonic fibroblasts (MEFs) were maintained at 37°C with 5% CO_2 and maximum humidity in DMEM medium supplemented with 10% fetal bovine serum (FBS) and 100 U/ml penicillin and streptomycin. Due to the immortalisation by the heat-sensitive SV 40 variant (ts*101), cerebral cells (CBC) were incubated at 33°C with DMEM containing 4.5 g/l glucose, 10% FBS, 24 mM KCl, 2 mM glutamine and the

same standard antibiotics. For starvation, cells were incubated in Earle's Balanced Salt Solution (EBSS) lacking nutrients. Treatment with the inhibitor chloroquine (50 µM) was conducted for 18 h. For freezing, cells were resuspended in 1.8 ml of freezing medium (45 % growth media, 45% FBS and 10% DMSO), transferred into cryo vials (Thermo Scientific, 368632) on ice and slowly frozen in a freezing container (Mr. Frosty, Thermo) at -80°C. For long-term storage, cells were stored in the vapour phase of liquid nitrogen. All cells in culture were frequently checked for mycoplasma using the MycoSpy mycoplasma detection kit.

4.2.2.2 Transient transfection & Immunofluorescence

Cells were transfected using Lipofectamine 2000 according to the manufacturer's protocol at least 20 h after seeding and cultured for further 24 h before lysis or fixation. For immunocytochemistry, cells were seeded in 24-well plates on coverslips with 14 mm diameter (0117580, Marienfeld).

4.2.2.3 Isolation, culture and immortalisation of mouse embryonic fibroblasts (MEFs)

Primary MEFs were isolated at day E13.5. Embryos resulted from timed heterozygous mating. Briefly, brain, eyes and inner organs were dissected from the embryos and processed for parallel genotyping (see 4.2.6) whereas the remaining tissue was washed in PBS. The sterile-washed tissues were minced on a cell culture plate using a sterile scalpel followed by addition of 2 ml DMEM supplemented with 100 U/ml penicillin and streptomycin (=P/S). The resulting suspension was further homogenised by pipetting with a syringe mounted with cannulas of decreasing inner diameter (0.9, 0.8, 0.7, 0.6, 0.55 and 0.4 mm). Next, 5 ml of 0.05% trypsin/EDTA supplemented with DNase I (final concentration 80 µg/ml) were added to the samples and incubated at 37°C for 10 min with occasional shaking. The supernatant containing dissociated cells was transferred into a new tube whereas the remaining tissue was incubated with trypsin/EDTA and DNase I as before. These steps were repeated until a total volume of 40 ml of dissociated cells per sample was collected. Genotyping results were usually available at this time, allowing the selection of WT and KO cells, respectively. Cell suspensions were pelleted at 240 *g* for 10 min and resuspended in 2 ml MEF plating media (DMEM with 20% FBS, 1.2% MEM, P/S). After cell counting, roughly $5 \cdot 10^6$ cells were seeded on dishes (⌀ 20cm) and cultured. Following two passages, cells were either stored (primary cells) or immortalised by transfecting the SV40 large T antigen plasmid and subcultured for further 10 passages.

4.2.2.4 Isolation and culture of dorsal root ganglia (DRG) neurons

Primary DRG neurons were isolated and cultured as described in Heinrich *et al.* (2016). In short, adult mice were sacrificed by cervical dislocation, DRGs were extracted from the spinal cord and rinsed 3 times with Hank's buffered salt solution (HBSS, w/o Ca^{2+} and Mg^{2+}) followed by an incubation in collagenase solution (3 mg/ml solved in HBSS) for one hour at 37°C. Additionally, activated trypsin was added to a final concentration of 0.1% for further 10 min incubation at 37°C. DRGs were rinsed 3 times with HBSS and then dissociated by using BSA-blocked, fire-polished glass Pasteur pipettes of decreasing diameters. The single cell suspension was centrifuged for 5 min at 160 *g* and supernatant was removed from the cell pellet. DMEM containing 10% horse serum was added to the cell pellet and again centrifuged for 5 min at 160 *g*. The supernatant was carefully removed and cells were resuspended in Neurobasal-A medium supplemented with 2 mM L-glutamine and 2% B27. Cells were plated on poly-L-lysine-coated cover slips for analysis by immunocytochemistry (ICC, see 4.2.13.1) or in T25 cell culture flasks for analysis by electron microscopy (EM, see 4.2.14.1) and placed at 37°C in a 5% CO_2 atmosphere. Thirty minutes after plating, medium was replaced by fresh culture medium containing β-NGF (50 ng/ml) to remove glia cells and to induce neurite outgrowth.

4.2.3 Fluorescence Protease Protection (FPP) Assay using live cell imaging

This assay is based on Lorenz *et al.* (2006). In short, 75,000 COS-7 cells were seeded on 0.1 mg/ml poly-L-lysine (PLL) coated 18 mm coverslips (0117580, Marienfeld) in 12-well plates. On the next day, the transfection of several constructs was performed with Lipofectamine 2000. Two days later, the cells were washed with pre-warmed *Intracellular Buffer* (50 mM HEPES pH 7.5, 23 mM NaCl, 3 mM $MgCl_2$, 100 nM $CaCl_2$, 1 mM EGTA and freshly added 107 mM K-Glutamate, 1 mM ATP and 2 mM DTT) and transferred to a heated perfusion chamber filled with the same buffer. Live cell imaging for both GFP and RFP was initiated on a Zeiss Cell Observer Z1 with a frame every 20 s starting with a pre-permeabilisation image followed by manual administration of 18 µM digitonin. After further 60 s, the buffer was replaced by *Intracellular Buffer* containing 6 mM freshly added trypsin. The concentrations for usage of both digitonin and trypsin were previously titrated in pilot experiments fitting to the time frames observed. The analysis of time series made use of ImageJ by drawing the outline of the respective cell and measuring the mean cell fluorescence intensity for each frame subtracted by the background intensity taken from a cell-free spot of the same frame (as background fluorescence changed

upon cell lysis). For further analysis, the area under the curve (AUC, integral) and decay (τ) was calculated for all experiments in a time range of 160 to 720 s.

4.2.4 Co-immunoprecipitation

HEK293T cells were seeded on 10 cm dishes and transfected the next day with Lipofectamine 2000 (Invitrogen). The next day, the transfection efficiency was verified by assessing GFP expression with a microscope. After one more day, the dishes were placed on ice, twice rinsed with ice-cold PBS twice, residual buffer was removed and 1 ml *Lysis Buffer 3* (10 mM KPO_4, 1 mM EDTA, 5 mM EGTA, 10 mM $MgCl_2$, 50 mM Orthoglycerophosphate, 0.5% NP-40, 0.1% Brij 35, 0.1% deoxycholic acid, 1 mM Na_3VO_4, protease inhibitor cocktail (cOmplete, Roche), 1 mM PMSF) was applied. Cells were harvested with a cell scraper. The lysate was incubated for 15 min on ice before centrifugation for clearance (12,000 *g*, 4°C and 30 min). At this point, a part of the sample (20 µl) was supplemented with sample puffer (6% SDS, 33% β-mercaptoethanol, 40% (v/v) glycerol and bromophenole blue), boiled for 5 min at 95°C and stored at -20°C as input control. The remaining volume was used for co-immunoprecipitation. For this, equilibrated pre-coupled agarose beads directed against the myc- or GFP-tag, respectively, were added to the cell lysate (anti-c-myc Agarose, Pierce Biotechnology and GFP-Trap, Chromotek GmbH). The suspensions were incubated on a tube rotator at 4°C overnight. The next day, the beads were sedimented (3000 *g*, 4°C, 5 min), the supernatant removed and washed with ice-cold lysis buffer for 3 times before the residual liquid was removed. 25 µl sample buffer were added to the beads and tubes were boiled at 95°C for 5 min. Resulting samples were stored at -20°C until usage.

4.2.5 SDS-PAGE, protein blotting and immunodetection

Protein concentration of lysates was measured with the bicinchoninic acid (BCA) assay (Pierce) following the instructions of the manufacturer. The absorbance was measured with a spectrometer (NanoDrop 2000, Thermo) with a fresh BSA serial dilution as reference. If applicable, samples were adjusted to 20 or 40 µg in 15 µl by adding the original buffer and finally supplemented by 3 µl sample buffer (6% SDS, 33% β-mercaptoethanol, 40% (v/v) glycerol and bromophenole blue). If not stated otherwise, samples were incubated at 95°C for 5 min before loading. SDS-poly acrylamide gels (Mini-PROTEAN, 1 mm thickness, Bio-Rad) with stacking gel and

8%, 10%, 12% or 15% resolving gel were manually casted according to the manufacturer's protocol, stored for a day at 4°C and mounted in the Mini-PROTEAN®3 System (Bio-Rad) filled with electrode buffer (25 mM Tris, 250 mM Glycine, 0.1 % SDS). A pre-stained marker was used as size standard (PageRuler, Thermo). The proteins were initially separated slowly at 15 mA for 15 min and then at higher voltage of 80-100 V. The electrophoresis was stopped at the desired time and prepared for a tank blot (Mini Trans-Blot, Bio-Rad) with either a nitrocellulose (Amersham Protran 0.45 µm NC) or methanol-activated PVDF membrane (Amersham Hybond P 0.45 PVDF) and by equilibrating all parts of the sandwich for 10 min in ice-cold blotting buffer (25 mM Tris, 192 mM Glycine, 20% Methanol). Proteins were transferred within 1 h at 280 mA. Membranes were blocked with TBS-T (Tris-buffered saline with Tween, 20 mM Tris, 150 mM NaCl, 0.1% Tween 20, pH 7.5) supplemented with 1% BSA for 1 h. Primary antibodies diluted in 1% BSA in TBS-T were incubated overnight. Later, membranes were washed 3 times (1, 5 & 10 min) with TBS-T with subsequent incubation of the secondary antibody in 1% BSA in TBS-T for 1 h at RT. After further 3 washing steps (1, 5 & 10 min) and a brief rinsing with ddH_20, membranes were incubated with ECL solution (Bio-Rad) according to the manufacturer's protocol and signals detected in a LAS 4000 automated detection system (GE Healthcare).

4.2.6 Transgenic mouse models

4.2.6.1 Disruption of Arl6ip1 *in mice*

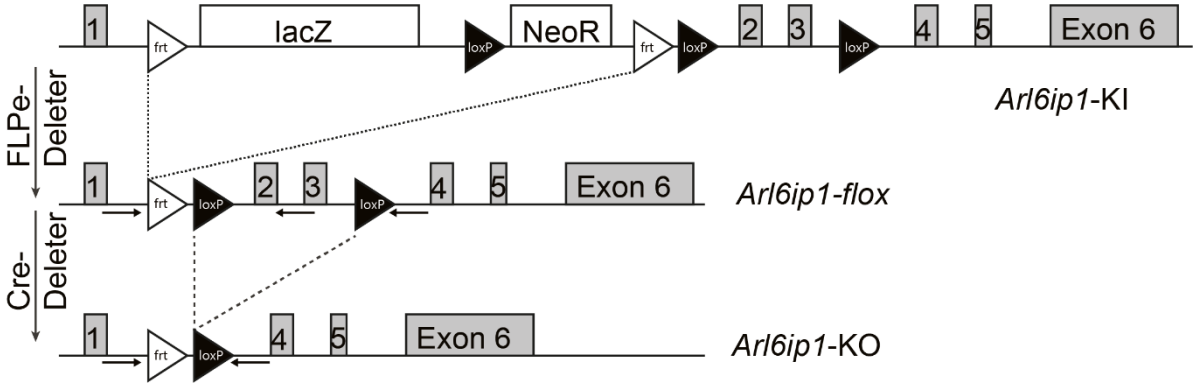

Figure 15: Generation of Arl6ip1-KO ***via*** Arl6ip1-flox ***by breeding with FLPe- and Cre-Deleter.*** *Black and white triangles indicate* loxp *and* frt *sites, respectively. Arrows indicate binding sites of used genotyping primers.*

To generate *Arl6ip1*-deficient mice the EUCOMM embryonic stem cell clone HEPD0752_7_A11 (Source Bioscience) was obtained. This clone carries a disrupted *Arl6ip1* gene by insertion of a cassette into intron 1, containing a lacZ reporter gene and a Neomycin resistance, which is

flanked by frt sites and includes a loxp site at the 3' end. Another loxP site was located in intron 3. This ES-cell clone is suitable for constitutive, conditional and reporter mouse strains, depending on mating with Cre- or FLPe-Deleter mice. The ES cells were injected into C57BL/6 donor blastocysts and transferred into foster mice by Katrin Schorr. Resulting chimeras were mated with C57BL/6 to test for germline transmission. Transgenic mice were subsequently mated with FLPe-Deleter mice (Farley *et al.* 2000) to remove the LacZ and neomycin resistance cassette. Resulting offspring were mated with Cre-Deleter mice (Schwenk *et al.* 1995) to obtain the knock-out of exons 2 and 3 (**Figure 15**). The predicted transcript leads to a frameshift and a premature stop codon after 14 aa and thus very likely results in nonsense-mediated mRNA-decay. Mice examined in this study were at least backcrossed for three generations.

4.2.6.2 Generation of the ER-reporter mouse line Arl6ip1-ER-Tomato-Emx1

Mice heterozygous for *Arl6ip1*-KO were mated with mice expressing the fluorescent protein KDEL-Tomato within the ER lumen under control of the EMX1 promoter, which were generated by Milena Žarković in our laboratory. Briefly, the Tomato cDNA contains a KDEL-motif leading to localisation in the ER. Additionally, the ER-Tomato construct contains a floxed stop cassette prior to the tdTomato-KDEL cDNA leading to tomato expression in cells with Cre recombinase expression exclusively (**Figure 16**). ER-Tomato were mated with double transgenic constitutive *Arl6ip1*-KO; *Emx1-cre* mice. Triple transgenic mice were bred to obtain *Arl6ip1*-WT or -KO mice in combination with *ER-Tomato* and *Emx1-cre* transgenes. At the time of investigation, first animals were available for analysis.

Figure 16: Generation of an ER-Tomato reporter line. *ER-resident tdTomato-KDEL (ER-Tomato) was generated by Milena Žarković. Note the floxed stop codon which can be removed by cell-specific Cre recombinase. Hence, mice were bred with* Emx1-cre *mice for cell type-specific expression of ER-Tomato (additionally to transgenic mice heterozygous for* Arl6ip1*-KO). Black triangles illustrate loxP sites. Arrows indicate binding sites of used genotyping primers.*

4.2.6.3 Genotyping

Genotyping was performed on genomic DNA extracted from tail biopsies by an alkaline lysis protocol (Truett *et al.* 2000) by conventional PCR (Table 4). PCR products were separated by 1.5% agarose gel electrophoresis.

4.2.7 Phenotypic analysis

For all experiments littermates were used that resulted from breeding mice that were back-crossed for at least 3 generations. Experimental procedures were approved by the TLV under registration number 02-055/14. To minimize variation, experiments were conducted by the same experimenter and during similar hours to avoid effects of the circadian cycle.

4.2.7.1 Beam-walk Test and Foot-Base Angle Measurement

The beam-walk test allows to quantify the motor function of the foot abduction by quantifying the foot-base angle. For this, mice were placed on a beam in 15 cm height with 1 m length and 4 cm width with the home cage at the far end of the beam as motivation. A camera recorded the mouse during its movement from behind. The obtained videos were used to determine foot-base angle, missteps during walking and fall-offs. Mice were habituated for three consecutive days to the experimental environment followed by further 2 days of measurement. The habituation was conducted stepwise with a distance of 35 cm, 60 cm and three repeats of 100 cm to the home cage. For analysis of the foot-base angle sequels of at least three proper steps were assessed. For this, genotype-blinded frames of the moment when toes were still touching the beam surface were analysed. For this, a line was drawn along the foot-base (heel to third toe) and another one parallel to the beam surface. The angle between both cutting lines defined the foot-base angle and was assessed using the ImageJ angle tool. Sequences with at least three consecutive steps were analysed with a minimum number of 32 assessed frames per animal.

4.2.7.2 Grip Strength

This test measures the maximum pull force which a mouse can still hold with its forelimbs. For this, the mouse was lifted on the tail base, brought to a trapeze-shaped handle connected to a force sensor. When the mouse grabbed the handle with the front paws, the mouse was gradually pulled at the tail base away from the device until the mouse released the handle. The measuring device (Grip Strength Meter, Ugo Basile, Italy) gave direct feedback to the experimenter via a ratemeter to ensure a gradual increase of the applied pull force (10 *g*/s). As the peak force is used as read-out, measurements with sudden movements of the animal were excluded. The habituation took place at three consecutive days with three repeats followed by the actual measurement with five repeats at two consecutive days. Between measurements, a break of 2 min was given to avoid exhaustion.

4.2.7.3 Nerve Conduction Analysis

To examine neuron function *in vivo,* nerve conduction properties of sensory and motor neurons were analysed. For this, anaesthetised mice (100 mg/kg ketamine & 16 mg/kg xylazine) of the respective age were placed prostrate on a heating pad (~35°C). Pairs of needle electrodes (tungsten, tip ⌀ 2-3 µm, impedance 0.1 MΩ) were inserted into the tail with 3 cm inter-electrode distance. The caudal motor fibres were recorded by applying an impulse on the proximal pairs of electrodes and by measuring at the distal electrodes and for sensory neurons vice versa (Figure 17). The amplitude of the stimulation impulse was increased stepwise from 1 V to 15 V. Stimulation was conducted in a series of rectangular pulses (amplitude ~20 mA, duration 0.1 ms). The sum action potential was filtered (high-pass filter: cut-off frequency 20 Hz, low-pass filter: cut-off frequency 10 kHz), digitalized (sampling 20 kHz). Signal amplitude and signal latency were measured (Petit *et al.* 2014). Measurements were performed by Dr. Lutz Liebmann.

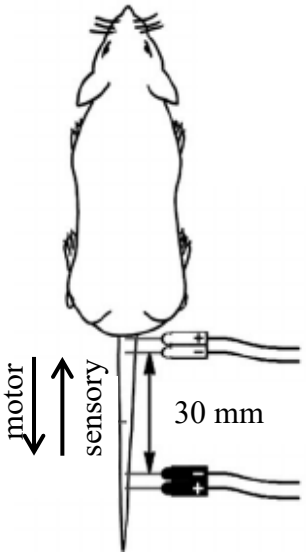

Figure 17: Nerve conduction analysis setup. *Modified from Petit et al. (2014).*

4.2.8 Protein extraction from tissues

Unfixed tissues (brain, spinal cord and muscle) were isolated from acutely sacrificed mice and either snap-frozen in liquid nitrogen for storage at -80°C or processed immediately. For protein extraction, the isolated tissue was chopped with a scalpel on a petri dish in 5 ml per g tissue ice-cold *Tissue Lysis Buffer* (50 mM Tris, 150 mM NaCl, 1 mM EDTA, 1% Triton X-100, 1 mM Na_3VO_4, 1 mM NaF, 2.5 mM Na_2HPO_4, 2.5 mM NaH_2O_4, protease inhibitor cocktail (cOmplete, Roche), 1 mM PMSF), sheared by pipetting with a 1 ml pipette with cut tip and homogenised in an ice-cold 2 ml cylinder with a Teflon plunger in a Sartorius Potter S with 12 strokes at 900 rpm. The tissue homogenate was incubated for 10 min on ice and centrifuged at 3,000 *g* for 10 min at 4°C to pellet cell debris and nuclei. The supernatant was collected, an aliquot diluted 1:10 and 1:20 in 0.1 M NaOH for measurement of the protein concentration and frozen for storage. Protein quantification in lysates, blotting and immunodetection were conducted as described in 4.2.5.

4.2.9 Transcardial perfusion

Mice were deeply anaesthetized and perfused transcardially with roughly 35 ml phosphate-buffered saline (PBS, pH 7.4) followed by 4% paraformaldehyde (PFA) in PBS for 10 min. For electron microscopy, the animals were perfused with 3.9% glutaraldehyde in PBS. After isolation, tissue was post-fixed overnight with the respective fixative on a tumbling roll mixer at 4°C and subsequently washed with PBS.

4.2.10 Tissue sectioning

Depending on the respective tissue and downstream experiments, tissue sections were either cut with a sliding cryotome for free-floating sections, with a cryostat microtome for cryosections mounted on glass slides or, if paraffine-embedded, with a microtome for histological analysis (see next paragraph). For sliding cryotome sectioning, PFA-fixed samples were dehydrated by incubation in 15% and 30% sucrose until sinking, respectively. Free-floating sections of brain (sagittal, 30 µm) or spinal cord (transversal or coronal, 20 µm) were prepared on a Leica SM 2000 R sliding microtome with a sample holder cooled by dry ice and 30% sucrose. For cryostat microtome sectioning, the respective tissues were embedded with OCT (Tissue-Tek, Sakura) in cryomolds and frozen on dry ice. OCT was also used to mount the samples in the cryostat. Sections (brains sagittal, 10 µm or spinal cord transversal, 8 µm) were cut at -12°C specimen temperature and -20 °C blade temperature on a Thermo Scientific CryoStar NX70 cryostat microtome.

4.2.11 Histochemistry

4.2.11.1 Paraffin-embedding and microtome cutting

Spinal cord tissue of paraformaldehyde-perfused mice was wrapped in paper to avoid loss in the next steps and placed in tissue cassettes for dehydration overnight following standard procedures using the Leica Tissue Processor TP1020 Histokinette. After paraffin-embedding at the Leica HistoCora Arcadia, transversal sections of 5 µm thickness were prepared using a Thermo HM355S microtome with waterslide and Cool-Cut. Section series were collected on glass slides and dried. Before staining, the sections were heated to 60°C for 10 min for flattening. Rehydration took place with the following incubation steps: 3 times 10 min xylene, twice 5 min 100% EtOH, 3 min 90% EtOH, 3 min 70% EtOH, 2 min tap water and 2 min dH_2O.

4.2.11.2 Nissl staining

For Nissl staining, 1% cresyl violet solution was heated to 60°C and filtered. The sections were stained for 3 min at 60°C and subsequently washed in dH_2O. Staining differentiation was achieved by 3 min in 90% EtOH with 3 further dehydration steps in 100% EtOH for 2 min each.

4.2.11.3 HE staining

For hematoxylin and eosin stains (HE), rehydrated tissue slides were stained for 3 min in Hemalum solution according to Mayer. After washing in dH_2O, progressive blueing was conducted with 15 min tap water followed by 2 min incubation in dH_2O. Samples were incubated for 3 min in 0.5 % Eosin G solution, rinsed with tap water and dehydrated in an ascending alcohol series with 70%, 90% and twice 100% EtOH for 3 min each. Finally, sections were cleared 5 min in xylene for 3 times, air-dried and mounted with DPX.

4.2.12 Quantification of spinal motor neurons

Images of transversal spinal cord sections stained with cresyl violet were acquired by a Zeiss AxioLab A1. A horizontal line cutting the central canal was drawn, dividing the transversal spinal cord section into a dorsal and ventral half. Nissl-stained cells of the ventral part were counted if the nucleus was visible. For counting, the CellCounter plugin of ImageJ was applied. The unpaired t-test with Welch's correction was applied.

4.2.13 Immunofluorescence

4.2.13.1 Immunostaining of cells and free-floating sections

Cells and tissue sections were stained following a similar protocol. After washing with PBS twice, cells were fixed with 4% PFA for 15 min at room temperature (RT). For tissue staining, free-floating sections of perfused and post-fixed tissue were used and stained in 24-well plates. Both, fixed samples on coverslips or free-floating sections were washed three times with PBS followed by permeabilisation and blocking with 5% NGS/0.25% Triton-X in PBS at RT for 1 h. Incubation with primary antibodies (see **Table 2**) diluted in 5% NGS/0.25% Triton-X in PBS took place overnight at 4°C with gentle shaking. The next day, three consecutive washes with PBS were performed, 10 minutes each, after which the sections were incubated with the respective secondary antibodies for 1 h at RT under light protection while gently shaking. After this, the

samples were incubated with Hoechst 33258 for 10 min followed by three more washing steps with PBS. Free-floating sections were shortly rinsed in 5% NGS/0.25% Triton-X in PBS to reduce folding during mounting, free-floating sections were flattened in PBS, brought on coated glass slides (Histobond, Marienfeld), layered with Fluoromount-G and sealed with coverslips (15747592, Menzel-Gläser). In contrast, the coverslips were inverted and mounted on a glass slide (Superfrost, Thermo Scientific) with Fluoromount-G mounting media.

4.2.13.2 Immunostaining of cryosections on glass slides

Cryosections on glass slides were stained using the Shandon cassette system (Thermo Scientific, 72110017). For this, slides were hydrated for roughly 10 min under mild stirring to remove residual OCT medium and mounted bubble-free with Shandon coverplates. Slides were then permeabilised and blocked in 5% NGS/0.25% Triton-X in PBS, incubated with the primary antibodies in blocking solution overnight at 4°C. Next, slides were washed thrice with PBS, incubated with the respective secondary antibodies in blocking solution for 2 h at RT, incubated with Hoechst 33258 (1:10,000 in PBS), washed twice with PBS and finally mounted with Fluoromount-G and coverslips.

4.2.13.3 Image Acquisition

Images of immunostained cells and tissue were acquired with a confocal microscope (Zeiss LSM 880 with Airyscan). Tissue or cells were imaged at several layers in Z-axis (Z-stacks), which were collapsed for maximum intensity projections (MIPs) for better visualisation. General microscope settings such as laser intensity, pinhole, gain etc. were kept identical between sample sets and were established on secondary antibody control samples. A detection master gain of maximal 750 whereas a digital gain of 1 was used to avoid noise artefacts. Line averaging was enabled (double) and a pixel dwell time of minimum 1 µs was set. Overview images were obtained with a Zeiss Axio Observer Z1 using the tile scan function with stitching. To verify specificity, samples with primary and secondary antibodies were compared to controls that were only incubated with secondary antibodies.

4.2.14 Electron microscopy

4.2.14.1 Ultrastructural analysis of cultured DRG neurons

To preserve the native neuron morphology, a monolayer culture of dorsal root ganglia (DRG) neurons was fixed by the Karnovsky method (Karnovsky 1965), embedded in Epon resin at their

original position in 25-cm^2 plastic culture flasks following the flat embedding procedure (Spoerri *et al.* 1980). After Epon resin polymerization at high temperature, the embedded material was stripped off the plastic flask using needle-nose pliers and forceps. Small circular specimens (≤0.5 cm in diameter) of Epon-embedded material were cut using a drill bit (mounted with a rotating cutting tool) and glued onto supports for ultra-microtome sectioning. Ultrathin sequential sections of 70 nm were cut parallel to the neuron monolayer using an UMT UC7 ultramicrotome (Leica Microsystems) and transferred onto Formvar carbon-coated copper grids for staining using the EM AC-20 contrasting instruments (Leica Microsystems). Electrographs were acquired using a TEM (Cm100- Philips/FEI). Sample handling, image acquisition and subsequent analysis of the ER was performed by Dr. Muriel Mari (Groningen, Netherlands).

4.2.14.2 Ultrastructural analysis of nervous and muscle tissues

Mice were perfused with glutaraldehyde as described before (4.2.9). The fourth lumbal DRG, full length sciatic nerve, thoracic spinal cord and M. gastrocnemius were isolated, post-fixed overnight at 4°C in 3.9% glutaraldehyde and further processed for embedding in epoxy resin. Semi-thin sections were stained with toluidine blue and paraphenylendiamine. Ultrathin sections were contrasted with 0.5% uranyl acetate and 3% lead citrate and examined with a Philips CM10 electron microscope. Sample handling, image acquisition and evaluation was carried out Dr. Istvan Katona and Prof. Joachim Weis (Aachen).

4.2.15 Data analysis & randomisation

Unless otherwise stated, data are presented as mean ± SEM. For statistical analysis of two experimental groups, the samples were evaluated for Gaussian distribution with the Kolmogorov–Smirnov test. If normally distributed, the parametric two tailed Student's t test and if not the nonparametric Mann–Whitney *U* test was applied. If variances differed, the unpaired t-test with Welch's correction was applied. To compare several groups without Gaussian distribution, the Kruskal–Wallis test with Dunn's post-test was used. For experiments that included repeated measurements, differences between groups were surveyed by repeated-measures ANOVA with Bonferroni post-test. Significance was considered at p values <0.05 (*), <0.01(**) and <0.001 (***). Statistics were calculated with GraphPad Prism 5.0. Randomisation and blinding was achieved by using the script *RandomNames* of Jason Faulkner.

5 Results

5.1 ARL6IP1 is an ER-resident protein

The comparison of the human *Arl6ip1* coding DNA sequence with homologs of commonly used model organisms, allows drawing a true-to-scale dendrogram (Figure 18). This verifies a close sequence relation between murine and human *Arl6ip1*.

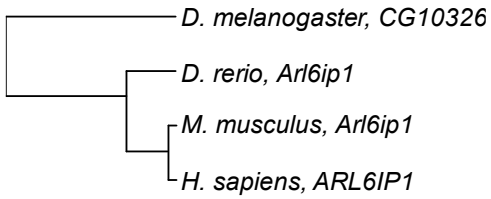

Figure 18: Dendrogram reflecting the DNA sequence homology between species. *For* D. melanogaster*, the* Arl6ip1 *homolog* CG10326 *was assessed.*

The high amino acid sequence similarity between the human and murine Arl6ip1 as studied by BLASTp analysis (https://blast.ncbi.nlm.nih.gov, Table 5) is even more obvious. Indeed, there is only one amino acid position that has unequal properties between man and mice (position 167: human S, murine F). All analysed chordate sequences contain the KKXX motif at the proteins' C-terminus. This motif mediates return of the membrane protein to the ER when recognized within the Golgi apparatus (Jackson *et al.* 1993, Vincent *et al.* 1998). The C-terminal end of the amino acid sequence of *D. melanogaster* Arl6ip1 also has an ER retention signal (XKXX). In summary, the Arl6ip1 sequence is rather conserved and contains an ER retention signal.

Table 5: Homology of Arl6ip1 protein sequences in common animal models versus ***man****. Identity depicts the amount of exact same amino acids in equal order whereas similarity also accounts amino acids with comparable chemical properties.*

	H. sapiens	*M. musculus*	*D. rerio*	*D. melanogaster*
Protein identity	-	96.55%	78.33%	27.92%
Protein similarity	-	99.50%	94.58%	63.55%
Longest isoform	203 aa	203 aa	203 aa	197 aa
ER retention motif	KKNE	KKNE	KKNE	RKLQ

5.2 ARL6IP1 contains putative LC3-interacting region (LIR) domains

5.2.1 The ARL6IP1 protein sequence contains putative LIR domains

LC3-interacting regions (LIRs) are short but versatile motifs. Most common are the WXXL and xLIR motifs, less conserved consensus sequences that can be identified by *in silico* analysis.

When applying the human ARL6IP1 wild-type amino acid sequence to the online tool iLIR (repeat.biol.ucy.ac.cy/iLIR/ (Jacomin *et al.* 2016)) which screens for these domains, six hits were identified (Table 6). The calculated position-specific scoring matrix (PSSM score, Kalvari *et al.* (2014)) allows a ranking of these hits. A higher score indicates a higher probability of the motif to bind to LC3. The e-value represents the probability of random (i.e., unrelated) hexapeptides to achieve a score at least as high as the hit, meaning the smaller the more meaningful is the hit. A PSSM value of 10 was selected as cut-off (cf. the active FAM134B DDFELL motif has a PSSM score of 18) for further screening. Because the motif LTYLIV is predicted to locate within the membrane, it was excluded. A construct of Arl6ip1 in which the motif QGWGEV was mutated to QGAGEA, called ARL6IP1-mutLIR-myc, was established and used for further studies (not shown).

Table 6: Putative LIR motifs found in the human ARL6IP1 protein sequence. *Position-specific scoring matrix (PSSM) scoring and e-value (probability for an random hit) help to rank the hits. Bold residues were mutated to alanine in ARL6IP1-mutLIR-myc.*

MOTIF	START	END	LIR sequence	PSSM score & (e-value)
WXXL	24	29	QG**W**GE**V**	12 (1.1e-01)
xLIR	160	165	LTYLIV	10 (2.0e-01)
WXXL	121	126	GWWKRL	9 (2.8e-01)
xLIR	54	59	LVFLII	6 (7.4e-01)
WXXL	74	79	VMFLCL	6 (7.4e-01)
WXXL	103	108	QRFHEI	4 (1.4e+00)

5.2.2 None of the putative LIR motifs of ARL6IP1 bind to LC3

To verify a potential interaction between ARL6IP1 and LC3-II, ARL6IP1-myc was overexpressed in HEK293T cells for a co-immunoprecipitation (CoIP) with endogenous LC3-II. As it is known that FAM134B has an active LIR domain (Khaminets *et al.* 2015), this protein served as a positive control. Chloroquine was used to inhibit the autophagic flux resulting in the accumulation of autophagosomes and, thus, LC3-I and LC3-II (chapter 3.3.1). Upon IP with beads coupled to antibodies directed against the myc-tag, no LC3-II could be detected via immunoblot in the untransfected or ARL6IP1-myc transfected sample. In contrast, LC3-II was detected in FAM134B-myc overexpressing cells (Figure 19). Notably, LC3-II could be detected in the 2% input control sample before the CoIP. Unintentionally, IgG light and heavy chains of the bead-coupled antibody are visible due to signal detection with a secondary antibody directed against mouse IgG as required for the anti-myc antibody.

These results confirm an interaction between LC3 and FAM134B but not between LC3 and ARL6IP1. A CoIP with ARL6IP1-mutLIR-myc did also show no interaction (data not shown). Hence, these results suggest that there is no direct interaction between ARL6IP1 and LC3-II.

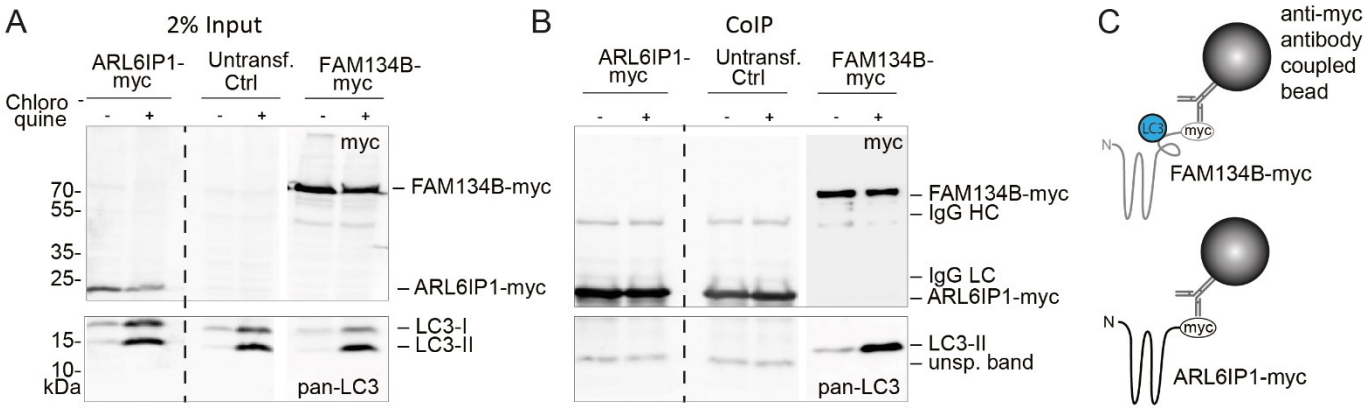

Figure 19: ARL6IP1 does not interact with LC3-II upon chloroquine-induced LC3 accumulation. *(A) Input control (2% of CoIP volume). Upper blot detected with antibody against myc, lower blot against pan-LC3. (B) CoIP using myc beads reveals a strong interaction between FAM134B (positive control) and LC3-II which is increased upon Cloroquine treatment (+) whereas ARL6IP1 does not coprecipitate with LC3-II. Untransfected cell lysates served as negative control (Ctrl). Dashed lines indicate ommitted lanes. Due to space limitations, blotting of FAM134B was conducted on another membrane but treated identical. (C) Cartoon illustrates assay procedures and interaction of LC3 (blue).*

5.3 Interaction studies of ARL6IP1

5.3.1 ARL6IP1 constructs

In this study, several constructs were established based on the pre-existent full length Arl6ip1 (Figure 20). Besides the wild-type, disease-associated variants like the missense point mutation L31P and the frameshift deletion K193F*fs, a construct with destroyed LIR domain (mutLIR) was established and used. Furthermore, truncation of either the ER retention signal (ΔKKNE) or deletions of roughly the C-terminal (Ret1) or N-terminal (Ret2) protein including the respective RHD.

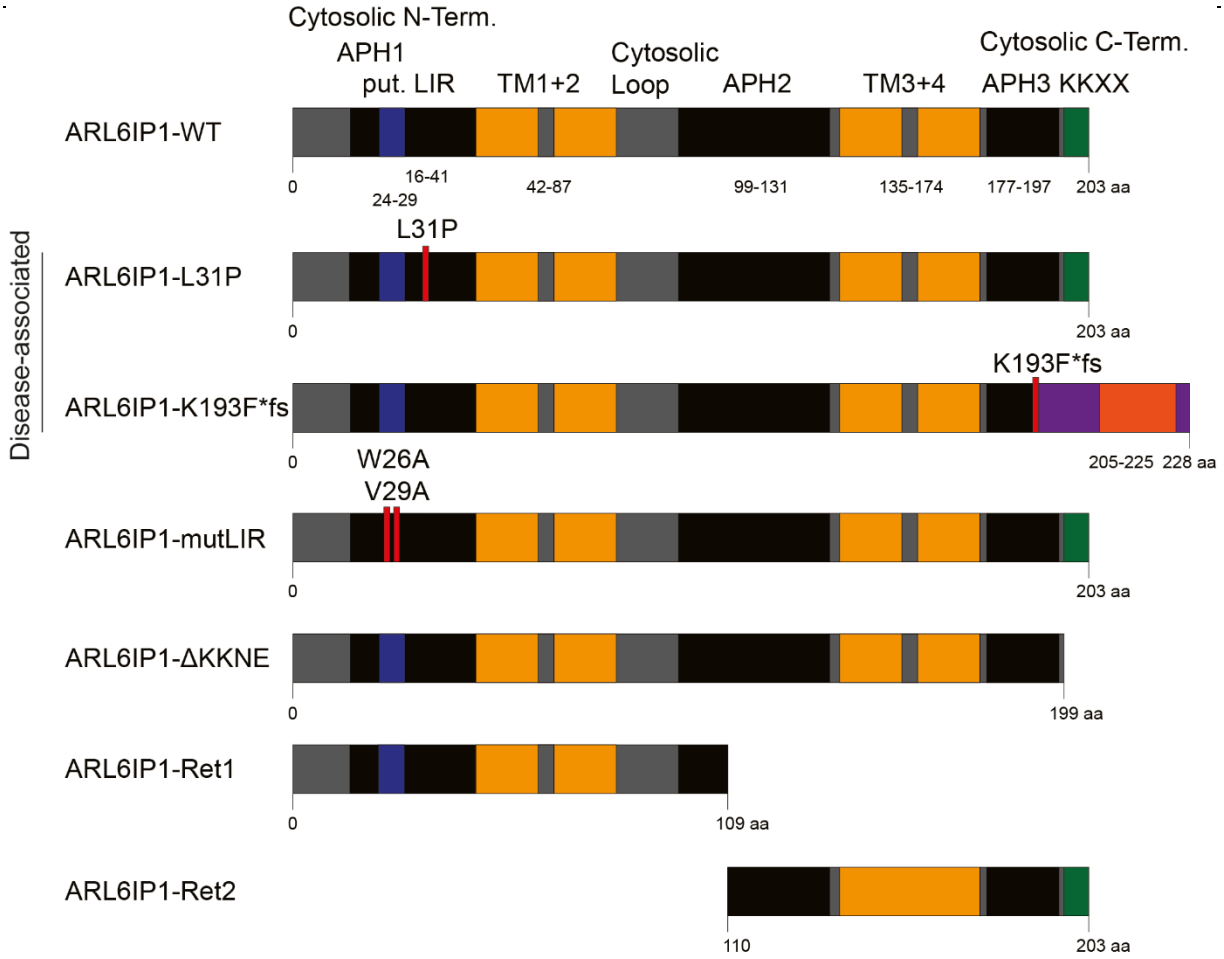

Figure 20: Protein sequences of ARL6IP1 *variants used in this study. Putative LC3-interacting region (LIR) motif (deep purple), transmembrane domains (orange), putative amphipathic helices (black), ER retention signal (green) and sites of mutation (red) are depicted. Frameshifted amino acids are shown in purple with new resulting transmembrane in dark orange.*

5.3.2 The C-terminal half of the protein is necessary for ARL6IP1-ARL6IP1 interaction

ARL6IP1 is known to oligomerise (Yamamoto, 2014). This was also observed in immunoblots while using less stringent conditions (low denaturation temperature or less β-mercaptoethanol, data not shown). CoIP with different ARL6IP1 variants (constructs see **Figure 20**) were performed to narrow down the interaction sites. Although the expression levels of overexpression constructs did vary in the respective input samples, enrichment of respective proteins in pull-down samples suggested interaction. The immunoblots (**Figure 21**) show an interaction of ARL6IP1-GFP, ARL6IP1-K193F*fs-GFP and ARL6IP1-ΔKKNE-GFP with ARL6IP1-myc, respectively. A slight band (asterisks) can be seen on the interaction blots for ARL6IP1-Ret2-GFP which likely reflects an interaction due to the initially low expression of ARL6IP1-Ret2-GFP as seen in the

input blot. No interaction between ARL6IP1-myc and ARL6IP1-Ret1-GFP could be detected. Thus, the C-terminal half of the protein seems to be crucial for oligomerisation of ARL6IP1.

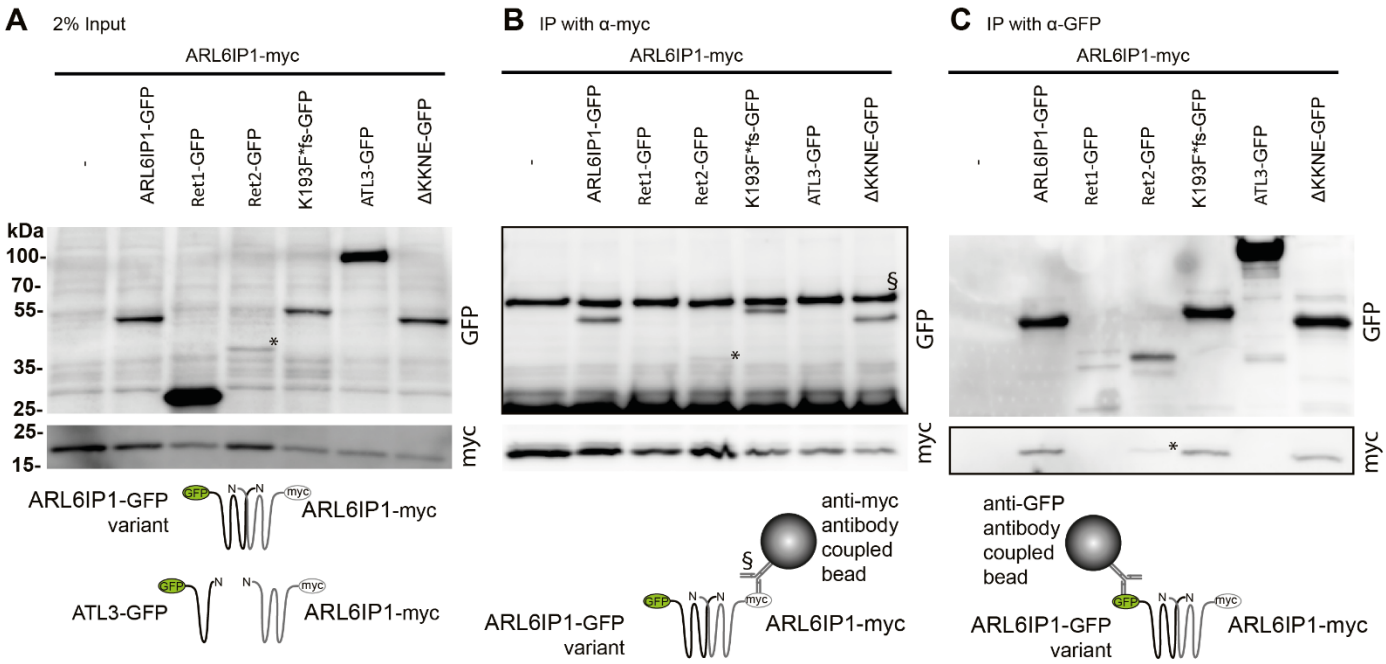

Figure 21: CoIP with ARL6IP1-GFP variants and ARL6IP1-myc helps narrowing down the interaction sites for oligomersiation. *(A) Input control (2%) before CoIP with beads directed against either myc- or GFP-tag. Cartoon illustrates assay procedure. Detecting antibody as labelled on the right side. Asterisks label low signal of Ret2-GFP. (B) CoIP with anti-myc-beads. IgG heavy chain causes strong signal at 55 kDa (depicted with §). Black frames indicate blots picturing the interaction. (C) CoIP with anti-GFP-beads.*

5.3.3 FAM134B constructs

In this thesis, various previously existent constructs of the FAM134 protein family were used. Besides the full-length proteins of FAM134A, B and C, variants of the FAM134B were transfected (Figure 22). This included S309X, a clinically relevant variant with a premature stop codon (Kurth *et al.* 2009) and artificial deletions of either the N-terminal or C-terminal part from the perspective of the cytosolic, intra-RHD loop.

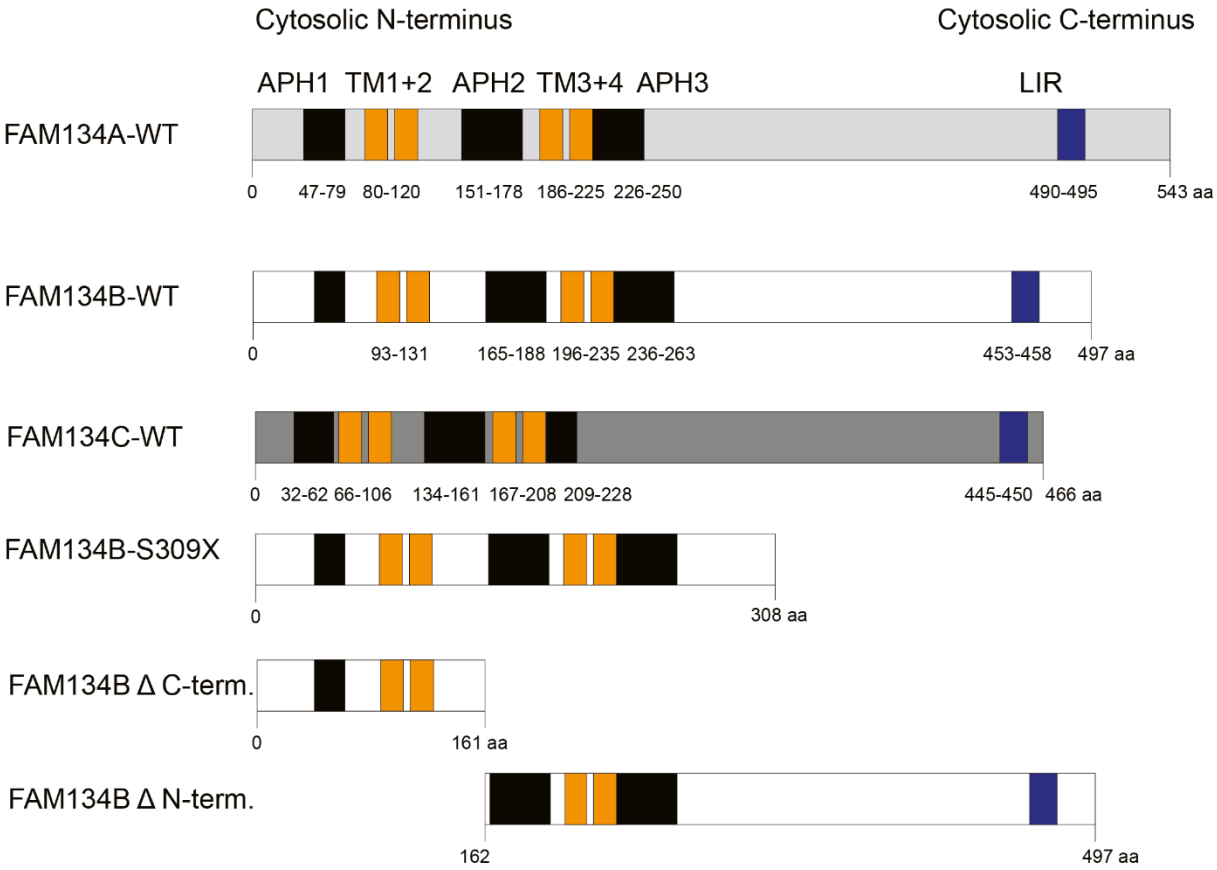

Figure 22: Protein sequences of FAM134 protein family member constructs used in this study. *Full length constructs of the longest isoform of FAM134A, B and C, respectively. Further variants as the disease-associated S309X and large N- or C-terminal truncations of FAM134B were applied. LC3-interacting region (LIR) motif (deep purple), transmembrane domains (orange) and putative amphipathic helices (black) are depicted.*

5.3.4 ARL6IP1 interacts with FAM134 proteins

An earlier yeast two-hybrid screen with full-length FAM134B as bait identified LC3 and ARL6IP1 as binding partners. To verify an interaction with ARL6IP1, all members of the FAM134 protein family (A, B and C) were tested against ARL6IP1 by CoIP. Furthermore, truncated variants of FAM134B such as the disease-associated S309X and constructs with deletions of the N- or C-ter-

minus (see **Figure 22**) were included in this assay. The pulldown experiment indicates a prominent interaction of all FAM134 protein family members with ARL6IP1 (**Figure 23**). Deletion constructs suggest that ARL6IP1 interacts with the N-terminal part of FAM134B. Consistent with this notion, no interaction could be observed with the FAM134B construct missing the N-terminal amino acids 1-161. To provide a negative control in this pulldown assay, another ER-resident membrane protein with hydrophobic domains, ATL3-GFP, was included as negative control. With this the CoIP buffer and CoIP procedure was established to eliminate false positive hits. The negative interaction for ATL3-GFP and ARL6IP1 proved that the CoIP buffer and general procedure applied for this experiment did not produce false positive hits.

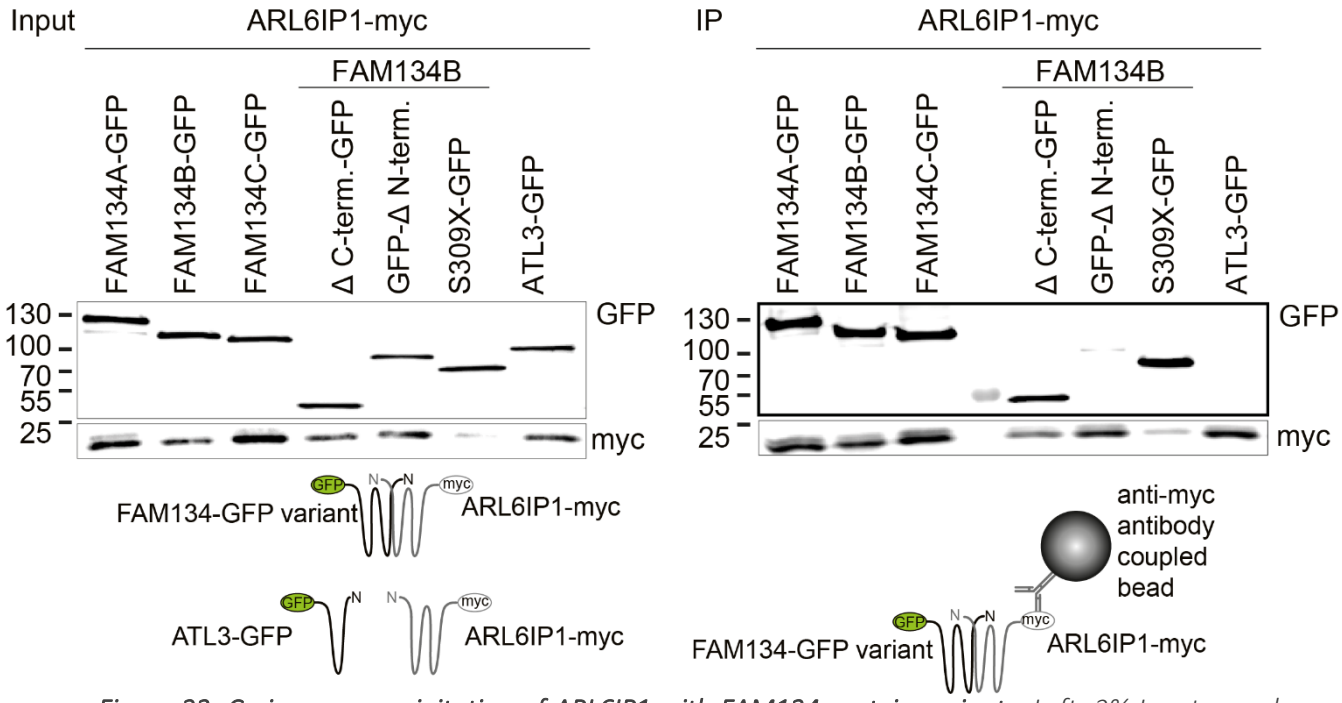

Figure 23: Co-immunoprecipitation of ARL6IP1 with FAM134 protein variants. *Left: 2% Input sample. Right: IP. All FAM134 protein variants interact except N-terminal deleted FAM134B. ATL3 served as negative control. Bold framed blot shows interaction. Cartoon illustrates experimental procedure.*

5.3.5 ARL6IP1 variants interact with FAM134B

Vice versa, mutated and truncated ARL6IP1 variants were tested against FAM134B to narrow down the regions required for an interaction. Surprisingly, besides minor mutations like L31P or a frameshift in the very C-terminal end even large truncations such as deletion of the first or second half of protein still seem to interact while the negative control ATL3 or pure GFP show no interaction (**Figure 24**).

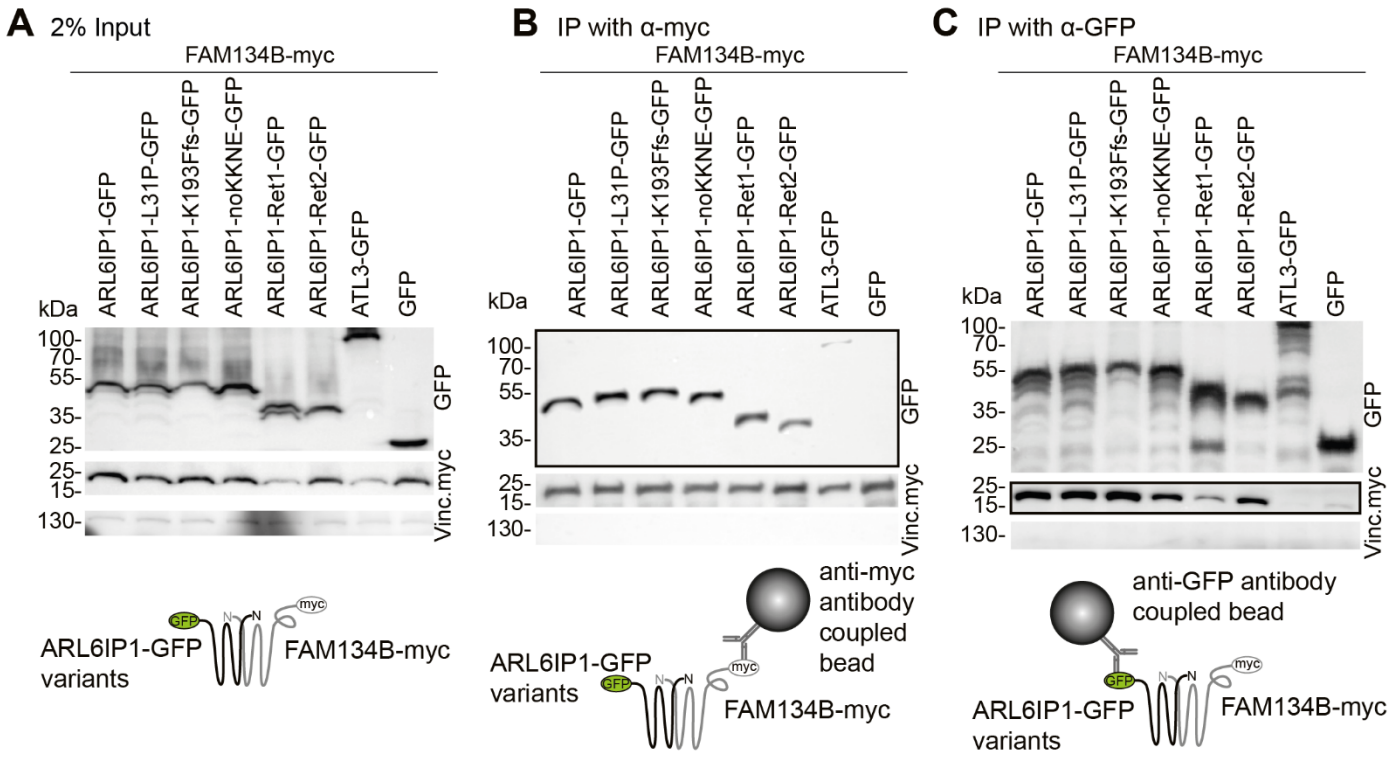

Figure 24: ARL6IP1 variants were tested for interaction with FAM134B. (A) 2% input sample. (B) IP by myc. (C) IP by GFP. Black frames indicate blot with interaction. Lower: Illustration depicts experimental condition.

5.4 ARL6IP1 colocalises with FAM134B

When overexpressing both ARL6IP1-myc and FAM134B-HA in mouse embryonic fibroblasts (MEFs) and immunostaining for the respective tags, a clear colocalisation between the overexpressed proteins was observed (**Figure 25**). In comparison to ARL6IP1, FAM134B is overrepresented at the perinuclear ER. Clinical relevant ARL6IP1 variants such as the clinical relevant mutations L31P (point mutation) and K193F*fs (frameshift mutation) still show an ER-like morphology and colocalise with FAM134B. This indicates that the localisation and interaction of these variants is not impaired. In some cells with strong overexpression of ARL6IP1 constructs changes in ER structure (“blobs”) with strong ARL6IP1 singal were observed. These structures were classified as overexpression artefacts and excessively overexpressing cells were excluded from further analysis.

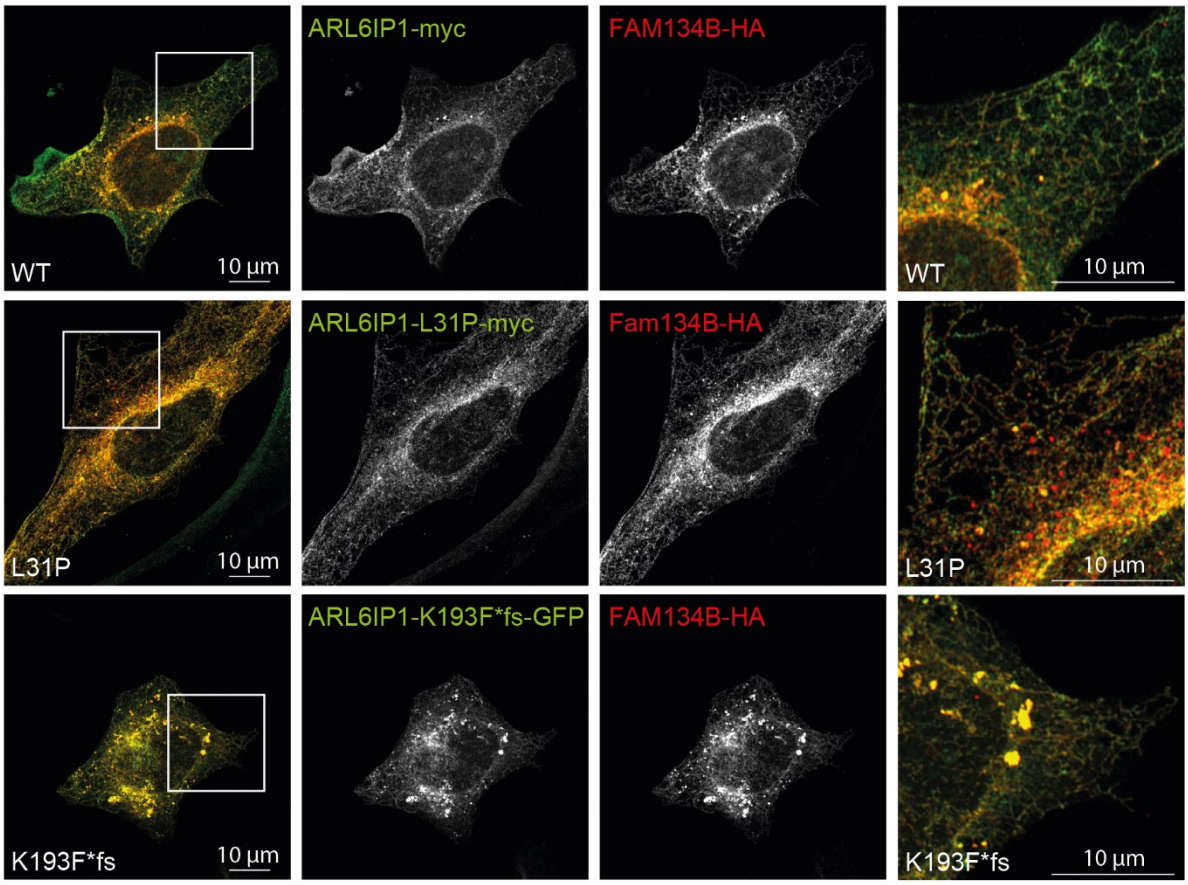

Figure 25: Co-staining of transiently overexpressed ARL6IP1 variants and FAM134B in MEFs*. In overlay images, ARL6IP1 variants are shown in green whereas FAM134B-HA is displayed in red. Colocalisation of FAM134B is given in perinuclear and distal ER for the Arl6ip1 WT as well as the disease associated variants L31P and K193F*fs. Maximum intensity projections (15 slices) with total Z-thickness of 3 µm.*

5.5 Structural analysis

ARL6IP1 is a rather short protein with only 203 amino acids (aa) containing two hydrophobic domains. To further elucidate the protein's function, physical properties and topology were examined.

5.5.1 ARL6IP1 contains amphipathic helices

Not only reticulon domains, but also adjacent regions are important for the actual membrane shaping ability of reticulon homology domains (Brady *et al.* 2015). For instance, helices semi-integrating into the membrane surface, can serve as lever enhancing the shaping ability of the protein (Breeze *et al.* 2016). These amphipathic helices (APHs) consist of an α-helix with predominantly hydrophobic amino acid residues on one axial side and hydrophilic residues on the opposite helix side**.** An APH C-terminal of the second RHD was mentioned for ARL6IP1 by Brady *et al.* (2015).

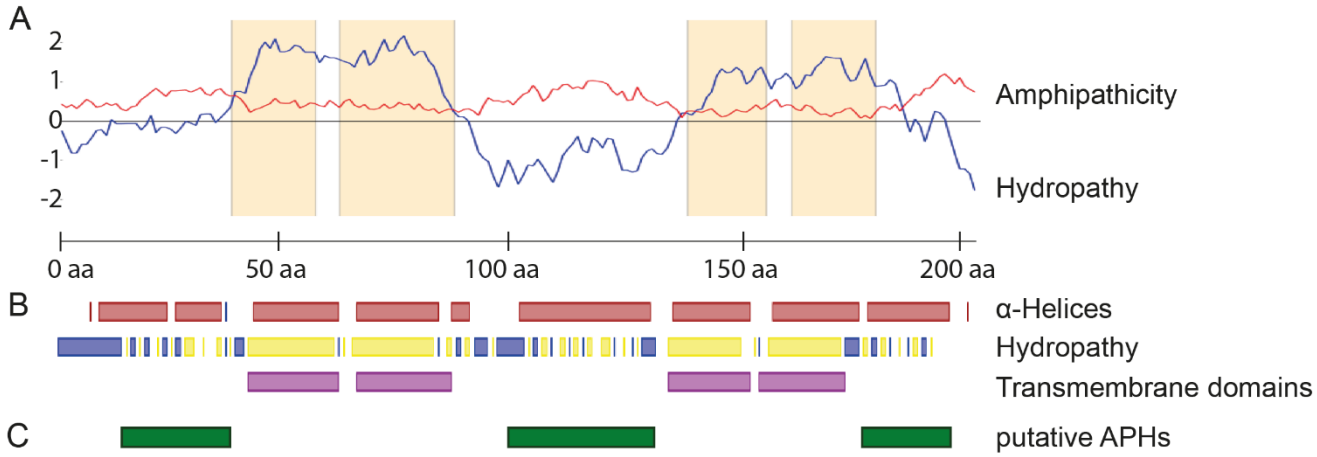

Figure 26: ARL6IP1 contains amphipathic helices. *(A) Hydropathy (blue) and amphipathicity (red) screening as conducted with the web-based tool WHAT 2.0. (B) Query for the amino acid sequence of ARL6IP1 in PredictProtein. Marked are the α-helix secondary structure (red), hydrophilic (blue) and hydrophobic (yellow) stretches as well as transmembrane domains (violet). (C) Assessment of α-helical stretches with HeliQuest resulted in three APHs (green). All distances refer to the amino acid (aa) scale in the middle.*

Screening the ARL6IP1 sequence with the Web Based Hydropathy and Amphipathicity predictions (WHAT 2.0, tcdb.org/progs/?tool=hydro, analysis window 15 aa) revealed the presence of such amphipathic sectors in regions close to the reticulon domains (**Figure 26**A). After verification by PredictProtein (https://open.predictprotein.org/) whether these sectors consist of α-helices, they were assessed with the online tool HeliQuest (heliquest.ipmc.cnrs.fr, settings: α-helix, analysis window 1 turn) to confirm the amphipathic properties (**Figure 26**B). When the hydrophobic moment (µH) was higher than 0.2 (the µH of Rtn1-4 APHs range between 0.248 and 0.293), the region was classified as APH (Figure 26C).

Three differently sized regions with putative APHs were found: N-terminal of the first RHD (aa 16-41), between the RHDs (aa 99-131) and C-terminal of the second RHD (aa 177-197). The latter was described previously by Brady *et al.* (2015). More detailed information about the APH characteristics can be found in **Figure S1**.

5.5.2 FPP assay suggests a cytosolic C-terminus of ARL6IP1

To understand the topology of ARL6IP1, a fluorescence protease protection assay was conducted. Briefly, fluorescent tagged proteins are overexpressed in cells followed by the application of digitonin, an agent predominantly permeabilising the cell membrane, with subsequent addition of the protease trypsin. If the fluorescent protein tag is located in the cytosol, it is accessible by the protease and its signal is quenched shortly upon trypsin administration. If located in the lumen of an organelle i.e. ER, the fluorescence signal is more stable during live cell imaging. For evaluating the latency of quenching, proteins with known topology (such as CD3-RFP, RFP-KDEL and FAM134B-GFP) were added as reference. When assessing ARL6IP1-GFP, it turned out that the attached GFP is rapidly quenched, but not as fast as CD3-RFP or FAM134B-GFP (**Figure 27**). For a more detailed analysis of the curves, the area under curve (AUC) and decay (τ) in seconds was calculated upon trypsin administration (140 s, **Table 7**). When comparing the dynamics of ARL6IP1-GFP with that of the control proteins, it appears that the GFP fused to ARL6IP1 is broken up quickly but not as rapidly as the fluorophores linked to FAM134B or CD3. The luminal fusion protein RFP-KDEL is mostly protected from proteases and hence shows a slow decline of mean fluorescence intensity. These results strongly suggest a cytosolic C-terminus of ARL6IP1.

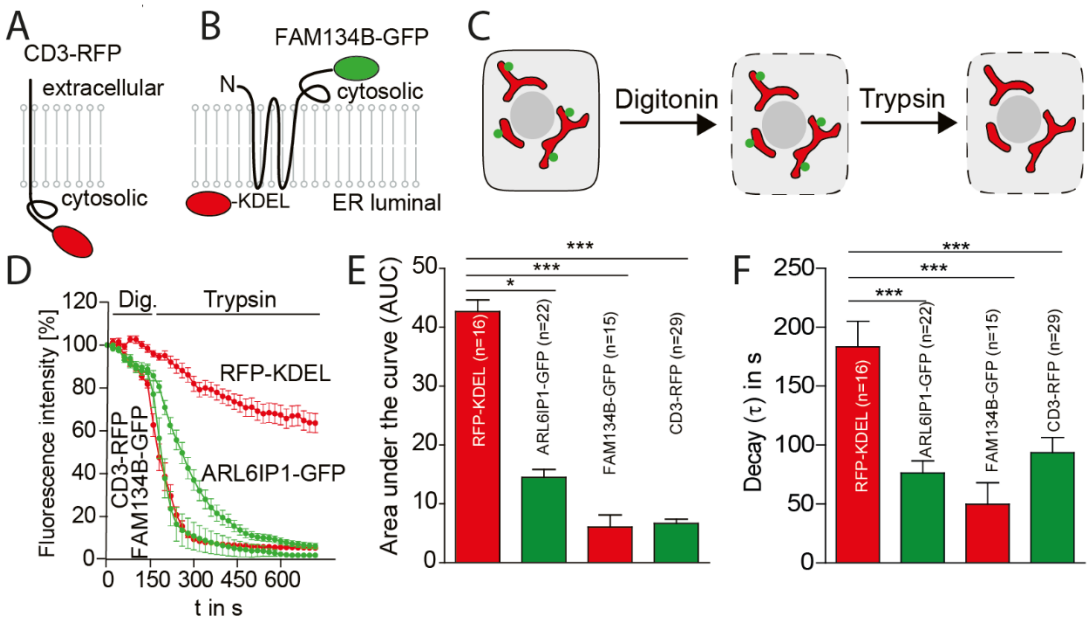

Figure 27: The fluorescence protease protection assay suggests a cytosolic C-terminus of ARL6IP1-GFP. (A) CD3-RFP resides at the plasma membrane with cytosolic tag, whereas (B) the ER membranes harbours FAM134B-GFP with cytosolic tag. RFP-KDEL is an ER luminal protein. (C) Overview of the FPP assay procedures: Plasma membrane is permeabelised by digitonin, followed by trypsin administration resulting in digestion of cytosolic fluorescent proteins. (D) shows the averaged overall cell intensity normalised to t_0. (E) illustrates the area under curve upon trypsin administration. (F) pictures the calculated decay upon trypsin administration. Dig. = digitonin.

Table 7: Curve statistics of fluorescence intensity dynamics during FPP assay upon trypsin administration (t=140 s). *AUC = area under the curve.*

	RFP-KDEL	ARL6IP1-GFP	FAM134B-GFP	CD3-RFP
AUC ±SEM in % × s	42687 ± 1975	14504 ± 1349	6064 ± 2038	6701 ± 709.4
Decay (τ) ±SEM in s	183.40 ± 21.62	76.35 ± 10.14	49.95 ± 18.01	93.60 ±12.65

5.6 Assessment of *Arl6ip1*-KO mice

5.6.1 The established mouse line is deficient of Arl6ip1

Arl6ip1-deficient mice were established using homologous recombined embryonic stem cells, following breeding with Cre and Flp recombinase positive strains and backcrossing with C57BL/6J mice (see 4.2.6). Absence of Arl6ip1 was verified in brain and spinal cord tissue by probing an immunoblot with the Arl6ip1-specific antibody (recognising the cytosolic loop) verifying the effectiveness of the knock-out strategy (Figure 28).

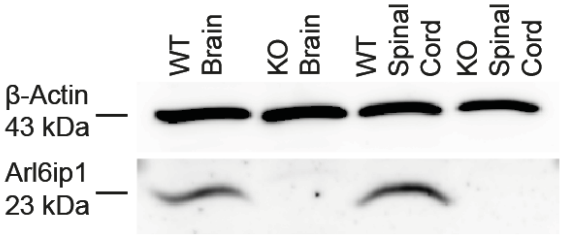

Figure 28: Verification of the Arl6ip1-KO in mouse tissue. *Immunoblot proofs the absence of Arl6ip1 protein bands in brain and spinal cord tissue.*

5.6.2 Homozygous knock-out of Arl6ip1 *results in a prominent neurological phenotype resembling features of the human disease*

After establishing the *Arl6ip1* mouse strain and breeding of the first homozygous KO mice an animal caretaker noticed an obvious phenotype in these mice. When lifting mice at its tail base KO mice tended to clasp their hind limbs with subsequent spastic movement with an onset around 6-8 weeks of age. Additionally, homozygous KO animals showed a malpositioning of hind limbs when moving, shrunken flanks, disturbed fur and kyphosis. All of these features progressed during aging. Overall, the *Arl6ip1*-KO line appears to be a suitable model for further investigation as it mimics features of the HSP phenotype observed in patients. The total body weight in *Arl6ip1*-KO mice is significantly reduced at the age of 2 and 22 months while 8-month-old animals show a trend to lower body weight as well (Figure 29, Table 8).

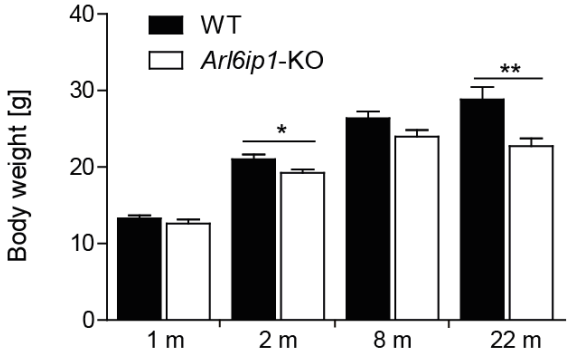

Figure 29: Body weight comparison of cohorts with similar sex distribution. *Arl6ip1-KO animals have a significantly lower weight at an age of 2 and 22 months For N see* ***Table 8****.*

Table 8: Body weight at different time points of cohorts with similar gender ratio. Student's test.

Body Weight [g]	WT	*Arl6ip1*-KO	P-value
1 month	13.33 ± 0.3580 (N=9)	12.62 ± 0.5435 (N=10)	0.3055
2 months	19.24 ± 0.4555 (N=15)	21.02 ± 0.6341 (N=16)	0.0325
8 months	26.40 ± 0.8775 (N=16)	23.99 ± 0.8688 (N=15)	0.0613
22 months	28.86 ± 1.584 (N=9)	22.75 ± 1.010 (N=11)	0.0034

5.6.3 Deficiency of Arl6ip1 *results in a severe motor phenotype*

Due to the hind limb clasping phenotype, basic motor functions were examined. When measuring the peak grip strength of the front paws (Figure 30A), a significant reduction was recognized in KO mice at 2 and 8 months compared to WT mice (Figure 30B, Table 9). A slight age-related effect was recognised in WT mice.

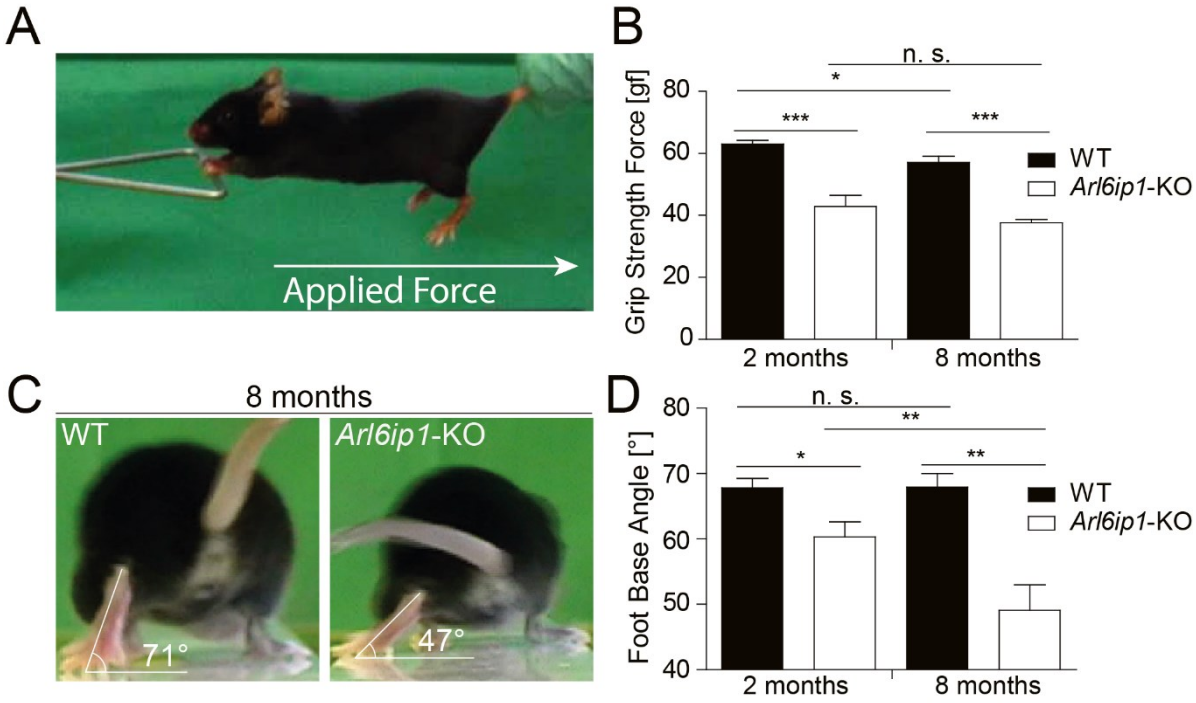

Figure 30: Phenotyping for motor function. *(A) Setup of grip strength measurement. Mice were brought to a handle which they gripped and a pulling force was applied on the tail base by the experimenter. The force was increased gradually and measured at the time-point when the mouse released the handle. (B) Decrease of forepaw peak grip strength in* Arl6ip1*-KO mice. Student's t-test. (C) Representative images of the foot-base angle (FBA) at toe-off position of the hind limb of a WT and a KO mouse traversing a beam. (D) The FBA is decreased in KO mice indicating a progressive gait abnormality. Student's t-test, n=6 WT and n=5 KO mice, n. s.: not significant.*

Table 9: Averaged peak grip strength forces in gram-force (gf). Student's t-test, N=6 WT & 5 KO.

Peak Grip Strength [gf]	WT	*Arl6ip1*-KO	P-value
2 months	62.95 ± 1.212 (N=6)	42.85 ± 3.695 (N=5)	0.0004
8 months	50.59 ± 2.995 (N=6)	35.80 ± 1.880 (N=5)	<0.0001
P-value	0.0302	0.2006	

The foot-base angle (FBA) measurement gives an insight into walking ability and foot abduction (Irintchev *et al.* 2005). It is assessed from rear-view frames while the mouse is walking on a beam allowing the later analysis of the angle between the axis of heel and third toe as well as the beam surface (**Figure 30**C). Again, a significant reduction is found in KO mice at 2 and 8 months. Additionally, there is a decrease of the FBA between 2 and 8 months in KO, proving the progressive characteristics of the HSP-like phenotype (**Figure 30**D, Table 10).

Table 10: Mean foot-base angles and SEM in °. Significance was evaluated by Student's t-test.

Foot-base angle [°]	WT	*Arl6ip1*-KO	P-value
2 months	67.83 ± 1.423 (N=6)	60.33 ± 2.287 (N=5)	0.0179
8 months	67.97 ± 2.073 (N=6)	49.07 ± 3.918 (N=5)	0.0016
P-Value	0.9741	0.0380	

5.6.4 *Nerve conduction measurements suggest a strong effect on the peripheral nervous system*

Wild-type and *Arl6ip1*-deficient mice were subjected to peripheral nerve conduction measurements. For this, electrodes with a known distance were inserted into the tail of anaesthetised mice. An impulse at the stimulating electrode resulted in an electric field which depolarised and hence excited the nerves and the resulting travelled field sum potential (neuronal or muscular)

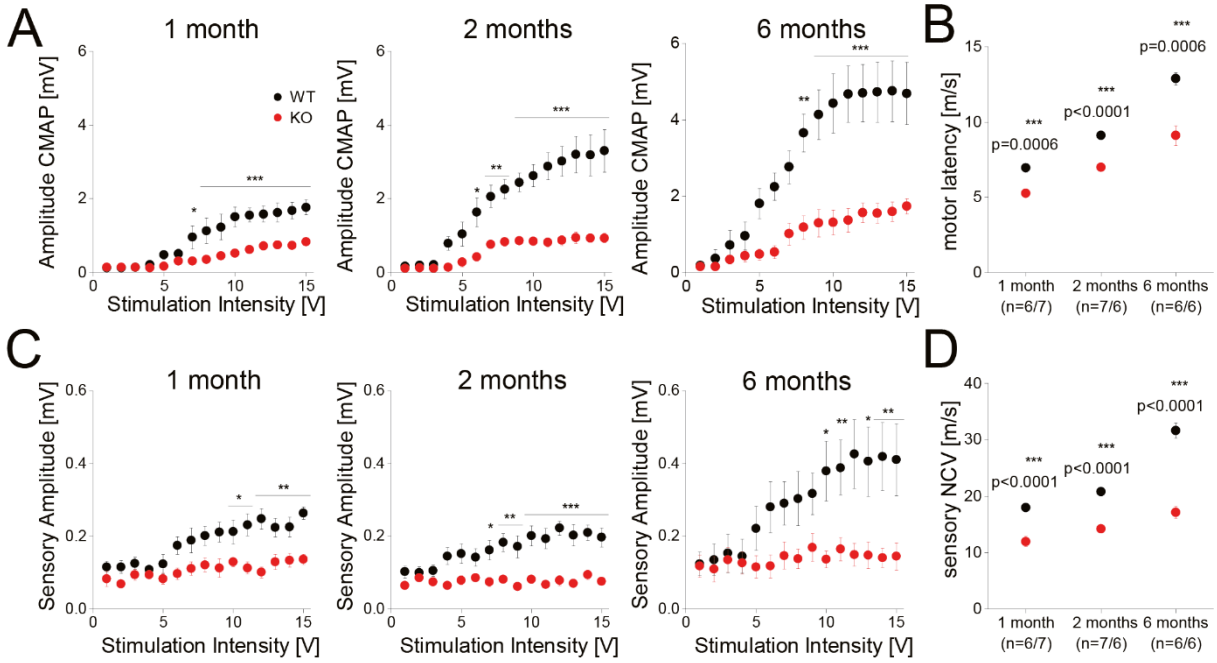

Figure 31: Nerve conductance studies at different ages show a drastic decrease of conduction in KO. (A) Compound muscle action potentials (CMAPs) are decreased in KO. (B) Deduced motor latencies are reduced in KO. (C) Sensory amplitudes as well as (D) nerve conduction velocities (NCV) are impaired in KO at all three ages. Repeated-measures ANOVA with Bonferroni post-test at amplitudes and Student's t-test for NCVs. 1/2/6 months, WT N=6/7/6, KO N=7/6/6.

can be measured at the second electrode. Two parameters were used as readout: The latency and the amplitude at the measuring electrode. With the latency and the known inter-electrode distance the sensory nerve conduction velocity (NCV) and motor latency can be calculated. While the calculated sensory NCV reflects the actual travelling speed within the nerves, the motor NCV contains the travelling speed within the nerve and also the transmission of the chemical synapse of the neuromuscular junction. Hence, the motor NCV is given as readout including neuronal transmission and transduction at the NMJ. On the other hand, the amplitude size gives a crude insight into how many neurons conduct the signal within the nerve. Neurodegeneration can result in reduced amplitudes.

Compound muscle action potential (CMAP) amplitudes differ drastically between WT and *Arl6ip1*-KO mice in all three ages tested, with smaller amplitudes in KO starting at 7-8 V trigger intensity (Figure 31A, Table S1). The same is true for sensory amplitudes, which are almost undetectable in the KO mice (Figure 31C, Table S2). Hence, the signal transmission is highly disturbed in both motor and sensory fibres. Additionally, the deducted sensory nerve conduction velocities and motor latencies are massively changed in all three age groups for both motor and sensory fibres (Figure 31B,D & Table 11).

Table 11: Mean latency-deducted nerve conduction velocities and SEM in m/s. Student's t-test served as significance indicator.

	1 month (N=6/7)			2 months (N=7/6)			6 months (N=6/6)		
	WT	KO	p-Value	WT	KO	p-Value	WT	KO	p-Value
Motor NCV (incl. NMJ)	6.950	5.247	0.0006	9.101	6.998	P<0.0001	12.87	9.100	0.0006
SEM	0.279	0.230		0.162	0.231		0.409	0.650	
Sensory NCV	17.93	12.00	P<0.0001	20.82	14.23	P<0.0001	31.62	17.11	P<0.0001
SEM	0.331	0.8656		0.6680	0.5318		1.339	1.022	

5.7 Neurodegeneration in cortex and cerebellum

5.7.1 Cerebral cortex layer neuron count

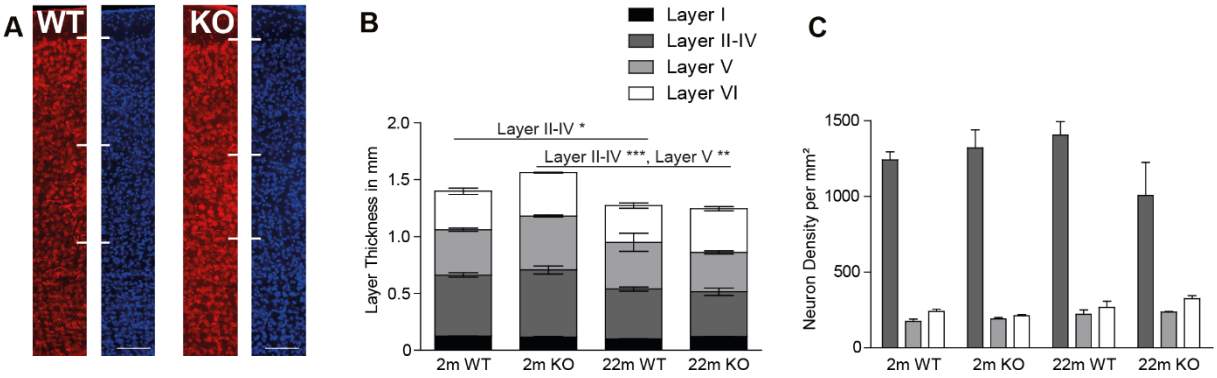

Figure 32: Cortical layer analysis. *(A) Exemplary images of NeuN staining and layer identification. Scale bars 250 µm. (B) Layer thickness of analysed sections. (C) Neuron density per mm² in the specific layers.*

To analyse the neuron density in the motor cortex, sagittal brain sections of both young and old animals were prepared and stained for the pan-neuron marker NeuN. Layerwise quantification of NeuN-positive cells per area revealed no prominent difference in neuron densities (**Figure 32**). Absolute layer thickness was not significantly changed between genotypes of same age. An aging effect is measurable with layer II-V shrinkage within both genotypes in addition to layer V reduction in KO. When assessing the neuron density, no difference was found in total or layerwise analysis.

5.7.2 Cerebral cortex tissue changes can be found in Arl6ip1-ER-Tomato-Emx1 *mice*

Arl6ip1-WT and -KO mice were crossed with a strain carrying the ER-resident fluorescent reporter protein ER-Tomato and *Emx1-cre* mice. Thus, the ER was labelled with Tomato in *Emx1*-positive cells in WT and *Arl6ip1*-KO mice (*Arl6ip1-ER-Tomato-Emx1*, 4.2.6).

This animal model allows the assessment of the effect of *Arl6ip1* deletion on the ER in the respective tissue. Unfortunately, only a very limited number of animals were available. Overall, sagittal brain did not show any obvious differences between WT and KO in the overview (**Figure 33**). However, a closer look at the somatomotor and somatosensory cortex revealed an apparent higher signal intensity of the ER-Tomato signal. When examining cortical neurons at higher magnification, ER-Tomato positive punctae attracted attention in the KO. Analysis of the hippocampus revealed noticeable dot-like signals in the area of Schaffer collaterals in KO mice which were absent in WT mice (**Figure 34**). Additionally, neurons in the hippocampal region CA4 were visible in WT but almost absent in KO leaving behind ER-Tomato positive punctae. For verification further mice need to be analysed.

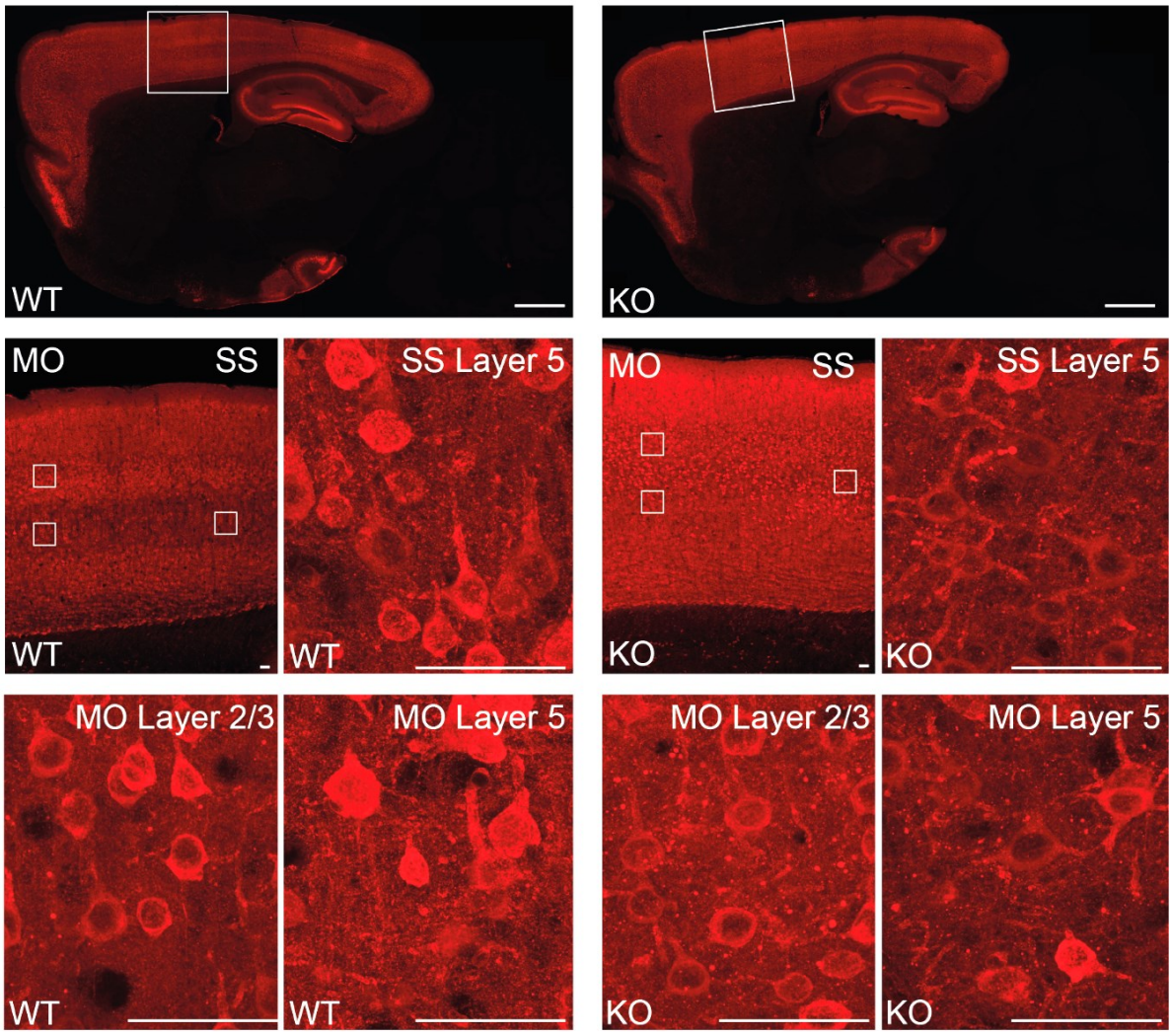

Figure 33: Sagittal brain sections of Arl6ip1-ER-Tomato-Emx1 *of 10-month-old mice. The overview shows a similar expression pattern of ER-Tomato in Emx1-cre positive cells. Close-up views of the motor (MO) or somatosensory (SS) cortex (marked with white frames in overview) reveal an accumulation of punctae in KO. Scale bars, overview image: 200 µm, zoomed images: 50 µm.*

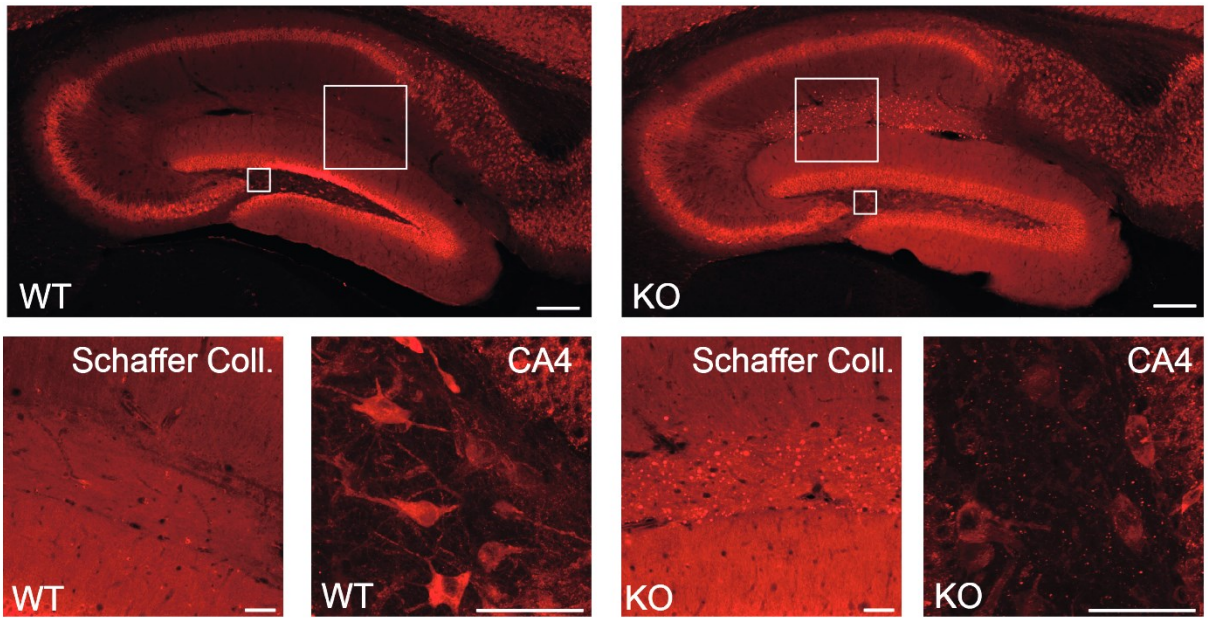

Figure 34: Hippocampus of Arl6ip1-ER-Tomato-Emx1 of 10-month-old mice. A prominent debris-like signal is visible in the region of Schaffer collaterals in KO. Additionally, neurons in the CA4 hippocampus region are not observable in KO leaving behind tomato-positive debris. Scale bars, overview image: 200 µm, zoomed images: 50 µm.

5.7.3 Purkinje neurons are progressively lost in KO mice

Purkinje cells are the largest cells within the cerebellum and are Calbindin-positive (**Figure 35**A). Analysis of the Calbindin staining suggested a reduction of Purkinje cells in KO mice. For this reason, a quantification of those cells was conducted on H&E stained brain sections (**Figure 35**B, by Hector Foronda). Indeed, besides an age-dependent difference, a genotype-dependent decrease was found in 22-month-old KO mice (WT, 2 m: 15.55 ± 0.55 cells/mm, 22 m: 12.95 ± 0.21 cells/mm, KO, 2 m: 15.21 ± 0.31 cells/mm, 22 m: 9.971 ± 0.46 cells/mm, Student's t-test, WT 2 m vs. 22 m p=0.0004, KO 2 m vs 22 m p<0.0001, WT 22 m vs. KO 22 m p<0.0001).

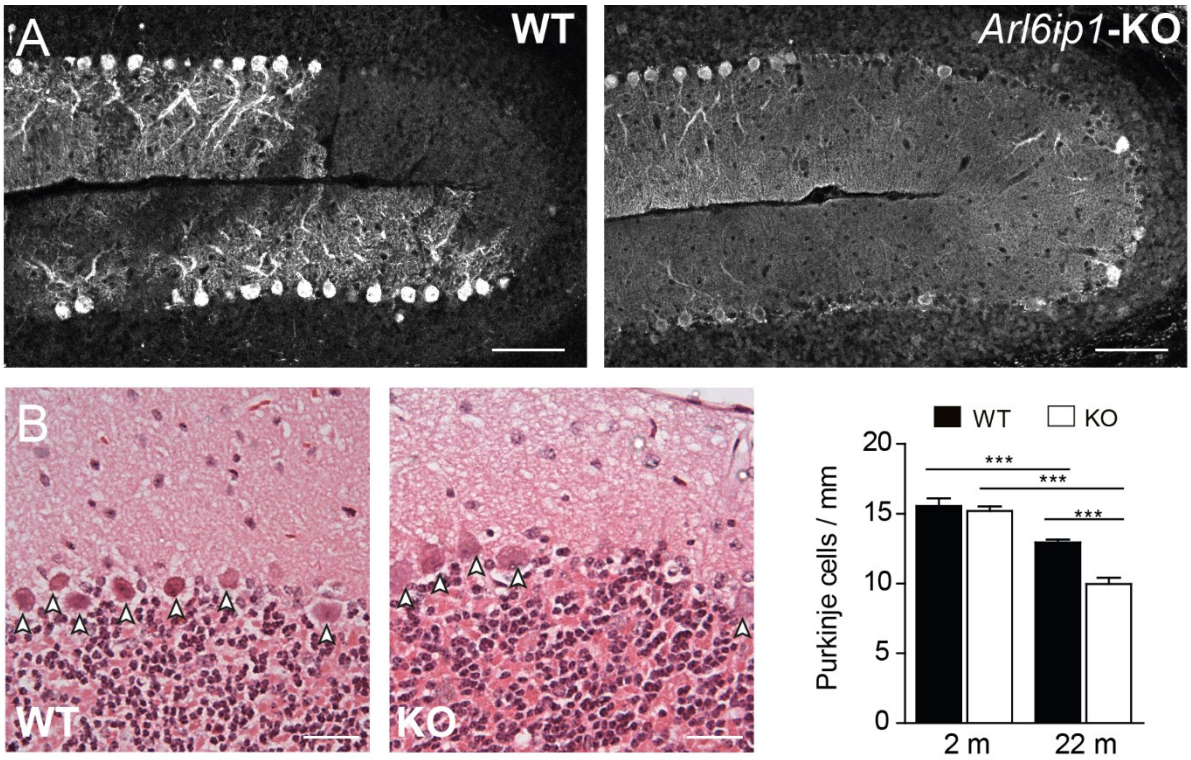

Figure 35: Purkinje neurons in* Arl6ip1*-KO mice. *(A) Cerebellum of 22-month-old animals stained for Calbindin, a marker of Purkinje cells, showing a loss of these cells. Scale bar 100 µm. (B) Verification and quantification on sagittal H&E stained brain slices validate a Purkinje neuron loss. Scale bar: 100 µm. Student's t-test, N=3 mice per age and genotype with 3 slices analysed for each, *** p<0.01.*

5.8 Motor neurons are reduced in spinal cord and cortical fibre tracts are affected

5.8.1 Spinal cord motor neurons degenerate in Arl6ip1*-KO mice*

Transversal thoracic spinal cord sections at the 7-9th thoracic vertebral segments (Th7-9) were Nissl stained. As motor neurons contain a large rough ER, they exhibit a prominent staining.

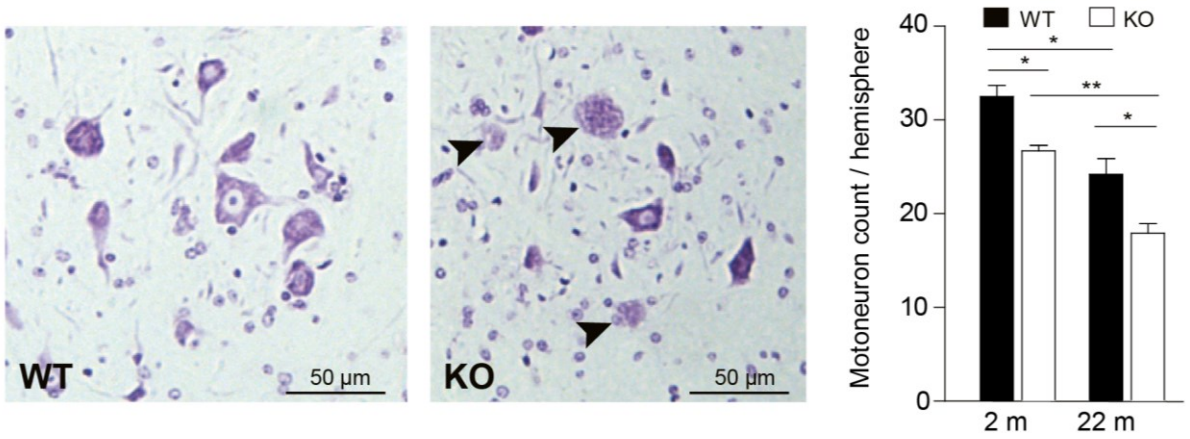

Figure 36: Motor neuron morphology and count in thoracic spinal cord. *Sections (5 µm) at the thoracic level reveal an accumulation of amorphous structures (possibly depicting degenerated motor neurons) in the lateral and medial nuclei in KO. The motor neuron count is reduced in 2 and 22-month-old KO compared to WT mice of same age. Within the same genotypes there are age effects recognisable. Unpaired t-test with Welch's correction, N=3/3.*

When quantifying cells on the ventral side, significant differences can be found in both 2 and 22-month-old animals between WT and KO, with less motor neurons in KO mice (Figure 36). An age-dependent effect is visible for WT and KO mice, as older animals of the same genotype show a reduced motor neuron count. Sometimes Nissl-positive amorphous structures could be detected in KO samples.

5.8.2 Arl6ip1-*KO reporter mice show an uncommon ER pattern in the thoracic spinal cord*

The *Arl6ip1-ER-Tomato-Emx1* mouse model could be used to assess neuronal ER signal in spinal cord sections in WT and KO independent of an antibody staining. Lumbar transversal and thoracic longitudinal sections were prepared and imaged for the expression of ER-Tomato (Figure 37). In analysed transversal sections, an accumulation of dot-like signals could be found in the dorsal column (likely *Fasciculus gracilis*) of *Arl6ip1*-KO mice. To analyse this signal in more detail, longitudinal (coronal) sections were imaged, showing a prominent signal enriched in single dilated axons in the KO whereas in WT mice the ER-Tomato signal was more evenly distributed. These structures may correspond to swollen axons.

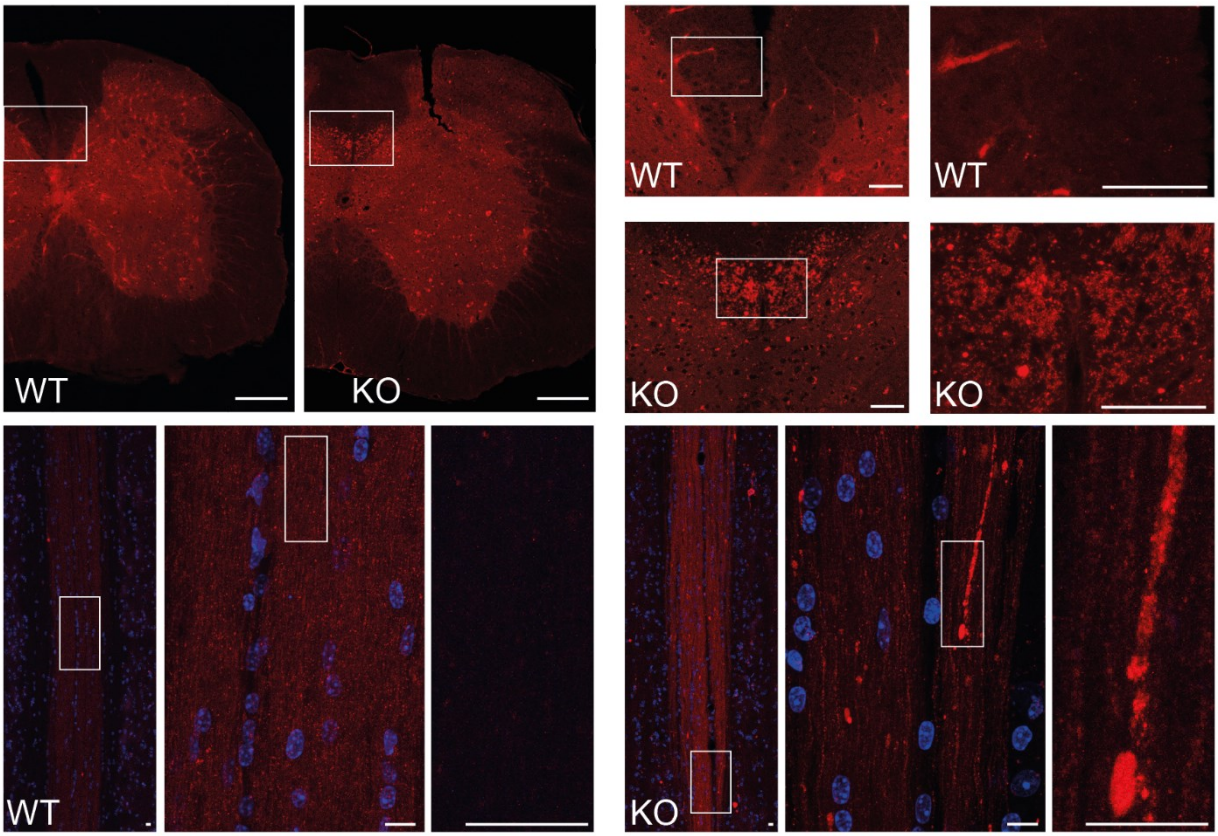

Figure 37: Spinal cord of Arl6ip1-ER-Tomato-Emx1 mice (10 months old). *Cross-sections at a lumbar level reveal accumulation of ER-Tomato signals in the dorsal column fibre tract of KO. Coronal longitudinal sections verify this signal enrichment in KO. Scale bars, overview: 200 µm, transversal zoom: 50 µm, longitudinal sections: 10 µm.*

5.8.3 Axon swelling in the thoracic spinal cord is verified by electron microscopy

The dorsal column of thoracic spinal cord contains afferent, sensory fibres. When assessing the ultrastructure of this region, dilated axons can be seen (Figure 38).

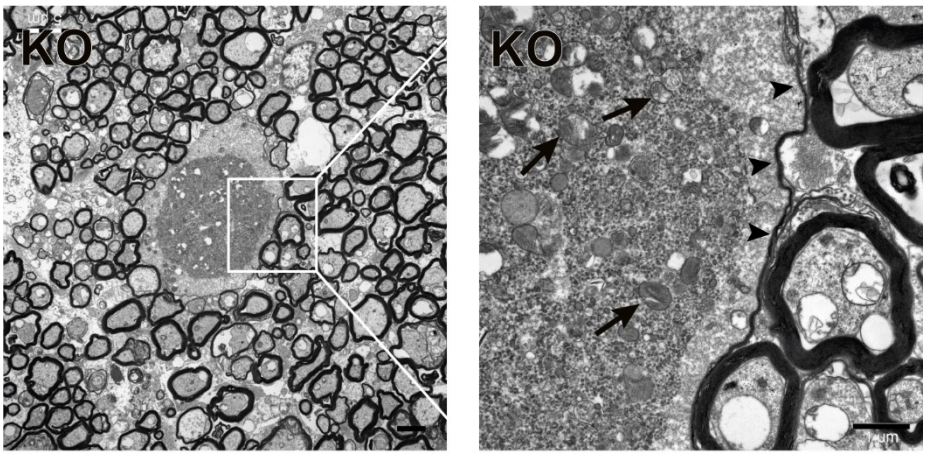

Figure 38: Ultrastructural analysis of a 6-month-old Arl6ip1*-KO shows axon swelling in the dorsal column in horizontal thoracic spinal cord sections.* *The swollen axon is still enwrapped by myelin (arrowheads) and contains granular osmiophilic material and degenerating organelles (arrows), including many abnormal mitochondria. Scale bar: 1 µm.*

This swollen axon is enwrapped by myelin sheets (arrowheads) and contains an accumulation of defective organelles such as mitochondria (arrows) and granular electron dense material.

5.9 Skeletal muscles in *Arl6ip1*-KO

5.9.1 Skeletal muscle mass is reduced in Arl6ip1-*KO*

Gastrocnemius muscles of animals at the age of 6 months were isolated and weighed. KO muscle mass was drastically reduced to 71.4 ± 6.8 mg in comparison to 139.8 ± 12.2 mg in WT (**Figure 39**).

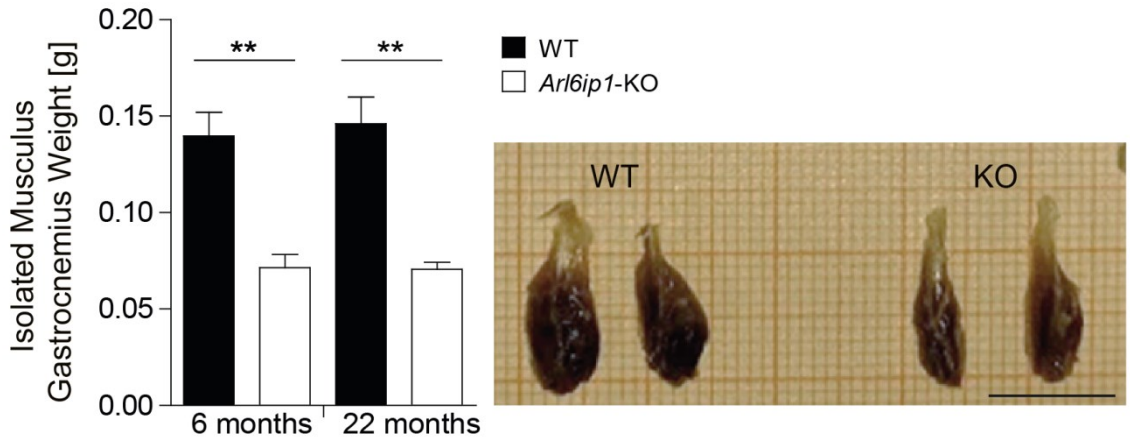

Figure 39: Weight and size of M. gastrocnemius are reduced. *Comparison shows muscle mass reduction. Student's t-test, N=3/3. Exemplary image of muscle atrophy of M. gastrocnemius isolated of animals at 6 months-of-age. Scale bar: 1 cm.*

5.9.2 Skeletal muscle atrophy is caused by denervation

To further investigate the cause of muscle waste, histological analysis was conducted by light and electron microscopy. In semi-thin sections, atrophic muscle fibres are visible in KO mice whereas WT mice show no abnormalities (**Figure 40**A). Ultrastructural analysis of the *M. gastrocnemius* by electron microscopy confirms muscle fibre degeneration (**Figure 40**B). The fact that whole muscle bundles are degenerated, suggests a neurogenic origin. Furthermore, a degenerating neuromuscular junction (NMJ) is visible in KO (**Figure 40**C). On the level of nerve fibres, osmiophilic material can be found in intramuscular neuron fibres in the KO (**Figure 40**D).

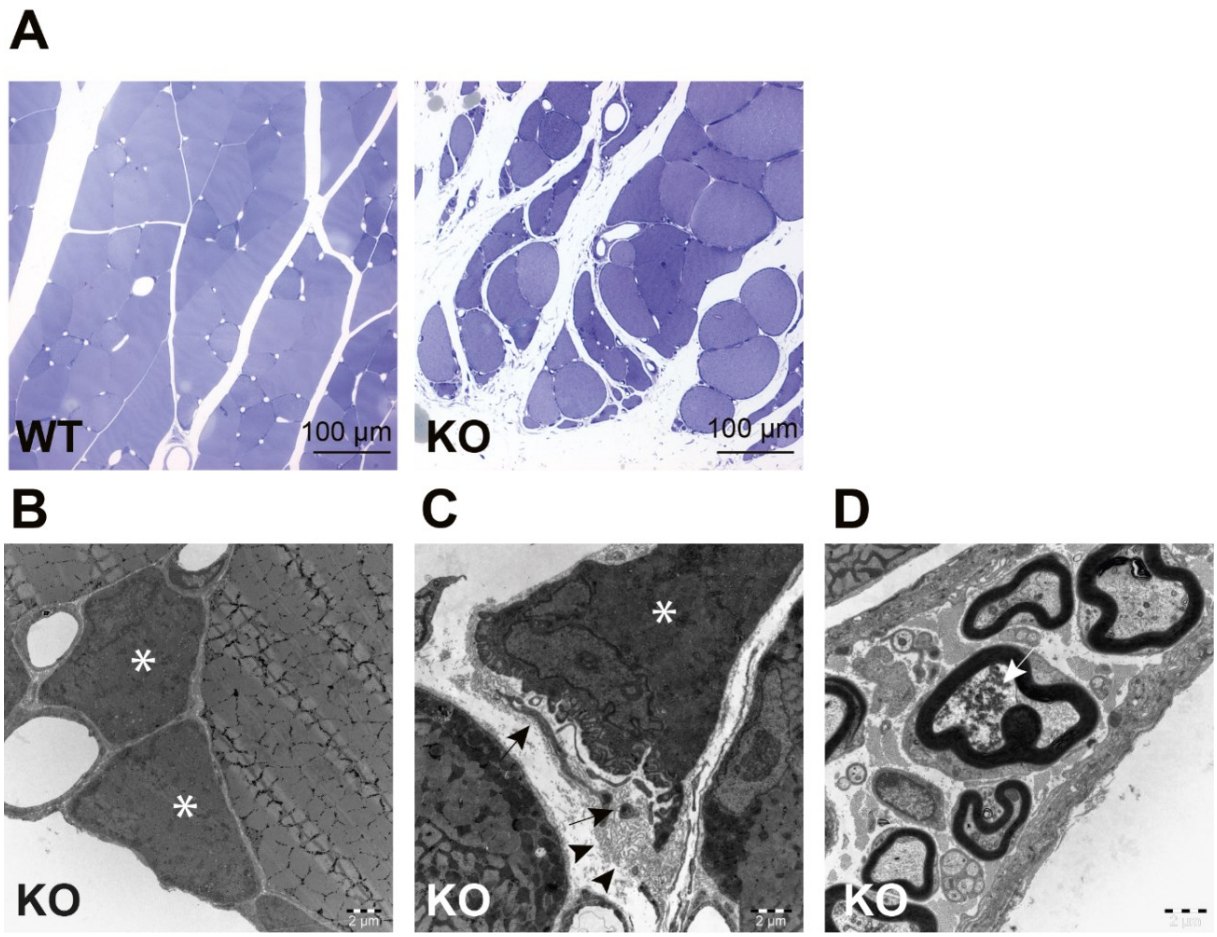

Figure 40: (Ultra)histological studies of the M. gastrocnemius *show neurogenic muscle degeneration in Arl6ip1-KO mice. (A) Toluidine blue stained semi-thin sections reveal grouped atrophic skeletal muscle bundles in 6-month-old KO animals. (B) Small diameter atrophic muscle fibers (asterisks) as a result of denervation next to a healthy fiber with regular architecture. (C) Atrophic fiber (asterisk) with sarcolemmal invaginations and basal lamina loops (arrows) together with several Schwann cell processes (arrowheads), typical for a denervated neuromuscular junction. (D) Accumulation of densely packed osmiophilic tubulofilamentous material (arrow) in a myelinated intramuscular nerve fiber. Scale bar in A: 100 µm, in B-D: 2 µm.*

5.10 Dorsal root ganglion neurons show morphological alterations

5.10.1 Immunohistochemistry on DRG sections shows increased Climp63 signal intensities in Arl6ip1-*KO mice*

Dorsal root ganglia are embedded in the spinal column vertebrae on either side of the spinal cord and contain the somata of sensory neurons. As a sensory loss is described in patients, alterations in these neurons are likely to occur in mice as well. To assess the ER morphology in these DRG neuron cell bodies, cryosections of isolated murine DRG tissue were immunostained for the ER marker Climp63. When having a closer look to the DRG tissue (Figure 41), an even distribution of Climp63 can be found in WT controls whereas KO tissue shows heterogeneous accumulations of the marker. There is more signal recognised in the KO DRG cell bodies compared to their WT counterparts.

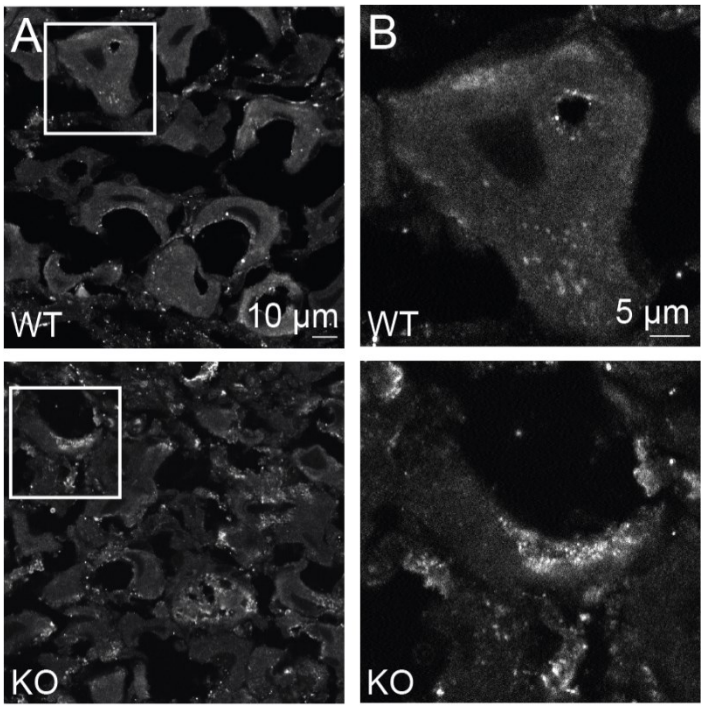

Figure 41: Immunostaining for the ER marker Climp63 on cryosections of DRG of WT and KO. *(A) Overviews reveal a higher perinuclear accumulation of Climp63 signals in KO samples whereas WT presents a rather homogenous distribution of signals. (B) Zoom of previous image as indicated by white frame.*

5.10.2 Ultrastructural analysis of cultured dorsal root ganglion neurons shows differences in ER and mitochondria

To further elucidate the ER morphology in DRG neurons, cultured neurons were investigated by electron microscopy. The perinuclear region was imaged and analysed (Figure 42). The ER area was quantified and compared between WT and KO sections. Importantly, a reduced ER area (normalised to cell size) was identified in KO mice (WT: 12.09% ± 1.94%, KO: 3.62% ± 0.62%, Student's t-test, p=0.0003, n=15). Additionally, the lumen of the perinuclear ER structures appeared to be narrower in the KO in comparison to WT (WT, wide: 60.41% ± 5.05%,

narrow: 39.59% ± 5.05%, KO, wide: 18.50% ± 3.61%, narrow: 81.50% ± 3.61%, Student's t-test, p <0.0001, n=30). In several KO cells, mitochondria look expanded with a more elongated shape. Furthermore, unidentified vacuoles possibly related to degradative compartments tend to be more present in KO (quantification pending).

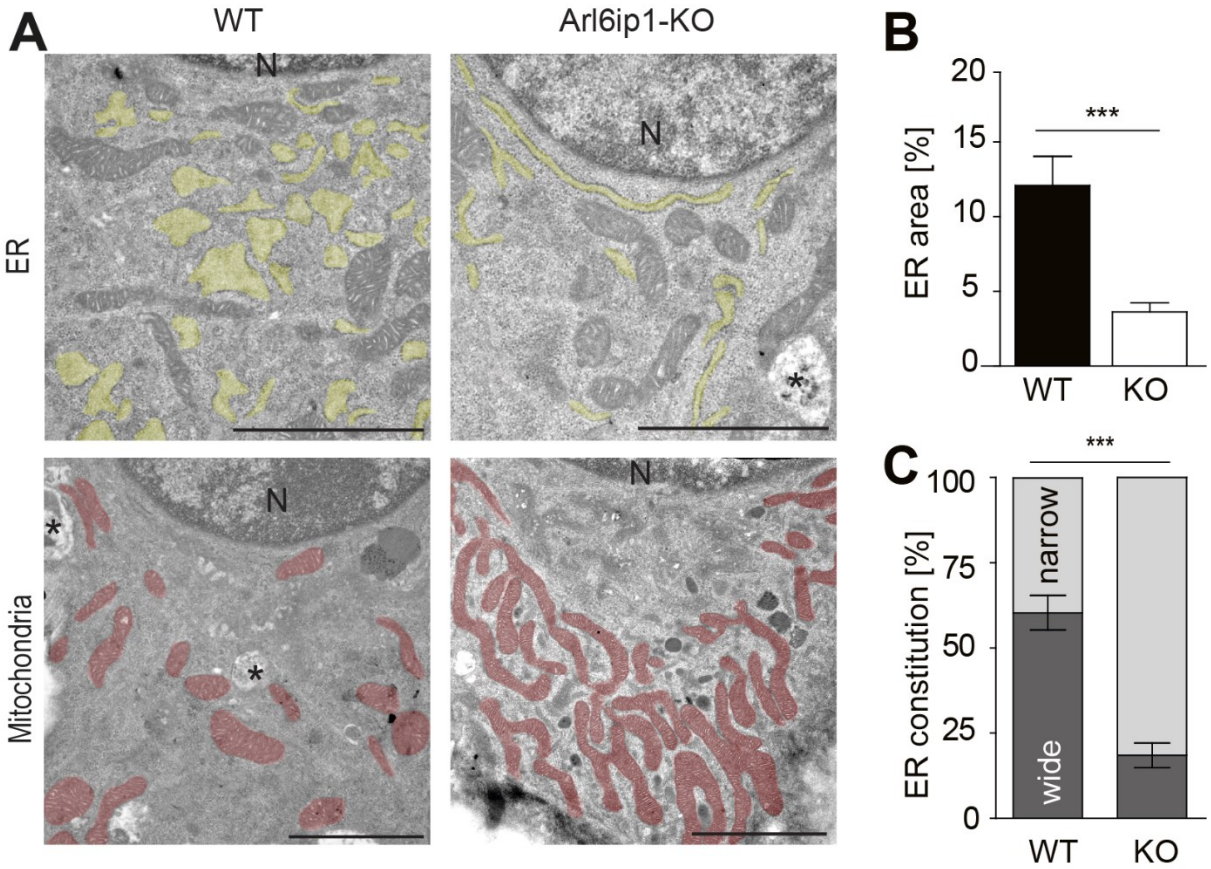

Figure 42: Electron microscopic analysis of cultured DRG neurons. *(A) Analysis of ER structure in cultured dorsal root ganglia (DRG) neurons. Representative electron micrographs of a cultured primary DRG neuron of WT and* Arl6ip1-*KO with the ER tinted in yellow and mitochondria tinted in red. asterisks: vacuoles, scale bar: 1 µm. (B) Quantification of the relative ER area of WT and* Arl6ip1-*KO DRG neurons normalised on cell area. Student's t-test, n=15 cells per condition. (C) Quantification ER constitution in DRG neurons with wide ER (dark grey)* versus *narrow ER (light grey). Cut-off 80 nm, Student's t-test, n=30 cells per condition.*

6 Discussion

Mutations in *ARL6IP1* are associated with a neurological phenotype that overlaps with symptoms of FAM134B-loss and both proteins were found to interact. The underlying cellular and molecular pathomechanisms, however, were still largely unknown. In a previous study of the lab, a detailed analysis of Fam134B identified its role in selectively target ER membranes into autophagosomes for degradation, thereby regulating ER turnover (Khaminets *et al.* 2015). Therefore, this thesis aimed to elucidate the role of ARL6IP1 for cellular maintenance.

To study the consequences of *Arl6ip1*-deficiency, a knock-out mouse model was established (chapter 4.2.6.1). The *Arl6ip1*-deficiency of KO animals could have been proofed by immunoblot validating the mouse model (chapter 5.6.1).

6.1.1 Phenotypic characterisation of the Arl6ip1*-KO mouse model*

Homozygous KO mice display a gait disorder resembling HSP: When elevated, KO mice showed hind limb clasping starting around 6-8 weeks of age. Interestingly, this is different for *Fam134B*-KO mice which show no obvious motor phenotype. The infantile onset of the observed motor symptoms is in accordance with the clinical picture (Nizon *et al.* 2018, Novarino *et al.* 2014, Wakil *et al.* 2019). This phenotype was hence further analysed and motor functions assessed in a quantitative manner (chapter 5.6.3). The grip strength assay exhibited a drastic loss of force at the age of 2 and 8 months in KO animals compared to WT mice. The measurement of the foot-base angle (FBA) served to quantify motor impairment over time (Irintchev *et al.* 2005). In agreement with other mouse models of HSP (Beetz *et al.* 2013, Khundadze *et al.* 2013, Khundadze *et al.* 2019, Varga *et al.* 2015), mice showed a progressive flattening of the foot-base angle, which is consistent with recently published clinical data showing strong motor impairments in human patients suffering from SPG61 (chapter 3.7.4). The progressive manner of the disease phenotype in human (Fowler and O'Sullivan 2016, Wakil *et al.* 2019) is reflected by the FBA decline from 2 to 8-months-old animals in the KO cohort whereas the FBA is stable over time in WT mice.

Based on the mouse behavioural tests, the question remained whether the observed weakness is of muscle or neuronal origin. To address a potential neuronal phenotype, tail nerves were assessed, which comprise both motor and sensory fibres (chapter 5.6.4). To get an idea of peripheral nerve function, these nerves were stimulated electrically with a stepwise increasing

intensity and the amplitude of the distal response was measured in anaesthetised mice – either in proximal direction for sensory nerves or distal direction for motor nerves. Compound muscle action potential amplitudes, representing motor nerves and synapse, were strongly decreased in KO mice. This is in accordance with motor impairments as well as the neuropathy and neurogenic loss of motor response described in a case study of patients deficient of *ARL6IP1* (Wakil *et al.* 2019). Measurement of sensory amplitudes also showed a reduced signal intensity in *Arl6ip1*-KO mice, which may reflect a loss of sensory fibres. This validates published clinical data that suggest a motor and sensory neuropathy in patients with *ARL6IP1* mutations (Chukhrova *et al.* 2019, Nizon *et al.* 2018). As the distance of the stimulating electrode and the recording electrode and the time the signal needs to travel are known, we were able to determine the mean nerve conduction velocity (NCV). Reduced NCVs in KO mice for both sensory and motor nerves may suggest a defect of axon myelination. In short, not just less intense signal (lower amplitude) is travelling through the nerves of *Arl6ip1*-KO mice in either direction, it is also slower. Hence, *Arl6ip1*-KO mice develop a progressive neuropathy which affects both motor and sensory neuron function.

6.1.2 Histological analysis of Arl6ip1-*KO mice*

Based on the results from the phenotypic characterisation, it was aimed to analyse different neuronal tissues of the central or the peripheral nervous system which might be affected.

To clarify whether upper motor neurons are affected, the neurons of the motor cortex were counted in both WT and KO mice (chapter 5.7.1). Although minor changes were observed independent of the genotype, no major difference in the thickness of the different layers was observed in KO mice. Likewise, the neuron densities in the specific layers remained unchanged. Hence, from the underlying data it cannot be concluded that the cortical motor neuron numbers change over time.

In pilot studies using the first animals available of the *ER-Tomato* reporter line, the morphology of the hippocampus appeared different between WT and *Arl6ip1*-KO mice (N=1 each). First, the area of the Schaffer collaterals contains many Tomato-positive dot-like structures in *Arl6ip1*-KO mice. Schaffer collaterals are processes of pyramidal neurons of the region CA3 projecting to the CA1 areas. The dot-like structures might result from either ER abnormalities within living cells or cells which underwent cell death and became debris. Second, when assessing the CA4,

a specific region of the hippocampus, a loss of neurons can be observed in *Arl6ip1*-KO. The hippocampus generally fulfils the function of transferring sensory sensations into long-term memory besides learning and regulation of emotion (Bartsch 2015). These functions were not assessed in the mouse model but clinical case studies mentioned mental retardation (Chukhrova *et al.* 2019).

The somatomotor and somatosensory cortex are crucial for either generating and sending information for voluntary movements or processing sensation from the body's periphery. As the clinical features in human patients and the *Arl6ip1*-KO mouse phenotype indicate an impaired function of both cortices, the *Arl6ip1-ER-Tomato-Emx1* mouse model was used to further assess these brain regions (chapter 5.7.2). Again, dot-like ER-Tomato-positive structures were found next to neurons, possibly indicating degenerating axons or intracellular ER.

Purkinje neurons play a crucial role within the cerebellum as key regulators for the fine-tuning of motor functions (Hirano 2018). Purkinje cells inhibit deep cerebellar nuclei via GABA release (Hirano and Kawaguchi 2012). Purkinje neuron loss may contribute to the observed uncertainty while movement in *Arl6ip1*-KO mice. Hence, these cells were analysed (chapter 5.7.3). The Purkinje neuron quantification on HE stained brain slices revealed a reduction of Purkinje cell cells in 22-month-old *Arl6ip1*-KO mice. Interestingly, no difference could be observed at the age of 2 months. Purkinje neuron loss is a recurrent feature in HSP (Khundadze *et al.* 2013). Potentially, this neuron loss is caused by the accumulation of ER aggregates. Defects in autophagy have been found earlier when investigating other spastic paraplegia genes (Khundadze *et al.* 2013, Varga *et al.* 2015).

The dorsal column is a fibre tract of the spinal cord, which consists in rodents of both sensory fibres which project via the thalamus to the somatosensory cortex and descending motor fibres. When assessing this region in mice deficient for *Arl6ip1* but positive for the ER-Tomato reporter, some fibres of the dorsal column tract of KO showed (chapter 5.8.2).

Electron microscopy was used to assess the ultrastructure of the fibre tract which could confirm the findings in ER-Tomato mice: Not only axonal swellings were found, but also accumulated organelles e.g., mitochondria. Axon swelling was previously observed in other HSP mouse models (Edgar *et al.* 2004).

HSP is characterised by progressive degeneration of either upper motor neurons or both upper and lower motor neurons (Parodi *et al.* 2017). To investigate if lower motor neurons are affected, motoneuron somata were quantified in thoracic spinal cord sections (chapter 5.8.1). In fact, the motor neuron count was significantly reduced in KO in comparison to WT mice. These results are in accordance with the literature, that classifies the HSP resulting from *Arl6ip1*-deficiency as disease affecting the upper and lower motor neurons (Parodi *et al.* 2017).

To answer whether only long-projecting neurons are affected upon Arl6ip1-deficiency and to further investigate morphology changes observed in the Arl6ip1-ER-Tomato-Emx1 mouse line, phenotyping of memory function by behavioural experiments such as Morris water maze or fear conditioning or electrophysiological studies like long-term potentiation assessments are applicable. Another reporter mouse line expressing ER-Tomato in parvalbuminergic neurons of mice WT or KO for Arl6ip1 was established very recently. This tool could help to further address ER changes in Purkinje neurons to get more detailed insights in loss of these cells. Additionally, this mouse line could be used to study the ER in unstained DRGs, as part of the DRG neurons are parvalbuminergic, or even investigate the ER morphology and dynamics in real-time in unfixed cultured DRG neurons.

6.1.3 Muscle loss

As mentioned earlier, *Arl6ip1*-KO mice are lighter and exhibit a decreased foot-base angle which indicates impaired walking abilities. Upon dissection, a muscular atrophy was obvious in KO animals. Hence, minor studies on muscles were conducted.

Each lower motor neuron innervates a set of muscles fibres via neuromuscular junctions (NMJs). When muscle-innervating neurons degrade, this leads to a denervation of muscle fibres which subsequently degenerate (Batt and Bain 2013).

A drastic loss of body weight as well as muscle mass and size could be observed in *Arl6ip1*-KO mice (chapter 5.6.2 and 5.9.1). The muscle mass of the *Musculus gastrocnemius* was reduced by almost 50%. Additionally, toluidine-stained sections of this muscle show grouped atrophic muscle bundles adjacent to normal or enlarged muscle fibre bundles (chapter 5.9.2). Atrophic fibres could be also detected by electron microscopic ultrastructural analysis. Furthermore, de-

generating NMJs could be seen as well as accumulation of osmiophillic material in intramuscular nerve fibres. All these findings suggest that muscle fibres degenerate due to loss of innervating nerve fibres. In fact, HSP has been characterised as an atrophying muscle disease (Parodi *et al.* 2017).

6.2 Molecular and cellular studies on ARL6IP1

6.2.1 ARL6IP1 interacts with FAM134 proteins

It was found previously that ARL6IP1 is a positive hit of a large-scale yeast two-hybrid screen with FAM134B as bait (unpublished results of the group). To verify an interaction, ARL6IP1-myc was co-expressed with FAM134 proteins, FAM134B variants (see Figure 22) or Atlastin 3, another protein harbouring Reticulon homology domains, which served as negative control. Subsequent co-immunoprecipitation (CoIP) studies (chapter 5.3.3) confirmed an interaction with ARL6IP1 for all constructs, except the negative control and the FAM134B construct missing the N-terminal amino acids 1-161. This suggests that ARL6IP1 interacts with the FAM134 proteins. Further, it is indicated that the interaction with FAM134B requires the N-terminal part of FAM134B.

6.2.2 Interaction of FAM134B with ARL6IP1 variants

When performing CoIP experiments of FAM134B with various ARL6IP1 variants (see Figure 20) it appears that all ARL6IP1 variants regardless of truncations or mutations are still able to interact with FAM134B-myc (chapter 5.3.5). The negative controls like ATL3-GFP and GFP alone did not interact.

There are at least two possible explanations for the finding that all ARL6IP1 variants interact with FAM134B. Either an interaction is only depending on the FAM134B N-terminus while no specific site of ARL6IP1 is required or there is more than one binding site at the ARL6IP1 protein.

6.2.3 ARL6IP1 colocalises with FAM134B

Transient overexpression of ARL6IP1-myc and FAM134B-HA results in a similar localisation of both proteins. However, the distribution seems to be somewhat shifted with more ARL6IP1

being present in peripheral ER, whereas FAM134B is more prominent in perinuclear regions. This is consistent with previous reports (Dong *et al.* 2018, Khaminets *et al.* 2015). The pattern of ARL6IP1-L31P-myc seems to be similar, but on close-up the colocalisation with FAM134B is not that strong anymore with structures only positive for FAM134B-HA. Images of ARL6IP1-K193F*fs transfected cells reveal a more frequent presence of condensed structures within the cells. These are positive for both the ARL6IP1 variant and FAM134B. Aside from this morphological change, the colocalisation does not appear to be impaired.

The colocalisation of overexpressed ARL6IP1 and FAM134B as well as of endogenous levels of both proteins was validated by a Proximity Ligation Assay as conducted by Patricia Franzka (data not shown, manuscript in preparation).

In the discussed experiment, a system with transient overexpression of constructs was used due to the lack of reliable antibodies. Neither for FAM134B nor for ARL6IP1 highly specific commercial antibodies were available. Two antibodies raised against the hydrophilic loop or C-terminus of ARL6IP1 in rabbits did not show specific results either.

The drawback of overexpression systems is the lack of control of how much construct a single cell has taken up, ranging from marginal abundance to massive expression levels. In addition, the overexpression of membrane proteins to study the endoplasmic reticulum, the cellular organelle where membrane protein synthesis takes place, may affect the object of the study. In every set of *Arl6ip1*-transfected cells, drastic changes of ER morphology were observed, regardless of whether WT or variants were transfected. These changes included perinuclear accumulations, which were highly positive for ER markers and the FAM134B and ARL6IP1 protein. These cells were excluded from analyses.

Another challenge is the cotransfection of cells. The transfection rate is considerably lower in MEFs compared to e.g., HEK293T cells. For this reason, only single or double transfections did result in reasonable quantity of positive cells.

Fluorescent proteins are a convenient tool in molecular biology. Not only the transfection efficiency of fluorescent proteins can be assessed at any time, it also allows live cell imaging. Furthermore, the fluorescent tag can still be used after fixation and allows (but does not necessarily need) antibody staining against the tag. On the other side, these advantages come with a few drawbacks: Fluorescent proteins are relatively large (eGFP: 27 kDa), which can be particularly problematic when analysing small proteins such as ARL6IP1 (23 kDa). This could lead to

steric hindrance during ARL6IP1 protein folding. To counteract this issue, a flexible six amino acid long linker with no ordered secondary structure was inserted. Another limitation of the use of GFP is the fact that GFP itself has a tendency to dimerise (Costantini *et al.* 2012). This effect increases with higher GFP concentrations. If this fluorescent protein is fused to a transmembrane protein, the tendency to dimerise may even increase. Furthermore, the membrane protein leads to an orientation of the GFP allowing it to rotate only in one degree of freedom resulting in higher possibility of dimerisation (Costantini *et al.* 2012). The dimerisation may even lead to the reorganisation of the membrane structure resulting in whorls of the membrane stabilised by the dimerising fluorescent proteins fused to membrane proteins. Costantini *et al*. suggested the term organised smooth ER (OSER) for these structures. For this reason, myc-tagged variants were used whenever possible. Nevertheless, aggregates were seen in ARL6IP1-myc transfected cells as well, although to a lesser extent. These aggregates were also observed by Yamamoto *et al.* (2014) and Dong *et al.* (2018). The GFP-independent accumulation might be caused by the possibility of ARL6IP1 to oligomerise in combination with its shaping ability. The interplay of shaping ER membranes and a higher probability of ARL6IP1 to be present at curved membranes (due to its energetic stability) might lead to a self-increasing accumulation upon a certain overexpression level.

Due to all these limitations of protein overexpression studies, an approach of endogenous tagging by CRISPR/Cas9 was planned and performed. The heterozygous insertion of a N-terminal HA- and tetracysteine (FlAsH) tag was successful at the DNA level. Unfortunately, a tagged protein could neither be detected by HA- nor by FlAsH-tag and, thus, was not followed up any further.

6.2.4 The putative LIR motifs of ARL6IP1 are not active

In order to get an idea of ARL6IP1 protein function, its functional domains were investigated.

FAM134B contains an active LC3-interacting region (LIR) motif (Khaminets *et al.* 2015). Because of certain similarities like a similar subcellular localisation, topology and shared clinical phenotypes of patients with ARL6IP1 loss-of-function mutations, the need to investigate an ER-phagy function of ARL6IP1 and presence of a LIR motif in this protein was given. As these motifs do not have a single consensus sequence, the ARL6IP1 protein sequence was screened *in silico* by the online tool iLIR, resulting in the prediction of a small number of putative LIR motifs (chapter

5.2.1). To investigate whether those are active *in vitro*, a CoIP with transiently expressed ARL6IP1-myc was performed at physiological or chloroquine-induced LC3 levels (chapter 5.2.2).

Chloroquine is a lysosomotropic agent, which means it gets trapped within the strongly acidic lysosome due to protonation. It was thought that it impairs the complete acidification of lysosomes and thereby affects the proton-depending hydrolases (Pasquier 2016). Nevertheless, a recent study suggested another mechanism with chloroquine preventing the fusion of autophagosomes with lysosomes (Mauthe *et al.* 2018). Regardless of its mode of action, chloroquine is known to result in the accumulation of autophagosomes, which at this step are still decorated with LC3-II (Schaaf *et al.* 2016). Hence, chloroquine increases the levels of LC3-II.

In samples (untreated and chloroquine-treated) with overexpressed ARL6IP1-myc no LC3 was detected upon CoIP whereas the positive control FAM134B-myc co-immunoprecipitated with LC3. These results suggest that ARL6IP1 is not interacting with LC3 itself and that its putative LIR motifs are inactive.

Apparently, ARL6IP1 does not have the ability to directly recruit LC3-decorated phagophore membranes. Potentially, proteins like FAM134B or others that were not overexpressed or enriched in these samples may interact with both ARL6IP1 and LC3 could possibly mediate an indirect ARL6IP1-dependent ER-phagy. Furthermore, a special trigger (e.g., UPR signals) might be needed to allow direct interaction of LC3 and ARL6IP1.

6.2.5 ARL6IP1 oligomerisation depends on its N-terminal half

ARL6IP1 does oligomerise (Yamamoto *et al.* 2014). To elucidate the necessary sites of ARL6IP1-*trans*-interaction, CoIP experiments with ARL6IP1-myc and GFP-tagged ARL6IP1 variants were performed (chapter 5.3 & Figure 20). Interestingly, only interactions of ARL6IP1-myc with ARL6IP1-GFP, ARL6IP1-Ret2-GFP, ARL6IP1-K193F*fs-GFP and ARL6IP1-ΔKKNE-GFP were found. In contrast, an interaction of ARL6IP1-myc with ARL6IP1-Ret1-GFP was not observed. This finding strongly suggests that the oligomerisation requires the N-terminal half of the protein.

Protein oligomerisation is important for shaping ER tubules as reported for Reticulon 1 and 4 (Shibata *et al.* 2008, Zurek *et al.* 2011). ARL6IP1 is able to shape membranes (unpublished work of Nicole Koch and Yamamoto *et al.* (2014)). The shaping ability increases to a large extent when

ARL6IP1 is enriched locally. Therefore, it appears likely that oligomerisation also occurs at endogenous levels at certain ER sites.

As suggested by the CoIP results, the *trans*-interaction ARL6IP1 requires the N-terminal half of the protein, which consists of the cytosolic N-terminus, the first hydrophobic hairpin and the first half of the cytosolic loop. Possibly, the ARL6IP1/ARL6IP1 interaction does not only take place as a parallel or planar oligomerisation resulting in a tubular shape (see Figure 7B) but additionally in an orthogonal assembly with shaping the membrane in two dimensions (resulting in a tubule tip). This would explain the accumulation at peripheral ER tips as reported by Dong *et al.* (2018).

6.2.6 Effects of Arl6ip1-deficiency on ER-phagy

Previous studies on FAM134B revealed its function as an ER-phagy receptor by its direct interaction with LC3-II (Khaminets *et al.* 2015). Due to overlapping clinical symptoms and protein interaction of ARL6IP1 and FAM134B, a similar pathomechanism upon *ARL6IP1*-loss was considered. This option appears unlikely as a no direct interaction between ARL6IP1 and LC3 was observed. The regulation and procedure of ER-phagy is a complex cellular process, with a potential contribution of ARL6IP1 under physiological conditions. To verify this *in vitro*, cells that could be transiently transfected with tagged ARL6IP1 and their lysates used for pulldown experiments and subsequent analysis of proteins interacting with ARL6IP1 by Mass Spectrometry or Western Blotting. The identification of proteins involved in autophagosome maturation and ER-phagy would suggest a role of ARL6IP1 in ER-phagy. To understand an effect on ER-phagy regulation, levels of identified interaction partners could be compared between WT, *Arl6ip1*-KO and transiently overexpressed cells under normal and also serum-starved conditions, to include investigations in ER-phagy induced states.

To overcome ER stress in cells, a complex machinery called the Unfolded Protein Response (UPR) is activated resulting in upregulation of chaperones, reduction of general protein synthesis but also increased ER-phagy. To investigate whether ARL6IP1 plays a role for these pathways, relevant proteins within the UPR cascade could be monitored.

To investigate an effect of ARL6IP1 on the recently described mechanism of ER exit site (ERES) related micro-autophagy described by Omari *et al.* (2018), the herein published procollagen

assays could be applied. Procollagen, the precursor of extracellular matrix protein collagen, is synthesised within the ER and inserted into the secretory pathway. Misfolded procollagen is directly trafficked via ERES micro-autophagy to degradative compartments. If this mechanism is impaired by the absence of ARL6IP1, procollagen will accumulate and detected by immunofluorescence or Western blotting. A crucial precondition for this experiment is the expression of procollagen within the studied cells — either endogenously or upon transfection.

6.2.7 Effects of ARL6IP1 mutation on ER shaping and ER morphology

ARL6IP1 is known to shape membranes (unpublished work of Nicole Koch and Yamamoto *et al.* (2014)). These experiments were conducted in rat brain-derived or artificial liposomes, respectively, by co-incubation with controls or ARL6IP1 and subsequent electron microscopic imaging. To elucidate the role of ARL6IP1 and its point mutation variants on ER morphology on a more macroscopic level, an assay with *Xenopus laevis* egg extract could be conducted (Wang *et al.* 2013). This would give insights on ARL6IP1-dependent network and tubule organisation. For this, the purified frog egg extracts containing ER membranes can be supplied with recombinantly expressed and purified proteins and imaged for its resulting ER morphology. This assay allows simple administration of multiple proteins (e.g., FAM134B) and variation of protein concentration with a readout in real-time.

The frame-shift mutation of ARL6IP1 (K193F*fs) very likely results in a fifth transmembrane domain. This appears to result in increased membrane shaping (as shown by Nicole Koch, unpublished work) of the ER. As the clinical phenotype proves, the ARL6IP1 function is impaired – either due to the enhanced shaping or the absence of functional groups at the C-terminus due to the changed amino acid sequence. This possibly could lead to a halted autophagosome generation as too little ER membrane is available for the growing autophagosome because of an impaired sprouting of ER membrane. Very recent ultrastructural studies of our lab on human skin fibroblasts of a patient carrying the homozygous K193F*fs mutation in ARL6IP1 revealed a massively changed ultrastructure of the rough ER with plenty whirls and invaginations (data not shown, manuscript in preparation). These structures could represent accumulated autophagosome precursors, halted during their maturation. In murine fibroblasts and DRG neurons deficient for *Arl6ip1,* no similar structures were observed indicating a potential unique pathomechanism in K193F*fs patients.

Although only few case studies with patients carrying mutations in ARL6IP1 or deficiency of the protein have been published, the described phenotypes differ depending on the mutation or protein deficiency. To further understand the different modes of action, neuron progenitor cells with mutated *ARL6IP1* additional to a short endogenous tag by CRISPR/Cas9 might be a helpful tool. This would allow interaction studies, for example by co-immunoprecipitation with subsequent mass spectrometry in differentiated neurons. Further, ultrastructural analyses of skin fibroblasts derived from patients carrying the L31P mutation would be desirable.

Membrane shaping proteins play a crucial role in remodelling of membranes (Prinz and Hinshaw 2009). Passive shaping proteins are able to curve membranes whereas energy-dependent motor proteins enhance and complete membrane fission. This is a fundamental process required for ER-phagy and also critical for the supply of endosomal membranes. ARL6IP1 is described to reside at the distal tips of ER tubules (Dong *et al.* 2018) which, besides ER exit sites (ERES), can serve as donor sites for ER-phagy, especially during starvation (Ge *et al.* 2017). Whether ARL6IP1 physiologically leads to fine ER tips which are later on detach and feed the endosomal pathways with membranes could be addressed in an experimental setting with high resolution imaging of live cells with marked ER. Reduced availability of the crucial process of ER-phagy goes along with severe consequences (UPR activation, ER dilation, reduced protein synthesis, diminished resilience against stressors like starvation, autophagy).

The enrichment of ARL6IP1 on peripheral tubules as described by (Dong *et al.* 2018) underlines the importance of the protein in distal cell areas. This is in line with observations of (Fowler and O'Sullivan 2016) who reported a loss of complexity in distal areas of long projecting neurons in fruit flies. With the help of the now available reporter mouse line Arl6ip1-ER-Tomato-Emx1, a future experiment could be imaging of newly formed synapses in hippocampal or cortical neuron cultures to compare the presence of ER structures in Arl6ip1-KO and WT. Similarly, the presence of ER tubules can be assessed within neuromuscular junctions of muscles like the *M. gastrocnemius*. In the same way, cultured sensory neurons could be assessed by an analogous experiment: In DRGs a large share of neurons is Parvalbumin (PV)-positive. Thus, the breeding of an Arl6ip1-ER-Tomato mouse line with PV as promotor for expression of the reporter protein was already initiated.

The ER morphology with its sheets and tubules is highly diverse. To stay in shape, it is strongly regulated by membrane-integrating shaping proteins and connector proteins that bridge ER

membrane contacts or mediate interaction with the plasma membrane or other organelles (Zhang and Hu 2016). Absence of shaping proteins such as ARL6IP1 may alter the delicate tubular network in distal parts of the cell; e.g., in axons and synapses of neurons. ER protrusions are necessary for shaping presynaptic boutons due to the function of the ER as Ca^{2+} reservoir: Calcium channels release the second messenger at the protrusion and thereby stabilise polymerized microtubules (Karagas and Venkatachalam 2019).

The ER has contacts with several organelles. This includes mitochondria, Golgi, endosomes, lysosome, peroxisomes, lipid droplets and the plasma membrane (Jing *et al.* 2020, Schwarz and Blower 2016). These contacts are essential for different functions such as lipid transfer (plasma membrane, Golgi, peroxisome, late endosome), Ca^{2+} exchange in mitochondria, endosomes, lysosomes, plasma membrane (Burgoyne *et al.* 2015) or serve as scaffold for proteins required for mitochondrial fission (Friedman *et al.* 2011). If now the complexity of the ER is lowered due to a loss of a shaping proteins such as ARL6IP1 ER-organellar contacts and hence its functions are decreased. Reduced mitochondrial fission was observed in long-projecting neurons of Drosophila deficient of Arl6ip1. Similar effects could be analysed by evaluating existing Arl6ip1-deficient and WT cells or tissue for their mitochondrial characteristics like number, circularity and length.

6.2.8 Amphipathic helices in ARL6IP1

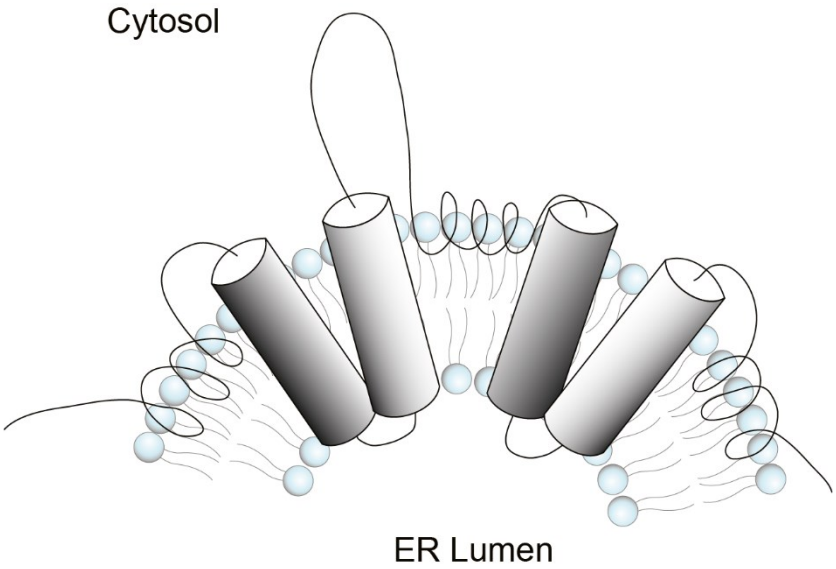

Figure 43: Suggested topology model of ARL6IP1 *with three functional amphipathic helices (APHs) resulting in a strongly bent protein.*

In this study, three putative amphipathic helices (APHs) were found to be predicted for ARL6IP1.

As the importance of these structures emerged in recent years, APHs on reticulon(-like) proteins became a focus of attention within this thesis. Recently, a middle and C-terminal APH of ARL6IP1 were reported, although only the middle APH was tested functionally (Brady *et al.* 2015, Dong *et al.* 2018). Destruction of the middle APH by mutation resulted in less enrichment of ARL6IP1 in ER tubule tips, probably due to less curvature. It has been reported that C-terminal KKXX is not functional as retention signal if too close to an APH (Vincent *et al.* 1998). This allows the speculation of an ER-retention mechanism depending on whether the C-terminal APH is incorrectly folded and hence not semi-integrated into the lipid bilayer which results in exposure of the KKXX motif.

If all three proposed APHs are functional, this would result in a highly bent ARL6IP1 protein explaining its localisation to ER tubule tips (Figure 43). Additionally, even if the middle APH is not functional (Supplement, (Dong *et al.* 2018)), the protein would be still curved and localised to ER tubules.

6.2.9 C-terminal topology of ARL6IP1

The location of the protein's C-terminus has been reported controversial (see 3.7.3). Thus, the need of new topology experiments was answered with a fluorescence protease protection (FPP) assay which suggested a cytosolic C-terminus (chapter 5.5.2). Briefly, the assay tests whether fluorescent proteins linked to the protein of interest are accessible to an added proteinase after plasma membrane permeabilisation by digitonin. If so, the measured fluorescence drops which can be analysed on a time axis. In detail, the background normalised signal intensity of CD3-RFP and FAM134B-GFP drops promptly upon trypsin administration. In contrast, the intraluminal RFP-KDEL signal is rather stable. ARL6IP1-GFP also shows a rapid but slower decline compared to CD3-RFP or FAM134B-GFP. The slower fluorescence diminishment of ARL6IP1-GFP can be explained by the accessibility of the C-terminal tag. While in ARL6IP1-GFP it is rather close to the ER membrane and the hence GFP possibly partly inaccessible (35 amino acids (aa) between last hydrophobic domain and fluorescent tag), the distance and therefore the accessibility is much higher in FAM134B-GFP (265 aa). The CD3-RFP resides in the plasma membrane with an intracellular C-terminus (60 aa membrane distance) and hence, is easier accessible by trypsin than inner ER membrane resident proteins. Taken together, the FPP assay suggests a cytosolic C-terminal end of ARL6IP1 that might be rather close to the ER membrane.

When assessing the report of Kuroda *et al.* (2013), which concluded a luminal C-terminus, limitations of the *Gaussia* luciferase (Gluc) assay become evident. For the fusion protein generation, the group inserted the reporter enzyme right within the ARL6IP1 sequence at the respective position without any flexible linker. This gives the opportunity of steric hindrance during protein folding, due to the 19-kDa Gluc enzyme. Additionally, it appears that C-terminal of the point of insertion, the residual ARL6IP1 protein sequence is still present and thereby frames the Gluc, further increasing the potential of misfolding due to steric hindrance. Kuroda *et al*. seem to have recognised this during their studies of the P64 position, which by their assay seems to be cytosolic, and hence also established a truncated P64* variant, where only the first 64 amino acids of ARL6IP1 are fused to C-terminal Gluc. In the same assay, truncated P64* variant resulted in a luminal localisation of Gluc underlining the importance of using truncation variants. Unfortunately, only this amino acid position was truncated, not the other 7 previously investigated sites, which limits the study's validity. Furthermore, reliable positive and negative controls are missing.

Hence, the FPP assay performed in this thesis appears to be a better suited method suggesting a cytosolic C-terminus in line with all other online resources (Pfam database) and recently published studies (Dong *et al.* 2018, Wakil *et al.* 2019) except of Kuroda *et al.* (2013).

6.2.10 ER abnormalities of ex vivo cultured cells

Besides the already described motor phenotype, it was reported that *ARL6IP1*-deficient patients additionally suffer from a sensory neuropathy (Nizon *et al.* 2018, Novarino *et al.* 2014). This means that not only motor neurons degenerate, but also the sensory neurons (chapter 3.1.2). These pseudounipolar neurons are named by their soma location within the dorsal root ganglia (DRG, Figure 1). ARL6IP1 is an ER-resident protein which is also thought to have an impact on the organelle morphology (Dong *et al.* 2018, Fowler and O'Sullivan 2016). Hence, DRG neurons were analysed for an altered ER morphology.

The ultrastructure of cultured DRG neurons reveals a reduced ER area proportion in perinuclear sections (chapter 5.10.2). This goes along with a changed morphology to a narrower ER constitution. At first view, this contradicts findings of Dong *et al.* (2018) who observed a shift to predominantly ER sheets upon knock-down of *Arl6ip1* by siRNA. However, the experimental settings strongly differ. This includes comparison of cultured *ex vivo* DRG neurons of mice deficient

for *Arl6ip1 versus* HeLa cells transfected with siRNA against *Arl6ip1* mRNA, morphologic analysis of perinuclear areas and quantitative assessment by electron microscopy of untransfected cells *versus* qualitative assessment of peripheral ER of cells overexpressing the ER marker GFP-Sec61β by confocal fluorescence microscopy. Hence, the results of such different study conditions cannot be directly compared. As an additional aspect, in ultra-thin sections of DRG neurons, the number of mitochondria appeared to be increased, the mitochondria itself enlarged and more interconnected. Remarkably, these findings are in agreement with previous reports, linking the loss of *Arl6ip1* to less mitochondrial fission (Fowler and O'Sullivan 2016). Further, degradative compartments seem to be more prominent in *Arl6ip1*-KO cells suggesting an impaired intracellular degradative machinery.

6.3 Conclusion

Disruption of *Arl6ip1* in mice mimicked key characteristics of the neurological disease phenotype in human. *Arl6ip1*-KO exhibited spasticity and hind-limb clasping upon lifting as well as reduced body weight upon muscular atrophy. These features clearly mimic the observed symptoms of patients with hereditary spastic paraplegia (HSP). Assessing the basic motor functions with the grip strength assay and foot-base angle (FBA), resulted in a distinct phenotype between genotypes with significant reduction in *Arl6ip1*-KO animals. The progressive manner of HSP was further underlined with even lower FBA of older KO animals which is in accordance with patients. To investigate a neurogenic cause, nerve conduction studies on caudal nerves were performed. These suggested a neuron loss due to reduced amplitude in both afferent and efferent fibres, highlighting the neuronal impairment and also an additional sensory phenotype. Further, assessment of the signal transduction velocity revealed a drop in KO animals for both afferent and efferent fibres suggesting a demyelination of the according neurons. Histological alterations were found in sensory fibres of the dorsal column, hippocampus and both somatosensory and somatomotor cortex of *Arl6ip1*-deficient *ER-Tomato* reporter mice. This study brought insights into the severity of *Arl6ip1*-loss *in vivo*, the predominantly affected tissue and could rule out some molecular mechanisms. However, further research is ongoing to pinpoint a more detailed mode of molecular action.

ARL6IP1 is an ER-resident membrane protein carrying a functional C-terminal ER-retention signal (KKXX), which is conserved in the most common model organisms. This protein is able to

shape membranes by means of reticulon-homology domains and amphipathic helices. Predicted LC3-interacting regions do not appear to be functional as revealed by co-immunoprecipitation (CoIP) analyses. The N-terminal half of ARL6IP1 (amino acids, aa 1-109) is found to be crucial for self-oligomerisation. Furthermore, it was found in CoIP studies that ARL6IP1 interacts with all members of the FAM134 protein family. In particular, FAM134B binds ARL6IP1 via its N-terminus (aa 1-161) as revealed by CoIP. This interaction was further bolstered by cellular colocalisation of ARL6IP1 and FAM134B proteins. A previous study identified a role of FAM134B in regulating ER turnover and maintaining long-term homeostasis and survival of long-projecting sensory neurons. It remains open whether and how exactly ARL6IP1 is able to modulate FAM134B function. Potentially, ARL6IP1 is required as a positive regulator or enhancer for FAM134B mediated ER-phagy and apparently fulfils further physiological functions in motor neurons.

With the rise of high-throughput sequencing technologies for diagnostic use it is likely that further *ARL6IP1* variants are going to be found in symptomatic patients. A therapy of inherited diseases is highly complex, but further understanding of the pathomechanism of diseases associated with ARL6IP1 mutations helps to shape a therapeutic strategy.

7 References

Akiduki S, Ikemoto MJ. 2008. Modulation of the neural glutamate transporter EAAC1 by the addicsin-interacting protein ARL6IP1. J Biol Chem, 283 (46):31323-31332.

Al-Bari MAA. 2020. A current view of molecular dissection in autophagy machinery. J Physiol Biochem.

Batt JA, Bain JR. 2013. Tibial nerve transection - a standardized model for denervation-induced skeletal muscle atrophy in mice. J Vis Exp, (81):e50657.

Baumann O, Walz B. 2001. Endoplasmic reticulum of animal cells and its organization into structural and functional domains. Int Rev Cytol, 205:149-214.

Bear M, Connors B, Paradiso MA. 2020. Neuroscience: Exploring the brain. Jones & Bartlett Learning, LLC.

Beetz C, Koch N, Khundadze M, Zimmer G, Nietzsche S, Hertel N, Huebner AK, Mumtaz R, Schweizer M, Dirren E, Karle KN, Irintchev A, Alvarez V, Redies C, Westermann M, Kurth I, Deufel T, Kessels MM, Qualmann B, Hübner CA. 2013. A spastic paraplegia mouse model reveals REEP1-dependent ER shaping. J Clin Invest, 123 (10):4273-4282.

Bhaskara RM, Grumati P, Garcia-Pardo J, Kalayil S, Covarrubias-Pinto A, Chen W, Kudryashev M, Dikic I, Hummer G. 2019. Curvature induction and membrane remodeling by FAM134B reticulon homology domain assist selective ER-phagy. Nat Commun, 10 (1):2370.

Biga LM, Dawson S, Harwell A, Hopkins R, Kaufmann J, LeMaster M, Matern P, Morrison-Graham K, Quick D, Runyeon J. 2019. Anatomy & physiology. Corvallis, Oregon: Oregon State University.

Birgisdottir AB, Lamark T, Johansen T. 2013. The LIR motif - crucial for selective autophagy. J Cell Sci, 126 (Pt 15):3237-3247.

Blackshaw S, Harpavat S, Trimarchi J, Cai L, Huang H, Kuo WP, Weber G, Lee K, Fraioli RE, Cho SH, Yung R, Asch E, Ohno-Machado L, Wong WH, Cepko CL. 2004. Genomic analysis of mouse retinal development. PLoS Biol, 2 (9):E247.

Blackstone C. 2012. Cellular pathways of hereditary spastic paraplegia. Annu Rev Neurosci, 35:25-47.

Blackstone C. 2018. Hereditary spastic paraplegia. Handb Clin Neurol, 148:633-652.

Blackstone C, Prinz WA. 2016. Keeping in shape. Elife, 5.

Brady JP, Claridge JK, Smith PG, Schnell JR. 2015. A conserved amphipathic helix is required for membrane tubule formation by Yop1p. Proc Natl Acad Sci U S A, 112 (7):E639-648.

Breeze E, Dzimitrowicz N, Kriechbaumer V, Brooks R, Botchway SW, Brady JP, Hawes C, Dixon AM, Schnell JR, Fricker MD, Frigerio L. 2016. A C-terminal amphipathic helix is necessary for the in vivo tubule-shaping function of a plant reticulon. Proc Natl Acad Sci U S A, 113 (39):10902-10907.

Burgess RW, Crish SD. 2018. Editorial: Axonopathy in Neurodegenerative Disease. Front Neurosci, 12:769.

Burgoyne T, Patel S, Eden ER. 2015. Calcium signaling at ER membrane contact sites. Biochim Biophys Acta, 1853 (9):2012-2017.

Carlsson SR, Simonsen A. 2015. Membrane dynamics in autophagosome biogenesis. J Cell Sci, 128 (2):193-205.

Chen Y, Yu L. 2017. Recent progress in autophagic lysosome reformation. Traffic, 18 (6):358-361.

Chukhrova AL, Akimova IA, Shchagina OA, Kadnikova VA, Ryzhkova OP, Polyakov AV. 2019. A new case of infantile-onset hereditary spastic paraplegia with complicated phenotype (SPG61) in a consanguineous Russian family. Eur J Neurol, 26 (5):e61-e62.

Costantini LM, Fossati M, Francolini M, Snapp EL. 2012. Assessing the tendency of fluorescent proteins to oligomerize under physiologic conditions. Traffic, 13 (5):643-649.

De Leonibus C, Cinque L, Settembre C. 2019. Emerging lysosomal pathways for quality control at the endoplasmic reticulum. FEBS Lett, 593 (17):2319-2329.

Dong R, Zhu T, Benedetti L, Gowrishankar S, Deng H, Cai Y, Wang X, Shen K, De Camilli P. 2018. The inositol 5-phosphatase INPP5K participates in the fine control of ER organization. J Cell Biol, 217 (10):3577-3592.

Edgar JM, McLaughlin M, Yool D, Zhang SC, Fowler JH, Montague P, Barrie JA, McCulloch MC, Duncan ID, Garbern J, Nave KA, Griffiths IR. 2004. Oligodendroglial modulation of fast axonal transport in a mouse model of hereditary spastic paraplegia. J Cell Biol, 166 (1):121-131.

Fagone P, Jackowski S. 2009. Membrane phospholipid synthesis and endoplasmic reticulum function. J Lipid Res, 50 Suppl:S311-316.

Farley FW, Soriano P, Steffen LS, Dymecki SM. 2000. Widespread recombinase expression using FLPeR (flipper) mice. Genesis, 28 (3-4):106-110.

Fowler PC, O'Sullivan NC. 2016. ER-shaping proteins are required for ER and mitochondrial network organization in motor neurons. Hum Mol Genet, 25 (13):2827-2837.

Fregno I, Molinari M. 2019. Proteasomal and lysosomal clearance of faulty secretory proteins: ER-associated degradation (ERAD) and ER-to-lysosome-associated degradation (ERLAD) pathways. Crit Rev Biochem Mol Biol, 54 (2):153-163.

Fregno I, Fasana E, Bergmann TJ, Raimondi A, Loi M, Solda T, Galli C, D'Antuono R, Morone D, Danieli A, Paganetti P, van Anken E, Molinari M. 2018. ER-to-lysosome-associated degradation of proteasome-resistant ATZ polymers occurs via receptor-mediated vesicular transport. EMBO J, 37 (17).

Friedman JR, Lackner LL, West M, DiBenedetto JR, Nunnari J, Voeltz GK. 2011. ER tubules mark sites of mitochondrial division. Science, 334 (6054):358-362.

Gatica D, Lahiri V, Klionsky DJ. 2018. Cargo recognition and degradation by selective autophagy. Nat Cell Biol, 20 (3):233-242.

Ge L, Zhang M, Kenny SJ, Liu D, Maeda M, Saito K, Mathur A, Xu K, Schekman R. 2017. Remodeling of ER-exit sites initiates a membrane supply pathway for autophagosome biogenesis. EMBO Rep, 18 (9):1586-1603.

Gimenez-Andres M, Copic A, Antonny B. 2018. The Many Faces of Amphipathic Helices. Biomolecules, 8 (3).

Goyal U, Blackstone C. 2013. Untangling the web: mechanisms underlying ER network formation. Biochim Biophys Acta, 1833 (11):2492-2498.

Grumati P, Dikic I, Stolz A. 2018. ER-phagy at a glance. J Cell Sci, 131 (17).

Hansen M, Rubinsztein DC, Walker DW. 2018. Autophagy as a promoter of longevity: insights from model organisms. Nat Rev Mol Cell Biol, 19 (9):579-593.

Heinrich T, Hübner CA, Kurth I. 2016. Isolation and Primary Cell Culture of Mouse Dorsal Root Ganglion Neurons. Bio-protocol, 6 (7):e1785.

Hirano T. 2018. Regulation and Interaction of Multiple Types of Synaptic Plasticity in a Purkinje Neuron and Their Contribution to Motor Learning. Cerebellum, 17 (6):756-765.

Hirano T, Kawaguchi SY. 2012. Regulation of inhibitory synaptic plasticity in a Purkinje neuron. Cerebellum, 11 (2):453-454.

Hu J, Shibata Y, Zhu PP, Voss C, Rismanchi N, Prinz WA, Rapoport TA, Blackstone C. 2009. A class of dynamin-like GTPases involved in the generation of the tubular ER network. Cell, 138 (3):549-561.

Huang HY, Liu JT, Yan HY, Tsai HJ. 2012. Arl6ip1 plays a role in proliferation during zebrafish retinogenesis. Cells Tissues Organs, 196 (2):161-174.

Huang HY, Dai ES, Liu JT, Tu CT, Yang TC, Tsai HJ. 2009. The embryonic expression patterns and the knockdown phenotypes of zebrafish ADP-ribosylation factor-like 6 interacting protein gene. Dev Dyn, 238 (1):232-240.

Hübner CA, Kurth I. 2014. Membrane-shaping disorders: a common pathway in axon degeneration. Brain, 137 (Pt 12):3109-3121.

Hutchins JB, Barger SW. 1998. Why neurons die: cell death in the nervous system. Anat Rec, 253 (3):79-90.

Ikemoto MJ, Murasawa Y, Wang PC. 2017. Pentylenetetrazol modulates redox system by inducing addicsin translocation from endoplasmic reticulum to plasma membrane in NG108-15 cells. Biochem Biophys Rep, 11:72-78.

Irintchev A, Simova O, Eberhardt KA, Morellini F, Schachner M. 2005. Impacts of lesion severity and tyrosine kinase receptor B deficiency on functional outcome of femoral nerve injury assessed by a novel single-frame motion analysis in mice. Eur J Neurosci, 22 (4):802-808.

Jackson MR, Nilsson T, Peterson PA. 1993. Retrieval of transmembrane proteins to the endoplasmic reticulum. J Cell Biol, 121 (2):317-333.

Jacomin AC, Samavedam S, Promponas V, Nezis IP. 2016. iLIR database: A web resource for LIR motif-containing proteins in eukaryotes. Autophagy, 12 (10):1945-1953.

Jing J, Liu G, Huang Y, Zhou Y. 2020. A molecular toolbox for interrogation of membrane contact sites. J Physiol, 598 (9):1725-1739.

Kalvari I, Tsompanis S, Mulakkal NC, Osgood R, Johansen T, Nezis IP, Promponas VJ. 2014. iLIR: A web resource for prediction of Atg8-family interacting proteins. Autophagy, 10 (5):913-925.

Kandel ER, Schwartz JH, Jessell TM, Biochemistry Do, Jessell MBT, Siegelbaum S, Hudspeth A. 2000. Principles of neural science. McGraw-hill New York.

Karagas NE, Venkatachalam K. 2019. Roles for the Endoplasmic Reticulum in Regulation of Neuronal Calcium Homeostasis. Cells, 8 (10).

Karnovsky MJ. 1965. A Formaldehyde-Glutaraldehyde Fixative of High Osmolality for Use in Electron Microscopy. Journal of Cell Biology, 27 (2):A137-+.

Katona I, Weis J. 2017. Diseases of the peripheral nerves. Handb Clin Neurol, 145:453-474.

Khaminets A, Heinrich T, Mari M, Grumati P, Huebner AK, Akutsu M, Liebmann L, Stolz A, Nietzsche S, Koch N, Mauthe M, Katona I, Qualmann B, Weis J, Reggiori F, Kurth I, Hübner CA, Dikic I. 2015. Regulation of endoplasmic reticulum turnover by selective autophagy. Nature, 522 (7556):354-358.

Khundadze M, Kollmann K, Koch N, Biskup C, Nietzsche S, Zimmer G, Hennings JC, Huebner AK, Symmank J, Jahic A, Ilina EI, Karle K, Schols L, Kessels M, Braulke T, Qualmann B, Kurth I, Beetz C, Hübner CA. 2013. A hereditary spastic paraplegia mouse model supports a role of ZFYVE26/SPASTIZIN for the endolysosomal system. PLoS Genet, 9 (12):e1003988.

Khundadze M, Ribaudo F, Hussain A, Rosentreter J, Nietzsche S, Thelen M, Winter D, Hoffmann B, Afzal MA, Hermann T, de Heus C, Piskor EM, Kosan C, Franzka P, von Kleist L, Stauber T, Klumperman J, Damme M, Proikas-Cezanne T, Hübner CA. 2019. A mouse model for

SPG48 reveals a block of autophagic flux upon disruption of adaptor protein complex five. Neurobiol Dis, 127:419-431.

Kirkin V, Rogov VV. 2019. A Diversity of Selective Autophagy Receptors Determines the Specificity of the Autophagy Pathway. Mol Cell, 76 (2):268-285.

Klionsky DJ. 2012. Look people, "Atg" is an abbreviation for "autophagy-related." That's it. Autophagy, 8 (9):1281-1282.

Klionsky DJ, Cregg JM, Dunn WA, Jr., Emr SD, Sakai Y, Sandoval IV, Sibirny A, Subramani S, Thumm M, Veenhuis M, Ohsumi Y. 2003. A unified nomenclature for yeast autophagy-related genes. Dev Cell, 5 (4):539-545.

Kuroda M, Funasaki S, Saitoh T, Sasazawa Y, Nishiyama S, Umezawa K, Simizu S. 2013. Determination of topological structure of ARL6ip1 in cells: identification of the essential binding region of ARL6ip1 for conophylline. FEBS Lett, 587 (22):3656-3660.

Kurokawa K, Nakano A. 2019. The ER exit sites are specialized ER zones for the transport of cargo proteins from the ER to the Golgi apparatus. J Biochem, 165 (2):109-114.

Kurth I. 2010. Hereditary Sensory and Autonomic Neuropathy Type II. In: Adam MP, Ardinger HH, Pagon RA, Wallace SE, Bean LJH, Stephens K, Amemiya A, Hrsg. GeneReviews((R)). Seattle (WA).

Kurth I, Pamminger T, Hennings JC, Soehendra D, Huebner AK, Rotthier A, Baets J, Senderek J, Topaloglu H, Farrell SA, Nurnberg G, Nurnberg P, De Jonghe P, Gal A, Kaether C, Timmerman V, Hübner CA. 2009. Mutations in FAM134B, encoding a newly identified Golgi protein, cause severe sensory and autonomic neuropathy. Nat Genet, 41 (11):1179-1181.

Lauwers E, Goodchild R, Verstreken P. 2016. Membrane Lipids in Presynaptic Function and Disease. Neuron, 90 (1):11-25.

Lein ES, Hawrylycz MJ, Ao N, Ayres M, Bensinger A, Bernard A, Boe AF, Boguski MS, Brockway KS, Byrnes EJ, Chen L, Chen L, Chen TM, Chin MC, Chong J, Crook BE, Czaplinska A, Dang CN, Datta S, Dee NR, Desaki AL, Desta T, Diep E, Dolbeare TA, Donelan MJ, Dong HW, Dougherty JG, Duncan BJ, Ebbert AJ, Eichele G, Estin LK, Faber C, Facer BA, Fields R, Fischer SR, Fliss TP, Frensley C, Gates SN, Glattfelder KJ, Halverson KR, Hart MR, Hohmann JG, Howell MP, Jeung DP, Johnson RA, Karr PT, Kawal R, Kidney JM, Knapik RH, Kuan CL, Lake JH, Laramee AR, Larsen KD, Lau C, Lemon TA, Liang AJ, Liu Y, Luong LT, Michaels J, Morgan JJ, Morgan RJ, Mortrud MT, Mosqueda NF, Ng LL, Ng R, Orta GJ, Overly CC, Pak TH, Parry SE, Pathak SD, Pearson OC, Puchalski RB, Riley ZL, Rockett HR, Rowland SA, Royall JJ, Ruiz MJ, Sarno NR, Schaffnit K, Shapovalova NV, Sivisay T, Slaughterbeck CR, Smith SC, Smith KA, Smith BI, Sodt AJ, Stewart NN, Stumpf KR, Sunkin SM, Sutram M, Tam A, Teemer CD, Thaller C, Thompson CL, Varnam LR, Visel A, Whitlock RM, Wohnoutka PE, Wolkey CK, Wong VY, Wood M, Yaylaoglu MB, Young RC, Youngstrom BL, Yuan XF, Zhang B, Zwingman TA, Jones AR. 2007. Genome-wide atlas of gene expression in the adult mouse brain. Nature, 445 (7124):168-176.

Lek M, Karczewski KJ, Minikel EV, Samocha KE, Banks E, Fennell T, O'Donnell-Luria AH, Ware JS, Hill AJ, Cummings BB, Tukiainen T, Birnbaum DP, Kosmicki JA, Duncan LE, Estrada K, Zhao F, Zou J, Pierce-Hoffman E, Berghout J, Cooper DN, Deflaux N, DePristo M, Do R, Flannick J, Fromer M, Gauthier L, Goldstein J, Gupta N, Howrigan D, Kiezun A, Kurki MI, Moonshine AL, Natarajan P, Orozco L, Peloso GM, Poplin R, Rivas MA, Ruano-Rubio V, Rose SA, Ruderfer DM, Shakir K, Stenson PD, Stevens C, Thomas BP, Tiao G, Tusie-Luna MT, Weisburd B, Won HH, Yu D, Altshuler DM, Ardissino D, Boehnke M, Danesh J, Donnelly S, Elosua R, Florez JC, Gabriel SB, Getz G, Glatt SJ, Hultman CM, Kathiresan S, Laakso M, McCarroll S, McCarthy MI, McGovern D, McPherson R, Neale BM, Palotie A,

Purcell SM, Saleheen D, Scharf JM, Sklar P, Sullivan PF, Tuomilehto J, Tsuang MT, Watkins HC, Wilson JG, Daly MJ, MacArthur DG, Exome Aggregation C. 2016. Analysis of protein-coding genetic variation in 60,706 humans. Nature, 536 (7616):285-291.

Li HY, Zheng XM, Che MX, Hu HY. 2012. A redox-sensitive luciferase assay for determining the localization and topology of endoplasmic reticulum proteins. PLoS One, 7 (4):e35628.

Lippincott-Schwartz J, Roberts TH, Hirschberg K. 2000. Secretory protein trafficking and organelle dynamics in living cells. Annu Rev Cell Dev Biol, 16:557-589.

Lopez A, Fleming A, Rubinsztein DC. 2018. Seeing is believing: methods to monitor vertebrate autophagy in vivo. Open Biol, 8 (10).

Lorenz H, Hailey DW, Wunder C, Lippincott-Schwartz J. 2006. The fluorescence protease protection (FPP) assay to determine protein localization and membrane topology. Nat Protoc, 1 (1):276-279.

Lorrain M. 1898. Contribution à l'étude de la paraplégie spasmodique familiale: travail de la clinique des maladies du système nerveux à la Salpêtrière. G. Steinheil.

Lui HM, Chen J, Wang L, Naumovski L. 2003. ARMER, apoptotic regulator in the membrane of the endoplasmic reticulum, a novel inhibitor of apoptosis. Mol Cancer Res, 1 (7):508-518.

Maddirevula S, Alzahrani F, Al-Owain M, Al Muhaizea MA, Kayyali HR, AlHashem A, Rahbeeni Z, Al-Otaibi M, Alzaidan HI, Balobaid A, El Khashab HY, Bubshait DK, Faden M, Yamani SA, Dabbagh O, Al-Mureikhi M, Jasser AA, Alsaif HS, Alluhaydan I, Seidahmed MZ, Alabbasi BH, Almogarri I, Kurdi W, Akleh H, Qari A, Al Tala SM, Alhomaidi S, Kentab AY, Salih MA, Chedrawi A, Alameer S, Tabarki B, Shamseldin HE, Patel N, Ibrahim N, Abdulwahab F, Samira M, Goljan E, Abouelhoda M, Meyer BF, Hashem M, Shaheen R, AlShahwan S, Alfadhel M, Ben-Omran T, Al-Qattan MM, Monies D, Alkuraya FS. 2019. Autozygome and high throughput confirmation of disease genes candidacy. Genet Med, 21 (3):736-742.

Magdaleno S, Jensen P, Brumwell CL, Seal A, Lehman K, Asbury A, Cheung T, Cornelius T, Batten DM, Eden C, Norland SM, Rice DS, Dosooye N, Shakya S, Mehta P, Curran T. 2006. BGEM: an in situ hybridization database of gene expression in the embryonic and adult mouse nervous system. PLoS Biol, 4 (4):e86.

Marques F, Sousa JC, Coppola G, Gao F, Puga R, Brentani H, Geschwind DH, Sousa N, Correia-Neves M, Palha JA. 2011. Transcriptome signature of the adult mouse choroid plexus. Fluids Barriers CNS, 8 (1):10.

Mauthe M, Orhon I, Rocchi C, Zhou X, Luhr M, Hijlkema KJ, Coppes RP, Engedal N, Mari M, Reggiori F. 2018. Chloroquine inhibits autophagic flux by decreasing autophagosome-lysosome fusion. Autophagy, 14 (8):1435-1455.

Moltedo O, Remondelli P, Amodio G. 2019. The Mitochondria-Endoplasmic Reticulum Contacts and Their Critical Role in Aging and Age-Associated Diseases. Front Cell Dev Biol, 7:172.

Moore KL, Dalley AF. 2018. Clinically oriented anatomy. Wolters kluwer india Pvt Ltd.

Nizon M, Kury S, Pereon Y, Besnard T, Quinquis D, Boisseau P, Marsaud T, Magot A, Mussini JM, Mayrargue E, Barbarot S, Bezieau S, Isidor B. 2018. ARL6IP1 mutation causes congenital insensitivity to pain, acromutilation and spastic paraplegia. Clin Genet, 93 (1):169-172.

Novarino G, Fenstermaker AG, Zaki MS, Hofree M, Silhavy JL, Heiberg AD, Abdellateef M, Rosti B, Scott E, Mansour L, Masri A, Kayserili H, Al-Aama JY, Abdel-Salam GMH, Karminejad A, Kara M, Kara B, Bozorgmehri B, Ben-Omran T, Mojahedi F, El Din Mahmoud IG, Bouslam N, Bouhouche A, Benomar A, Hanein S, Raymond L, Forlani S, Mascaro M, Selim L, Shehata N, Al-Allawi N, Bindu PS, Azam M, Gunel M, Caglayan A, Bilguvar K, Tolun A, Issa MY, Schroth J, Spencer EG, Rosti RO, Akizu N, Vaux KK, Johansen A, Koh AA,

Megahed H, Durr A, Brice A, Stevanin G, Gabriel SB, Ideker T, Gleeson JG. 2014. Exome sequencing links corticospinal motor neuron disease to common neurodegenerative disorders. Science, 343 (6170):506-511.

Omari S, Makareeva E, Roberts-Pilgrim A, Mirigian L, Jarnik M, Ott C, Lippincott-Schwartz J, Leikin S. 2018. Noncanonical autophagy at ER exit sites regulates procollagen turnover. Proc Natl Acad Sci U S A, 115 (43):E10099-E10108.

Omasits U, Ahrens CH, Muller S, Wollscheid B. 2014. Protter: interactive protein feature visualization and integration with experimental proteomic data. Bioinformatics, 30 (6):884-886.

Parodi L, Fenu S, Stevanin G, Durr A. 2017. Hereditary spastic paraplegia: More than an upper motor neuron disease. Rev Neurol (Paris), 173 (5):352-360.

Parzych KR, Klionsky DJ. 2014. An overview of autophagy: morphology, mechanism, and regulation. Antioxid Redox Signal, 20 (3):460-473.

Pasquier B. 2016. Autophagy inhibitors. Cell Mol Life Sci, 73 (5):985-1001.

Petit B, Giraudet F, Bechon C, Bardin L, Avan P, Boespflug-Tanguy O, Begou M. 2014. Mice with a deletion of the major central myelin protein exhibit hypersensitivity to noxious thermal stimuli: involvement of central sensitization. Neurobiol Dis, 65:55-68.

Pettersson M, Bessonova M, Gu HF, Groop LC, Jonsson JI. 2000. Characterization, chromosomal localization, and expression during hematopoietic differentiation of the gene encoding Arl6ip, ADP-ribosylation-like factor-6 interacting protein (ARL6). Genomics, 68 (3):351-354.

Prinz WA, Hinshaw JE. 2009. Membrane-bending proteins. Crit Rev Biochem Mol Biol, 44 (5):278-291.

Rao Y, Perna MG, Hofmann B, Beier V, Wollert T. 2016. The Atg1-kinase complex tethers Atg9-vesicles to initiate autophagy. Nat Commun, 7:10338.

Reggiori F, Ungermann C. 2017. Autophagosome Maturation and Fusion. J Mol Biol, 429 (4):486-496.

Schaaf MB, Keulers TG, Vooijs MA, Rouschop KM. 2016. LC3/GABARAP family proteins: autophagy-(un)related functions. FASEB J, 30 (12):3961-3978.

Schuck S, Gallagher CM, Walter P. 2014. ER-phagy mediates selective degradation of endoplasmic reticulum independently of the core autophagy machinery. J Cell Sci, 127 (Pt 18):4078-4088.

Schwarz DS, Blower MD. 2016. The endoplasmic reticulum: structure, function and response to cellular signaling. Cell Mol Life Sci, 73 (1):79-94.

Schweingruber C, Rufener SC, Zund D, Yamashita A, Muhlemann O. 2013. Nonsense-mediated mRNA decay - mechanisms of substrate mRNA recognition and degradation in mammalian cells. Biochim Biophys Acta, 1829 (6-7):612-623.

Schwenk F, Baron U, Rajewsky K. 1995. A cre-transgenic mouse strain for the ubiquitous deletion of loxP-flanked gene segments including deletion in germ cells. Nucleic Acids Res, 23 (24):5080-5081.

Shibata Y, Hu J, Kozlov MM, Rapoport TA. 2009. Mechanisms shaping the membranes of cellular organelles. Annu Rev Cell Dev Biol, 25:329-354.

Shibata Y, Voss C, Rist JM, Hu J, Rapoport TA, Prinz WA, Voeltz GK. 2008. The reticulon and DP1/Yop1p proteins form immobile oligomers in the tubular endoplasmic reticulum. J Biol Chem, 283 (27):18892-18904.

Spoerri PE, Dresp W, Heyder E. 1980. A simple embedding technique for monolayer neuronal cultures grown in plastic flasks. Acta Anat (Basel), 107 (2):221-223.

Stolz A, Grumati P. 2019. The various shades of ER-phagy. FEBS J, 286 (23):4642-4649.

Stolz A, Ernst A, Dikic I. 2014. Cargo recognition and trafficking in selective autophagy. Nat Cell Biol, 16 (6):495-501.

Strümpell A. 1883. Zur Kenntniss der multiplen degenerativen Neuritis. Archiv für Psychiatrie und Nervenkrankheiten, 14 (2):339-358.

Strunnikova NV, Maminishkis A, Barb JJ, Wang F, Zhi C, Sergeev Y, Chen W, Edwards AO, Stambolian D, Abecasis G, Swaroop A, Munson PJ, Miller SS. 2010. Transcriptome analysis and molecular signature of human retinal pigment epithelium. Hum Mol Genet, 19 (12):2468-2486.

Truett GE, Heeger P, Mynatt RL, Truett AA, Walker JA, Warman ML. 2000. Preparation of PCR-quality mouse genomic DNA with hot sodium hydroxide and tris (HotSHOT). Biotechniques, 29 (1):52, 54.

Varga RE, Khundadze M, Damme M, Nietzsche S, Hoffmann B, Stauber T, Koch N, Hennings JC, Franzka P, Huebner AK, Kessels MM, Biskup C, Jentsch TJ, Qualmann B, Braulke T, Kurth I, Beetz C, Hübner CA. 2015. In Vivo Evidence for Lysosome Depletion and Impaired Autophagic Clearance in Hereditary Spastic Paraplegia Type SPG11. PLoS Genet, 11 (8):e1005454.

Vincent MJ, Martin AS, Compans RW. 1998. Function of the KKXX motif in endoplasmic reticulum retrieval of a transmembrane protein depends on the length and structure of the cytoplasmic domain. J Biol Chem, 273 (2):950-956.

Wakil SM, Alhissi S, Al Dossari H, Alqahtani A, Shibin S, Melaiki BT, Finsterer J, Al-Hashem A, Bohlega S, Alazami AM. 2019. Truncating ARL6IP1 variant as the genetic cause of fatal complicated hereditary spastic paraplegia. BMC Med Genet, 20 (1):119.

Wang M, Kaufman RJ. 2016. Protein misfolding in the endoplasmic reticulum as a conduit to human disease. Nature, 529 (7586):326-335.

Wang S, Romano FB, Field CM, Mitchison TJ, Rapoport TA. 2013. Multiple mechanisms determine ER network morphology during the cell cycle in Xenopus egg extracts. J Cell Biol, 203 (5):801-814.

Yamamoto Y, Yoshida A, Miyazaki N, Iwasaki K, Sakisaka T. 2014. Arl6IP1 has the ability to shape the mammalian ER membrane in a reticulon-like fashion. Biochem J, 458 (1):69-79.

Yu L, Chen Y, Tooze SA. 2018. Autophagy pathway: Cellular and molecular mechanisms. Autophagy, 14 (2):207-215.

Zaffagnini G, Martens S. 2016. Mechanisms of Selective Autophagy. J Mol Biol, 428 (9 Pt A):1714-1724.

Zhang H, Hu J. 2016. Shaping the Endoplasmic Reticulum into a Social Network. Trends Cell Biol, 26 (12):934-943.

Zimmerberg J, Kozlov MM. 2006. How proteins produce cellular membrane curvature. Nat Rev Mol Cell Biol, 7 (1):9-19.

Zurek N, Sparks L, Voeltz G. 2011. Reticulon short hairpin transmembrane domains are used to shape ER tubules. Traffic, 12 (1):28-41.

8 Appendix

8.1 Supplement

A $_{21}$**EQLQGWGEVMLMADKVLR**$_{38}$

Physico-chemical properties	Polar residues + GLY	Nonpolar residues
Hydrophobicity <H>	Polar residues + GLY (n / %)	Nonpolar residues (n / %)
0.448	9 / 50.00	9 / 50.00
Hydrophobic moment <μH>	Uncharged residues + GLY	Aromatic residues
0.408	GLN 2, GLY 2	TRP 1,
Net charge z	Charged residues	Special residues
-1	LYS 1, ARG 1, GLU 2, ASP 1,	CYS 0, PRO 0
	Hydrophobic face : A W L M L	

Click to enlarge

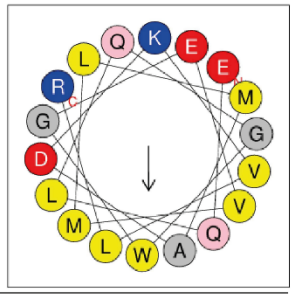

B $_{110}$**SNLVKTRRRAVGWWKRLF**$_{127}$

Physico-chemical properties	Polar residues + GLY	Nonpolar residues
Hydrophobicity <H>	Polar residues + GLY (n / %)	Nonpolar residues (n / %)
0.336	10 / 55.56	8 / 44.44
Hydrophobic moment <μH>	Uncharged residues + GLY	Aromatic residues
0.543	SER 1, THR 1, ASN 1, GLY 1	TRP 2, PHE 1,
Net charge z	Charged residues	Special residues
6	LYS 2, ARG 4,	CYS 0, PRO 0
	Hydrophobic face : none	

Click to enlarge

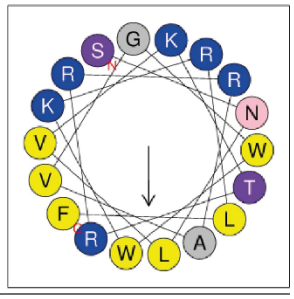

C $_{180}$**ILKYIGMAKREINKLLKQ**$_{197}$

Physico-chemical properties	Polar residues + GLY	Nonpolar residues
Hydrophobicity <H>	Polar residues + GLY (n / %)	Nonpolar residues (n / %)
0.365	9 / 50.00	9 / 50.00
Hydrophobic moment <μH>	Uncharged residues + GLY	Aromatic residues
0.596	GLN 1, ASN 1, GLY 1	TYR 1,
Net charge z	Charged residues	Special residues
4	LYS 4, ARG 1, GLU 1,	CYS 0, PRO 0
	Hydrophobic face : Y L A I I I L	

Click to enlarge

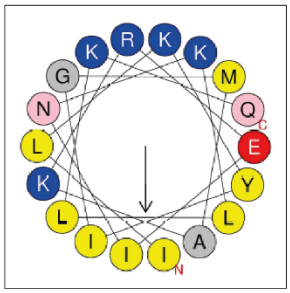

Figure S1: Calculations of features of the three identified amphipathic helices (APH) using the web-based tool HeliQuest. Stretches of 18 amino acids out of the recognised APH regions were analysed. Shown are the areas with maximal hydrophobic moment (μH) for each putative APH. (A) Frame 21-38 of the APH ranging from 16-41 aa. Note the strong hydrophobic moment (0.408) and evenly distributed polar (incl. Gly) and nonpolar residues of the investigated region. For comparison: the μH of APH Rtn1-4 range between 0.248 and 0.293. (B) Frame 110-127 of the APH ranging from 99-131 aa. μH = 0.543 with 55.6 % polar residues (incl. Gly). (C) Frame 180-197 of the APH ranging from 177-197 aa. μH = 0.596 with 50 % polar residues (incl. Gly). Amino acid colours: yellow = hydrophobic, blue = positively charged, red = negatively charged, antique pink = polar uncharged, grey = other.

Table S1: Mean compound muscle action potential amplitudes in mV. Significance was calculated with a two-way ANOVA followed by Bonferroni post-test.

Motor	1 month (N=6/7)			2 months (N=7/6)			6 months (N=6/6)		
Stimula-tion	WT	KO	p-Value	WT	KO	p-Value	WT	KO	p-Value
0 V	0.180	0.160	P > 0.05	0.166	0.108	P > 0.05	0.180	0.1600	P > 0.05
1 V	0.180	0.160	P > 0.05	0.163	0.106	P > 0.05	0.180	0.1600	P > 0.05
2 V	0.370	0.160	P > 0.05	0.193	0.122	P > 0.05	0.370	0.1600	P > 0.05
3 V	0.720	0.330	P > 0.05	0.213	0.120	P > 0.05	0.720	0.3300	P > 0.05
4 V	0.960	0.430	P > 0.05	0.788	0.146	P > 0.05	0.960	0.4300	P > 0.05
5 V	1.810	0.470	P > 0.05	1.050	0.288	P > 0.05	1.810	0.4700	P > 0.05
6 V	2.250	0.540	P > 0.05	1.638	0.428	P < 0.05	2.250	0.5400	P > 0.05
7 V	2.760	1.010	P < 0.05	2.067	0.756	P<0.01	2.760	1.010	P > 0.05
8 V	3.650	1.180	P<0.001	2.260	0.832	P<0.01	3.650	1.180	P<0.01
9 V	4.140	1.290	P<0.001	2.448	0.855	P<0.001	4.140	1.290	P<0.001
10 V	4.440	1.310	P<0.001	2.632	0.854	P<0.001	4.440	1.310	P<0.001
11 V	4.670	1.370	P<0.001	2.880	0.814	P<0.001	4.670	1.370	P<0.001
12 V	4.710	1.570	P<0.001	3.014	0.871	P<0.001	4.710	1.570	P<0.001
13 V	4.730	1.550	P<0.001	3.202	0.946	P<0.001	4.730	1.550	P<0.001
14 V	4.750	1.600	P<0.001	3.184	0.934	P<0.001	4.750	1.600	P<0.001
15 V	4.690	1.740	P<0.001	3.300	0.936	P<0.001	4.690	1.740	P<0.001

Table S2: Mean sensory amplitudes in mV. Significance was calculated with a two-way ANOVA followed by Bonferroni post-test.

Sensory	1 month (N=6/7)			2 months (N=7/6)			6 months (N=6/6)		
Stimula-tion	WT	KO	p-Value	WT	KO	p-Value	WT	KO	p-Value
0 V	0.180	0.160	P > 0.05	0.094	0.071	P > 0.05	0.120	0.100	P > 0.05
1 V	0.180	0.160	P > 0.05	0.103	0.064	P > 0.05	0.120	0.120	P > 0.05
2 V	0.370	0.160	P > 0.05	0.100	0.085	P > 0.05	0.140	0.110	P > 0.05
3 V	0.720	0.330	P > 0.05	0.106	0.075	P > 0.05	0.150	0.140	P > 0.05
4 V	0.960	0.430	P > 0.05	0.146	0.065	P > 0.05	0.150	0.130	P > 0.05
5 V	1.810	0.470	P > 0.05	0.153	0.079	P > 0.05	0.220	0.120	P > 0.05
6 V	2.250	0.540	P > 0.05	0.143	0.087	P > 0.05	0.280	0.120	P > 0.05
7 V	2.760	1.010	P < 0.05	0.163	0.074	P < 0.05	0.290	0.150	P > 0.05
8 V	3.650	1.180	P<0.001	0.183	0.082	P<0.01	0.300	0.140	P > 0.05
9 V	4.140	1.290	P<0.001	0.172	0.063	P<0.01	0.320	0.170	P > 0.05
10 V	4.440	1.310	P<0.001	0.202	0.082	P<0.001	0.380	0.140	P < 0.05
11 V	4.670	1.370	P<0.001	0.194	0.067	P<0.001	0.390	0.160	P < 0.05
12 V	4.710	1.570	P<0.001	0.223	0.079	P<0.001	0.430	0.150	P<0.01
13 V	4.730	1.550	P<0.001	0.203	0.071	P<0.001	0.410	0.150	P<0.01
14 V	4.750	1.600	P<0.001	0.210	0.094	P<0.001	0.420	0.140	P<0.01
15 V	4.690	1.740	P<0.001	0.198	0.077	P<0.001	0.410	0.140	P<0.01

8.2 List of Figures

8.3 List of Tables

8.4 Ehrenwörtliche Erklärung

Hiermit erkläre ich, dass mir die Promotionsordnung der Medizinischen Fakultät der Friedrich-Schiller-Universität bekannt ist,

ich die Dissertation selbst angefertigt habe und alle von mir benutzten Hilfsmittel, persönlichen Mitteilungen und Quellen in meiner Arbeit angegeben sind,

mich folgende Personen bei der Auswahl und Auswertung des Materials sowie bei der Herstellung des Manuskripts unterstützt haben:

Prof. C. A. Hübner, Dr. J. C. Hennings und Dr. L. Liebmann

die Hilfe eines Promotionsberaters nicht in Anspruch genommen wurde und dass Dritte weder unmittelbar noch mittelbar geldwerte Leistungen von mir für Arbeiten erhalten haben, die im Zusammenhang mit dem Inhalt der vorgelegten Dissertation stehen,

dass ich die Dissertation noch nicht als Prüfungsarbeit für eine staatliche oder andere wissenschaftliche Prüfung eingereicht habe und

dass ich die gleiche, eine in wesentlichen Teilen ähnliche oder eine andere Abhandlung nicht bei einer anderen Hochschule als Dissertation eingereicht habe.

Jena, 26.10.2020

_____

Hartmut Bocker

Hartmut Bocker

8.5 Danksagung

Hiermit möchte ich mich bei allen bedanken, die mich in verschiedenster Form bei meiner Promotion unterstützt und begleitet haben. Mein Dank gebührt an erster Stelle Prof. Christian Hübner für die Bereitstellung der interessanten Themen, die herausragenden Forschungsbedingungen, die Freiräume und die Betreuung.

Prof. Ingo Kurth danke ich für die angeregten Diskussionen und die praxisnahen Ratschläge. Vielen Dank für die konstruktiven Beiträge und Unterstützung, Prof. Helen Morrison.

Ebenso möchte ich der gesamten Arbeitsgruppe der *Funktionellen Genetik* für die angenehme Atmosphäre danken, speziell: Christopher für die akkuraten Einführungen in neue Methoden, allzeitige Bereitschaft zu helfen und *den* Humor, Tanja für ihre ausgestrahlte Ruhe, die omnipräsente Hilfsbereitschaft und die fließend sarkastischen Gespräche, Patricia für den Ansporn, Lutz für die Geduld beim Erklären und Diskutieren von Elektrophysiologie und Philosophie, Katrin für die Hilfe und Gespräche, Mukhran für die Unbekümmertheit und Johanna fürs gewissenhafte Zuarbeiten. Ich konnte bei weitem nicht nur Fachliches von euch lernen! Mein großer Dank geht ebenfalls an Antje, Milena und Adeela.

I thank Hector for his contributions and for taking over the Arl6ip1 project.

Des Weiteren bedanke ich mich bei allen Kooperationspartnern, Tierpflegern und allen nicht namentlich aufgeführten Mitarbeitern des Instituts für Humangenetik. Als Mitglied der DFG-Graduiertenschule *RTG 1715* möchte ich mich besonders bei Prof. Reinhard Wetzker und Dorith Schmidt bedanken.

Meinen Freunden Kai, Jan und Michel danke ich für die Reflektionen von außerhalb meines Forschungsfeldes und für ihr offenes Ohr, ganz gleich wie groß die räumliche Distanz war.

Melanie danke ich nicht nur für den Soundtrack meiner Dissertation, sondern auch für die Vielzahl an extracurricularen Aktivitäten und ihr Vermögen auch den Feiertagen noch etwas (Sub-)Kultur abzuringen.

Meiner Familie danke ich im besonderen Maße, da sie mich immer auf meinen Pfaden unterstütz und bestärkt hat. Ich kann mich glücklich schätzen euch zu haben.

Theresa, Danke für deine engelsgleiche Geduld, für die unverblümte, konstruktive Kritik aber auch für die fortwährende Motivation und omnipräsente Unterstützung. Ohne dich würde es diese Dissertation nicht geben.

Da steh' ich nun, ich armer Tor! Und bin so klug als wie zuvor.

Danke!

Hartmut